Institut für Meteorologie und Klimatologie
Gottfried Wilhelm Leibniz Universität Hannover

The Effect of Secondary Circulations on the Boundary Layer Turbulence during LITFASS-2003 - An LES Study

Björn Maronga

Diploma Thesis in Meteorology

May 26, 2010

"One never notices what has been done; one can only see what remains to be done."
(Marie Curie in a letter to her brother, 1894)

Abstract

The atmospheric boundary layer is characterized by turbulent transport of heat, moisture, momentum and other scalars. Numerical weather prediction models use grid resolutions in the order of kilometers, that cannot resolve microturbulent structures in the order of a few hundreds of meters or smaller. Hence, turbulence is parametrized using statistical approaches. Usually, these approaches are based on homogeneous turbulence, but former studies have shown that in the presence of thermal surface heterogeneities secondary circulations in the mesoscale appear that are superimposed on the turbulent flow field and modifying the turbulence characteristics to a significant amount. Therefore several studies investigated the effect of surface heterogeneities. However, in the majority of cases, idealized inhomogeneities were investigated (typically strip-like or checkerboard patterns).

The large-eddy simulation (LES) study of Uhlenbrock (2006) investigated the flow over realistic surface heterogeneities in the framework of the LITFASS-2003 experiment in an area of $400\ \mathrm{km}^2$. The LES model PALM was driven by measurements of the experiment and secondary circulations were observed and extracted from the simulation data by ensemble-averaging. Four different simulations were carried out with different synoptic conditions, particularly with varying background wind velocities and heterogeneous distributed surface heat fluxes owing to different land use. Depending on the wind speed and direction, the obtained circulations, oriented to the mean wind, appeared and local or roll-like structures developed. The latter could not be linked directly to the surface heterogeneity.

The present diploma thesis repeats some of the simulations of Uhlenbrock (2006) and takes a step forward in the study of the mesoscale circulations. The main hypothesis, that the flow is affected by a "smeared" surface heat flux and appropriate roll-like structures develop is confirmed by a correlation analysis, which forms an important part of the present study. Furthermore characteristic length scales of mesoscale scalar quantities are found to be significantly larger than those of velocity components. In addition to this, the contribution of the secondary circulation to vertical fluxes is quantified and it was possible to touch upon the effect on entrainment processes and the boundary layer growth due to surface heterogeneities. The simulations show ambiguous findings in the vertical contribution. While the sensible heat flux shows no enhancement and thus secondary circulations are most likely merely taking over a portion of the vertical transport of heat, the latent heat flux as well as the momentum fluxes suggest increased vertical fluxes under certain conditions in comparison with homogeneous cases. The entrainment is supposed to decrease in the presence of strong secondary circulations, which still is an open question in the scientific community.

Keywords: Surface heterogeneity, secondary circulation, large-eddy simulation

Zusammenfassung

Die atmosphärische Grenzschicht ist charakterisiert durch turbulenten Transport von Wärme, Feuchte, Impuls und anderen Skalaren. Numerische Wettervorhersagemodelle verwenden Gitterweiten in der Größenordnung von einigen Kilometern, die die Mikroturbulenz in der Größenordnung von ein paar Hundert Metern nicht auflösen können. Daher werden Turbulenzparametrisierungen verwendet, die auf statistischen Ansätzen beruhen. Diese Ansätze basieren im Allgemeinen auf der Annahme homogener Turbulenz. Bisherige Studien haben jedoch gezeigt, dass in der Gegenwart von thermischen Bodenheterogenitäten mesoskalige Sekundärzirkulationen auftreten, die der turbulenten Strömung überlagert sind und welche die Charakteristik der Strömung signifikant beeinflussen können. Aus diesem Grund beschäftigten sich viele Studien mit dem Effekt von Bodenheterogenitäten. In den meisten Studien wurden jedoch idealisierte Heterogenitäten (Streifen- oder Schachbrettmuster) untersucht.

Die numerische Untersuchung mit einem Grobstrukturmodell (engl.: *large-eddy simulation, LES*) von Uhlenbrock (2006) erforschte die Strömung über realistischen Bodenheterogenitäten im Rahmen des LITFASS-2003 Experimentes in einem 400 km^2 großen Gebiet. Der Antrieb des LES Modells PALM erfolgte mittels Messdaten aus dem LITFASS-Experiment. Sekundärzirkulationen konnten festgestellt und mit Hilfe des Ensemble-Mittels extrahiert werden. Vier verschiedene Simulationen wurden durchgeführt, die sich durch ihre synoptischen Vorgaben unterschieden, insbesondere durch unterschiedliche Hintergrundwindgeschwindigkeiten sowie durch die entsprechend der Landnutzung vorgegebenen heterogen verteilten bodennahen Flüsse von fühlbarer und latenter Wärme. In Abhängigkeit der Windgeschwindigkeit und -richtung entwickelten sich Zirkulationen, deren Strukturen sich in Richtung des mittleren Windes ausrichteten und bei höheren Windgeschwindigkeiten rollenartige Gestalt annahmen. Für diesen Fall war es bisher nicht möglich Abhängigkeiten von der darunterliegenden Heterogenität festzustellen.

Die vorliegende Diplomarbeit wiederholt Teile der Arbeit von Uhlenbrock (2006) und geht einen Schritt weiter um die Struktur von mesoskaligen Zirkulationen zu erforschen. Die Hypothese, dass die Strömung durch einen "verschmierten" bodennahen Wärmestrom beeinflusst wird und entsprechend diesem rollenartige Strukturen ausbildet, wird durch eine Korrelationsstudie bestätigt, die damit einen wichtigen Teil dieser Arbeit darstellt. Weiterhin werden charakteristische Längenskalen der mesoskaligen skalaren Größen berechnet, die aufzeigen, dass diese gegenüber den typischen Skalen der Geschwindigkeitskomponenten deutlich größer sind. Zudem wird der heterogenitätsinduzierte Beitrag der Sekundärzirkulationen zu Vertikalflüssen bestimmt und damit auch der Effekt auf das Grenzschichtwachstum und Entrainment-Prozesse angerissen. Die Simulationen zeigen uneinheitliche Ergebnisse. Während der gesamte fühlbare Wärmestrom sich unverändert zeigt und deshalb davon ausgegangen werden kann, dass die Sekundärzirkulation lediglich einen Teil des Vertikaltransportes übernimmt, deuten die Flüsse von latenter Wärme und Impuls im Vergleich mit homogenen Vergleichsläufen leicht erhöhte Gesamtflüsse bei bestimmten Bedingungen an. Das Entrainment scheint in der Gegenwart von starken Sekundärzirkulationen hingegen leicht reduziert zu sein, was jedoch noch eine offene Frage in der Wissenschaft darstellt.

Schlagwörter: Bodenheterogenität, Sekundärzirkulation, Grobstruktursimulation

Acknowledgements

First of all, I would like to thank the head of the PALM work group and my advisor, Prof. Dr. Siegfried Raasch, for his continuous guidance and supervising, particularly for the motivating, inspiring discussions and hints to solve technical problems. I also have to thank Prof. Raasch for his support during my semester abroad in Norway which was opening up new scientific perspectives. Furthermore, I would like to thank all members of the PALM group for the pleasant working atmosphere.

On the technical and bureaucratic side, special thanks go to Dr. Notker Fechner for the fast and capable IT support and Christiane Brünig for her help with any kind of form or application I had to fill in from time to time.

I am very grateful to my friend Annika Bleyer for correcting my English and to Dr. Gerald Steinfeld for his helpful comments on the manuscript from a scientific point of view.

Finally, I sincerely thank my family for the financial support during my studies.

Contents

List of Figures

List of Tables

List of Symbols and Abbreviations

Abbreviations

ABL	Atmospheric boundary layer
CBL	Convective boundary layer
CORINE	Coordinated Information on the European Environment, published by the European Environment Agency
DNS	Direct numerical simulation
FFT	Fast Fourier Transformation
HCR	Homogeneous control run
IMUK	Institute for Meteorology and Climatology at the Leibniz University of Hannover
LFA	LITFASS area
LES	Large-eddy simulation
LSM	Land Surface Model
MOL	Lindenberg Meteorological Observatory
MOST	Monin-Obhukov Similarity Theory
NWP	Numerical weather prediction
PALM	PArallelized Large-eddy simulation Model
RANS	Reynolds-averaged Navier-Stokes equation (Reynolds-averaged numerical simulation)
SC	Secondary circulation
SGS	Subgrid-scale model
SGS-TKE	Subgrid-scale turbulent kinetic energy, $\overline{e}$
SVAT	Soil-Vegetation-Atmosphere-Transfer Model
TKE	Turbulent kinetic energy

Greek letters

α_k	Kolmogorov constant
Δ;Δx, Δy, Δz	Grid length; grid lengths in x-, y-, z-direction
δ_{ij}	Kronecker delta
Δ_f	Fetch length
ε	Dissipation rate
ε_{ijk}	Levi-Civita symbol
η	Kolmogorov microscale
Λ	Dominant/Characteristic length scale
$\nu_m, \nu_h \nu_S$	Molecular viscosities for momentum, temperature and a scalar quantity
υ	Mean velocity in the boundary layer
Ω	Angular velocity of the Earth
Φ	Quantity
Ψ	Quantity
σ, σ^2	Standard deviation, variance
θ	Potential temperature
τ	Subgrid-scale stress tensor
Γ	Vertical gradient of potential temperature
φ	Geographical latitude
ρ	Correlation coefficient or air density

Operators

0	Basic state (Boussinesq approximation), surface value of a quantity (e.g. Φ_0) otherwise
$\lvert\Phi\rvert$	Absolute value of a quantity Φ
$\langle\Phi\rangle$	Time average of a quantity Φ
$\overline{\Phi}$	Temporal or spatial average of a quantity Φ
∂	Partial derivative symbol
$'$	Resolved-scale turbulent fluctuations, deviation from a mean value (section 2.1), subgrid-scale turbulent fluctuation (section 2.2)

$''$ ..... Subgrid-scale turbulent fluctuations or small-scale turbulent fluctuation (contains resolved and subgrid-scale fluctuations)

$*$ ..... Deviation from the basic state (Boussinesq approximation)

$\widetilde{\Phi}$ ..... Ensemble average of a quantity Φ

$\widetilde{\Phi'}$ ..... Heterogeneity induced (mesoscale) fluctuation of a quantity Φ

Roman letters

$\mathcal{A}_{[b(i+1),b(i)]}$ ..... Difference between two velocity fields with different border areas $b(i+1)$ and $b(i)$

$c_m = 0.1$ ..... Smagorinsky constant

dd ..... Wind direction

E ..... Spectral turbulent kinetic energy of a turbulent flow

e ..... Subgrid-scale turbulent kinetic energy

$\mathcal{F}$ ..... Height-integrated mesoscale vertical flux

ff ..... Wind speed

f_i ..... Coriolis parameter in tensor notation

$\mathcal{G}$ ..... Percental contribution of a height-integrated mesoscale flux to the total flux

g ..... Gravitational constant

u_g, v_g ..... Geostrophic wind velocity components. v_g is also referred to as the absolute value of the vector (u_g, v_g)

i, j, k ..... Integer indices $\in [1,2,3]$

k ..... Wave number

K_m, K_h, K_s ..... Turbulent diffusion coefficients of momentum, heat and scalars

k_s ..... Vertical stretch level

L ..... Length scale of the boundary layer

N ..... Integer number (e.g. of grid points)

p ..... Air pressure

q ..... Specific humidity

q_* ..... Characteristic humidity deviation

R ..... Reynolds stress

Re	Reynolds number
Ri	Richardson number, defined after Sullivan et al. (1998)
S	Scalar quantity
S_Φ	Discrete spectral energy of the quantity Φ, calculated by FFT
t	Time
θ_*	Characteristic temperature deviation
t_*	Characteristic time scale
$u, v, w; u_i$	Velocity components in direction of $x, y, z; x_i$
V	Volume of air
w_e	Entrainment rate, entrainment velocity
w_*	Vertical velocity scale
w_s	Subsidence velocity
$x, y, z; x_i$	Cartesian coordinates in space
z_0	Roughness length
z_i	Mean boundary layer height
$z_{i,loc}(x,y)$	Local boundary layer height, calculated by the modified gradient method
$\overline{z_{i,loc}}$	Mean local boundary layer height, calculated by the modified gradient method

1 Introduction

The present study investigates the effect of secondary circulations (SC), induced by realistic surface heterogeneities, on the boundary layer turbulence. With the aid of LES, the atmospheric boundary layer is simulated over heterogeneous surfaces to identify SCs and to obtain data for continuative analysis. This chapter gives an introduction into the atmospheric boundary layer over homogeneous and heterogeneous terrain, the derivation of the forcing dataset for the simulations and the current state of research. Furthermore, the main objectives of this study will be discussed.

1.1 The atmospheric boundary layer over heterogeneous terrain and heterogeneity induced secondary circulations

1.1.1 The atmospheric boundary layer over homogeneous terrain

The atmospheric boundary layer (ABL) is the lower part of the troposphere that is directly influenced by the Earth's surface and characterized by processes caused by surface forcings. The forcing processes, including frictional drag, heating, cooling, evaporation, transpiration and the absorbtion/disposal of more or less passive scalars (e.g. pollutants), are resulting in significant fluxes of sensible and latent heat as well as momentum and scalar quantities, which are usually of turbulent nature[1] (Stull, 1988; Garratt, 1992). Its height (or depth) varies typically between a few hundred meters and a few kilometers and is commonly referred to as z_i.

During daytime the ABL can be divided into three well-defined idealized layers that occur over land surfaces in high pressure regions. According to Stull (1988), the bottom 10 % of the boundary layer is called surface layer. It is the region, where turbulent fluxes and stress vary by less than 10 % of their magnitude. The lowest few centimeters of the surface layer are called microlayer, where turbulence is absent and molecular transport dominates. The mixed layer is located above the surface layer and is characterized by turbulence, which tends to mix heat, moisture and momentum vertically. Usually it is convectively driven, but there is also turbulence production by wind-shear. The source of convective turbulence production in the absence of clouds is the heat transfer from the surface layer into the mixed layer. In case of clouds atop the boundary layer, radiative cooling can also produce turbulence. In the diurnal cycle, the boundary layer is growing by entrainment at the interface between the mixed layer and the free atmosphere atop and is found to show its maximum depth in the late afternoon. The entrainment layer is the usually stably stratified capping zone and can be regarded as the transition zone to the free atmosphere, where hardly any turbulence is present. Rising thermals are able to penetrate into the entrainment zone/free atmosphere despite the stable conditions and corresponding downdrafts are leading to entrainment of warmer air into the boundary layer as well as momentum transport. The entrainment processes and the heating of the mixed layer lead to a continuous expansion of the convective boundary layer (CBL) during daytime.

There are three basic states of the boundary layer, the stable boundary layer (also called

[1] Turbulence can be regarded as irregular swirls of motions, so-called *eddies*.

nocturnal boundary layer), which is found to occur at night due to longwave outgoing radiation, the neutral boundary layer, which occurs for instance in overcast conditions and high background winds (Garratt, 1992) or above nocturnal stable boundary layers and the CBL (also called mixed layer), which is characterized by strong narrow updrafts of warm air due to surface forcings and cooler broader but weaker downdrafts (larger-scale). All these layers are displayed together with the near-neutral so-called residual layer in Fig. 1.1. The residual layer is the residuum of a mixed layer, which remains during nighttime, when the surface forcing and turbulent motions have vanished. It has immediate consequences for the boundary layer during daytime. It can rapidly merge into a CBL as soon as nocturnal inversions have vanished because it exhibits neutral stratification and well-mixed properties (Stull, 1988).

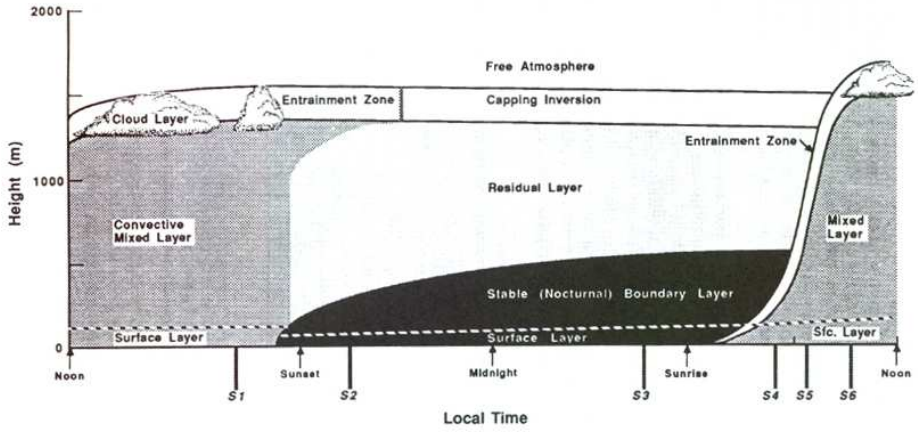

Figure 1.1: The boundary layer in high pressure over land in the diurnal cycle (after Stull, 1988).

1.1.2 The atmospheric boundary layer over heterogeneous terrain

Land surface heterogeneities can be divided into topographical and thermal heterogeneities. The former are composed by orography and vegetation/artificial elements and have been intensely investigated (e.g. local wind systems, forced up- und downward movements of air, orographic precipitation and kármán vortex streets). Heterogeneities are widely spread over the Earth's surface and a high spatial variability in vegetation, soil texture and wetness, land use and cloud cover (leading to local variability of incoming shortwave radiation at the surface) are rather the rule than homogeneous conditions (Letzel and Raasch, 2003). They are leading to horizontal differences in surface properties such as temperature, humidity, momentum and to differences of sensible and latent heat fluxes into the boundary layer. Their effect on the ABL, however, especially in case of realistic heterogeneities, still is an open question. In the majority of cases, idealized 1D oder 2D heterogeneities are studied. Several studies pointed out, that thermal heterogeneities lead to secondary circulations (e.g. Shen and Leclerc, 1995; Avissar and Schmidt, 1998; Raasch and Harbusch, 2001, see section 1.3). These thermal induced circulations can be considered as land and sea breeze systems (see Fig. 1.2), which are caused by large-scale pressure differences (Uhlenbrock, 2006).

Let the surface temperature of land and sea be equal in the morning hours. Due to incoming shortwave radiation in the course of the day, the land surface is heated up strongly, while the water temperature only rises slighty owing to the high heat capacity of water. The warm land surface yields also a heating of the near-surface air. The warm air is expanding and

lifting the isobars above the land surface, horizontal pressure gradients develop and horizontal compensational flows arise. Since the air mass above the land surface is reducing owing to the compensational flows, the surface pressure decreases next to the land surface (and increases next to the sea surface) and again horizontal compensational flows develop near the surface (sea breeze). Due to continuity reasons, the circulation is closed by strong updrafts (higher density of the warm air) over land and weak downdrafts of large-scale over the sea.

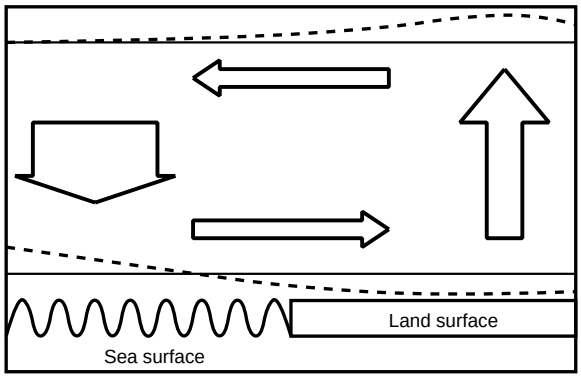

Figure 1.2: Schematic figure of a sea breeze system. Solid horizontal lines represent the isobar planes for homogeneous surface temperatures, the dashed lines show lifting or subsidence due to heterogeneous surface temperatures.

This scheme is also valid for thermal surface heterogeneities of different scales, but strongly dependent on the synoptic conditions, such as background wind, boundary layer height, incoming radiation and so forth and heterogeneity characteristics like size, or land use properties. Since heterogeneities are often found to be of smaller size than a classical land sea breeze system, the structure of SCs is more complex and superimposed on the randomly occuring eddies in homogeneous turbulence. The diurnal cycle of the boundary layer is of major importance for the development of SCs over realistic land surface heterogeneities, which consist typically of patches of water, forest and different agricultural fields. In the early morning hours, the land surface is relatively cold, due to nocturnal outgoing longwave radiation, while water patches show a higher temperature. In the course of the morning, solar radiation is able to heat up the land surface, so that the heterogeneity more or less vanishes. With further heating of the surface in the course of the day, characteristic heterogeneities develop according to the surface properties and circulations can occur. In the late afternoon, the forcing vanishes owing to the reduced incoming solar radiation and thus the heterogeneites and SCs vanish, too. Shen and Leclerc (1995) showed, that surface heterogeneities must be of the size of the boundary layer height (or larger) to be able to affect the boundary layer turbulence. The boundary layer is increasing permanently during daytime (see Fig. 1.1). From this follows, that the surface heterogeneity, which is affecting the flow in the boundary layer, is not only varying in time due to the diurnal cycle of incoming solar radiation, but also due to a change of the distribution of heterogeneous signals that are able to trigger SCs. Avissar and Schmidt (1998) investigated the influence of a mean background wind on the circulation by prescribing a one-dimensional heat flux wave and reported that a background wind (oriented along the waves) is decreasing the SC strength. A background wind of $5\ \mathrm{m/s}$ was found to eliminate all impacts of the surface heterogeneity. However, Raasch and Harbusch (2001) showed that a background wind is significantly modifying the structure of SCs, but not necessarily eliminiating it.

Mesoscale models and numerical weather prediction (NWP) models are using turbulence parametrizations (turbulence closure models), that are based on the classical analysis of

turbulence above homogeneous surface (Monin-Obkuhov Similarity Theory, MOST). These models cannot account for contributions by SCs of length and time scales caused by surface heterogeneities that are larger than turbulent eddies, typically found in a CBL, but smaller than the grid length (subgrid-scale turbulence) in mesoscale models. Thus, LES is commonly used to investigate the effect of surface heterogeneities in the CBL, also with the intention to improve turbulence parametrizations. In LES models the heterogeneities can be described by local surface temperature, humidity (or respective vertical fluxes) and roughness length to account for different vegetation height. Some studies used Land Surface Models (LSM) or Soil-Vegetation-Atmosphere-Transfer (SVAT) models, coupled to LES to prescribe the surface properties. Section 1.3 will outline past studies on the effect of surface heterogeneities and give an overview of the current state of research.

1.2 The LITFASS-2003 experiment

In 2002, the EVA-GRIPS[2] project was launched to investigate the influence of surface heterogeneities on the atmospheric boundary layer. Several research goups in the area of experimental and numerical meteorology participated to benefit from the synergy effect of this large-scale project. In 2003, the LITFASS-2003 experiment as main part of the EVA-GRIPS project was taking place in the surrounding area of Lindenberg in the southeast of Berlin, Germany.

At this point, a brief outline of the experiment shall be reported for a better understanding of the data set, which was used to drive the LES model PALM. For a complete and more detailed description, please refer to Beyrich et al. (2004), Beyrich and Mengelkamp (2006) and Beyrich et al. (2006a).

The experiment was taking place from 05/19/2003 to 06/17/2003 in a $20\ \mathrm{km} \times 20\ \mathrm{km}$ area in the southeast of Berlin, in the surroundings of the Lindenberg Meteorological Observatory (MOL). The area is defined by a rectangle with the geographical coordinates of the southwest corner ($52^\circ 5' 30'' N$) and the northeast corner ($52^\circ 16' 26'' E$). It is dominated by forest and water areas as well as several agricultural patches (43 % forest, 32 % agriculture, 13 % grass, 7 % water and 5 % settlements). The orography is weak-developed and varies between $\sim 40\ \mathrm{m}$ and $\sim 160\ \mathrm{m}$ AMSL, thus shadowing effects are only present in the early morning hours and resulting temperature differences can be rated as small in comparison to the temperature differences provoked by land use heterogeneities.

Energy balance stations

During the measurement period, energy balance stations and soil sensors were placed over each land use (except settlements, see section 3.1). For the forest and water areas, permanently installed systems of the DWD[3] were used. The following quantities were measured by the energy balance stations:

- Air: temperature (T), relative humidity (RH), wind speed (ff), wind direction (dd) and pressure (p)
- Radiation: $R_{sw}\uparrow$, $R_{sw}\downarrow$,$R_{lw}\uparrow$, $R_{lw}\downarrow$, surface temperature T_0

[2]Regional Evaporation at Grid/Pixel Scale over heterogeneous land surfaces
[3]German Weather Service

- Soil: temperature (T_b), humidity q and soil heat flux (B)
- Turbulence (eddy-covariance): sensible heat flux (H), latent heat flux (LE) and friction velocity (u_*)
- Precipitation.

$R_{sw}\uparrow$ is the shortwave outgoing portion of the radiation balance and $R_{sw}\downarrow$, $R_{lw}\uparrow$, $R_{lw}\downarrow$ the incoming shortwave, outgoing longwave and incoming longwave portions, respectively. The processing and quality control is discussed in Mauder et al. (2006).

Remote sensing

According to the operational procedure of the DWD, radiosondes were released daily in Lindenberg at 5 UTC, 11 UTC, 17 UTC and 23 UTC (see Neisser et al., 2002). For selected days, additional radiosondes at 8 UTC and 14 UTC provided profiles of temperature, relative humidity, pressure and wind for every 3 h during daytime. Furthermore, a Sodar/RASS ($z = 20 - 400$ m) as well as a lower atmosphere profiler (LAP, $z = 0.3 - 1.5$ km) and a tropospheric wind profiler (TWP, $z = 0.5 - 8.0$ km provided vertical profiles of temperature and wind. A microwave radiometer profiler (MWRP, $z = 0.1 - 10.0$ km) measured temperature and content of water vapor. Moreover, lidar systems were used.

Other measurements

Beside the measurements mentioned above, data from scintillometer (see Meijninger et al., 2006; Kohsiek et al., 2006) and the helicopter-borne turbulence probe Helipod (see Bange et al., 2006) was compared to the simulation results of Uhlenbrock (2006), but will not be used in the present study. The same holds for remote sensed data from NOAA[4] satellites. Hourly meteorological observations according to the WMO[5] guidelines (MOL, station code 10393) were available and the spatial distribution of precipitation was observed by radar systems at Berlin Tempelhof Airport.

1.3 Current state of research

The observation of SCs in experimental studies is difficult and underlies several restrictions since the location, complex structure, temporal evolution and strength of SCs are usually *a priori* unknown and their size can extent to hundreds of kilometers. The development of SCs is not only forced by surface characteristics and the background wind, but also by variability of the surface heating due to clouds and local differences in precipitation patterns. Ground-based area-wide measurements would be necessary to observe these circulations, which is hardly feasible. Furthermore the circulations are superimposed on small-scale turbulent motions and thus an averaging (ensemble-, phase- and/or time-averaging) is required to extract the SCs. Airborne measurements are also restricted owing to limitations in flight length and instantaneous linear measurement of atmospheric quantities. Moreover, all measurements contain errors. Despite the fact that measurement technology improved the imprecision of sensors, errors of $1 - 5$ % must be taken into account (Foken, 2003). Nevertheless, several large-scale

[4] National Oceanic and Atmospheric Administration, U.S.A.
[5] World Meteorological Organization

experimental studies investigated the boundary layer characteristics over heterogeneous land surfaces, for instance MONSOON'90 (Kustas and Goodrich, 1994), BOREAS (Sellers et al., 1995), LITFASS-98 (Beyrich et al., 2002a, 2002b), LITFASS-2003 (see section 1.2) and IHOP_2002 (Weckwerth et al., 2004). Uhlenbrock (2006) compared large-eddy simulation (LES) results to the measurements of the LITFASS-2003 experiment, but the present study investigates SCs against the background of numerical-theoretical simulations only. Therefore, this section will give a summary of the current state of research of numerical studies in the field of surface heterogeneities with emphasis on the development of SCs.

Contrary to experimental studies, numerical simulations are able to provide area-wide four-dimensional (time and space) fields of all atmospheric variables which allows the determination and separation of SCs. Numerous mesoscale modeling studies have pointed out that land surface heterogeneities have a significant effect on weather, such as the development of cumulus clouds and precipiation, and climate forecasting (e.g. Pielke, 2001; Weaver and Avissar, 2001; Ramos da Silva, 2006; Reen et al., 2006). Owing to the limitation of grid resolution in mesoscale models, some studies investigated surface heterogeneities (idealized or observation-based) in the scale of hundreds of kilometers. Chen and Avissar (1994a, 1994b) and Weaver (2004) suggested the heterogeneity induced vertical mesocale fluxes of heat and moisture to be comparable to or even larger than the turbulent fluxes. Other studies disagreed with this finding and stated that the effect on the mesoscale flux is not as significant as suggested (e.g. Zhong and Doran, 1997, 1998; Doran and Zhong, 2000).

Since the grid resolution of mesoscale models is relatively low, heterogeneities on the scale of tens of kilometers were investigated and turbulence was fully parametrized. LES models have been used increasingly over the past two decades to simulate the flow over idealized and realistic surface heterogeneities by resolving the bulk of the energy-containing eddies (see 2.1 for a descripton of the LES technique). The high grid resolutions in LES studies have allowed the investigation of smaller heterogeneities down to the size of a few meters.

Early studies investigated small-scale heterogeneities in the order of a few hundreds of kilometers with zero background wind (Hechtel et al., 1990; Hadfield et al., 1991) or with background wind (Hadfield et al., 1992), but found no significant effect on the boundary layer structure. The later studies of Shen and Leclerc (1995) and Raasch and Harbusch (2001) used checkerboard-like two-dimensional heterogeneities and reported that the surface heterogeneities in fact must be at least of the size of the boundary layer height to influence the boundary layer characteristics (e.g. vertical heat fluxes). The simulations of sinoidal stripe-like one-dimensional heterogeneity by Avissar and Schmidt (1998) showed that a background wind of $2.5\ \mathrm{m/s}$ reduced the effect and they suggested that a background wind of $5\ \mathrm{m/s}$ would eliminate the effect of the surface heterogeneity. Furthermore, they stated that the water-vapor variability does not significantly affect the CBL and that mesoscale roll-like structures (see Etling and Brown, 1993, for a review of roll vortices in the ABL) occur for larger wave lengths ($\geq 5\ \mathrm{km}$) and small surface heat flux amplitudes of the heterogeneity. These structures were found to considerably affect the mean profiles of temperature and sensible heat flux. Raasch and Harbusch (2001) disagreed with the former finding of Avissar and Schmidt (1998) and pointed out that the SCs do not necessarily vanish in the presence of a background wind up to $7.5\ \mathrm{m/s}$. They found a dependency of the circulation strength on the mean wind orientation in relation to their discontinuous checkerboard surface heat flux pattern, which explains the contradiction to the results of Shen and Leclerc (1995) and Avissar and Schmidt (1998). Letzel and Raasch (2003) found temporal oscillations in the turbulent kinetic energy (TKE), which were leading to a stabilizing / labilizing of the boundary layer and thus to an oscillation of the SC strength. This effect was ascribed to horizontal pressure gradients, caused by surface temperature differences, whose teardown is established by the SC before the pressure gradients reincrease owing to

the constant prescribed surface heating. Uhlenbrock (2006) found no respective oscillations in the LITFASS simulations, which can be linked to the background wind as well as the time-dependent and complex surface forcing. Kang (2009) also investigated temporal oscillations and suggested that the onset of the oscillations might be the start of a break-up process of fluctuations at the scale of the mesoscale heterogeneity to small-scale fluctuations and thus calls into question the applicability of mesoscale models for the investigation of the effect of mesoscale surface heterogeneities. This result also questions the proposed grid length for mesoscale models of $5-10$ km to investigate mesoscale circulations by Roy and Avissar (2000). Gopalakrishnan and Avissar (2000) investigated the dispersion of passive tracers over an one-dimensional heterogeneity in comparison with homogeneous simulations and found that surface heterogeneities with a characteristic length scale of 5 km decrease the vertical mixing of particles, but increase the horizontal mixing owing to horizontal pressure gradients and compensational flow near the surface.

The LES study of Patton et al. (2005) used one-dimensional heterogeneities. The boundary layer was forced by the feedback of a surface model to a constant incoming net radiation but without background wind. They studied organized motions as well as their quantitative influence on vertical fluxes and found that the structures of dynamical (velocities) and scalar fields differ significantly. They reported a dependency on the scale of the heterogeneity, the boundary layer height and the initial state of moisture. Particularly, they figured out that the strongest CBL response to soil-moisture heterogeneity occurs for ratios of the heterogeneity to boundary layer height between 4 and 9 and that the bulk TKE of the ABL is increased by about 20 %. Furthermore, Patton et al. (2005) found the contribution to vertical fluxes by SCs to be height-dependent up to 70 % of the total vertical fluxes. They also stated that heterogeneous surfaces can lead to tower measurement errors up to 60 %, if the background wind is negligible. Uhlenbrock (2006) studied the development of SCs over idealized and particularly real heterogeneities in a 400 km^2 area. For the latter simulations, measurement data from the LITFASS-2003 experiment was used as surface forcing. It was the first time that the boundary layer structure and occuring SCs could be simulated under more or less realistic conditions and surface heterogeneities in the diurnal cycle. The investigations of idealized one-dimensional heterogeneities did hardly show the former modifications of the boundary layer proposed by Avissar and Schmidt (1998) and Letzel and Raasch (2003). Uhlenbrock (2006) ascribed this to the complex and slower evolution of the SCs. Dependencies of the vertical transport of TKE on the ratios of scale of the heterogeneity to boundary layer height and surface heat flux amplitude to mean surface heat flux were found in agreement with the studies of Shen and Leclerc (1995) and Raasch and Harbusch (2001). The simulation of realistic surface heterogeneities showed the developement of SCs under realistic synoptic conditions and their evolution in the diurnal cycle. The results were validated by comparison of the simulation data with measurements (tower, aircraft, ground-based stations). Uhlenbrock (2006) investigated the contribution to total vertical fluxes in comparison to the study of Patton et al. (2005) and reported that the total flux is not modified in the presence of SCs, but that a portion is taken over by the circulations. However, he found typical contributions of $5-15$ % for the sensible and $10-20$ % for the latent heat flux, which are less than the proposed values by Patton et al. (2005). Uhlenbrock (2006) ascribed this to the influence of background winds. Furthermore, the study found dominant length scales of dynamic variables to be smaller than corresponding length scales of scalar quantities, which was in agreement with Patton et al. (2005) as well. Kang and Davis (2008) stated from their LES that the vertical transport of heat by mesoscale (secondary) circulations is negligible compared to the turbulent transport, which contradicts the results of Patton et al. (2005) and Uhlenbrock (2006). They used one-dimensional heterogeneities and found two different regimes in the fair-weather ABL about

noon in dependency of the heterogeneity intensity: temporal oscillations ($0.01-0.02$ Km/s) or quasi-steady ($0.02-0.04$ Km/s). Inagaki et al. (2006) studied the physical background of the imbalance of the energy balance, which is known to occur for eddy covariance measurements over heterogeneous regions, by using LES and a one-dimensional sinoidal surface heterogeneity. They found two mechanisms causing the imbalance: the modificated vertical heat flux due to SCs and the vertical heat transport by turbulent organized structures (cluster of thermals with larger time scales than that of the individual plumes).

Prabha et al. (2007) investigated the development of SCs over a realistic surface heterogeneity in a model domain of size $3.5\ \mathrm{km} \times 3.5\ \mathrm{km} \times 1.5\ \mathrm{km}$ ($x \times y \times z$) with emphasis on the identification of heterogeneity induced circulations and their influence on point measurements. They found area-averaged heat fluxes to be up to 20 % higher than over a homogeneous forest area and suggested that strong SC updrafts are able to enhance the entrainment at the top of the mixed layer. They found quasi-stationary SC structures in low wind speeds ($2\ \mathrm{m/s}$) and roll-like structure in higher winds ($5\ \mathrm{m/s}$). The latter result is in agreement with the simulation of Uhlenbrock (2006) over realistic heterogeneity. Moreover, Prabha et al. (2007) reported that the heterogeneity modified the bulk properties of the CBL, such as vertical velocity variances (associated with roll formation) and TKE.

The coupled LES-SVAT study of Courault et al. (2007) investigated the feedback of the surface heat fluxes to SCs. They suggested that small-scale heterogeneities (here $2.5\ \mathrm{km}$) are able to induce SCs which lead to horizontal transport of moisture from wet to dry areas. Courault et al. (2007) reported a decreased sensible surface heat flux over the dry patch and that these circulations affect the spatial-averaged turbulent surface fluxes in the model domain.

Some studies reported modifications of the boundary layer depth in that way that the mixing layer is thicker over warmer patches and thinner over colder surface patches (e.g. Uhlenbrock, 2006; van Heerwaarden and Vilà-Guerau de Arellano, 2008; Fesquet et al., 2009). The reason for the spatial variation of the boundary layer height was associated with rising SC updrafts that increase the entrainment above the warm patches. van Heerwaarden and Vilà-Guerau de Arellano (2008) concluded that the higher CBL leads to lower absolute temperatures over the center of the warm patch (here a one-dimensional heterogeneity was used) and that moisture is advected to the center of the warm patch by the SC. Therefore low absolute temperatures in combination with high specific humidity over the warm patch could indicate that cloud formation may be augmented over warm patches of surface heterogeneities. They furthermore reported that the entrainment in low-amplitude heterogeneity cases was less than in homogeneous cases, but higher in large-amplitude cases. However, van Heerwaarden and Vilà-Guerau de Arellano (2008) attributed this finding to differences in their model spin-up and not to existing SCs. Moreover, they found the specific humidity variance in the entrainment zone to be larger than under homogeneous conditions and thus suggested that cloud formation might be enhanced over heterogeneous surfaces.

Some studies (e.g. Bou-Zeid et al., 2004; Albertson and Parlange, 1999a, 1999b) supported the concept of a blending height, a height, where the signal of surface heterogeneity has vanished due to mixing in the boundary layer. These studies investigated small-scale heterogeneities of $\sim 1-3\ \mathrm{km}$. Albertson and Parlange (1999a) suggested the blending height of scalar quantities to be smaller than for fluxes. Uhlenbrock (2006) disagreed with the general concept and questions the existence of a blending height, since even upper height layers were found to be affected by the surface heterogeneities and SCs were spanning the entire boundary layer. This finding is also supported by the observational study of Kang and Davis (2007), who reported that the blending height exceeded the boundary layer depth in four of five fair-weather cases during IHOP_2002.

Stoll and Porté-Agel (2009) investigated the effect of discontinuous surface temperature distributions (differences of $3\ \mathrm{K}$ and $6\ \mathrm{K}$) on the stable boundary layer at length scales between $100\ \mathrm{m}$ and $400\ \mathrm{m}$. On the one hand, the results showed that an increasing temperature gradient between the surface patches leads to increased boundary layer heights, decreased average surface fluxes, larger gradients in potential temperature near the surface as well as elevated nocturnal jet formation. On the other hand, momentum fluxes and near-surface wind speed profiles were found to show a small sensitivity to the temperature distribution at the surface. These results might be relevant when simulating the ABL in the diurnal cycle, especially in the morning hours, when nocturnal inversions are present near the surface.

1.4 Scope and structure of the present study

As was discussed in the previous section, several studies investigated the boundary layer structure and SCs in the presence of surface heterogeneities. Uhlenbrock (2006) investigated the temporal and spatial structure of SCs over realistic surface heterogeneities as well as the contribution of SCs to total vertical heat fluxes during selected days of the LITFASS-2003 experiment. The simulation results were also compared to the measurement data of the experiment. The present study uses the same LES model in its latest revision to reproduce and question some of the results of Uhlenbrock (2006) and to take a step forward. So far it was not possible to predict the appearence of SC based on the surface properties in presence of a background wind higher than $\sim 2\ \mathrm{m/s}$. The present study will introduce a first concept that explains the location of roll-like structures, that developed under a background wind of $4-6\ \mathrm{m/s}$, based on a correlation analysis. Furthermore, the choice of a sufficient border area, which is necessary when using horizontal cyclic boundaries in the LES model, will be investigated and the heterogeneity induced scalar structures in the boundary layer is discussed using spectral analysis. A decomposition of vertical turbulent fluxes will attempt to give information about the question how vertical transport of heat, humidity and momentum is taken over or enhanced by SCs, including remarks on the consequences for the boundary layer growth and entrainment processes.

The achievements of the present study can be regarded as preliminary work for the two granted DFG[6] projects DFG RA $617/20-1$: "Turbulent Structure Parameters over Heterogeneous Terrain - Implications for the Interpretation of Scintillometer Data" and DFG RA $617/21-1$: "The Effect of Land Surface Heterogeneity on the Atmospheric Boundary-Layer Structure and Measurements".

According to these objectives, this thesis is going to pursue the following outline. In chapter 2 the LES model used in the present study will be introduced, including the governing equations and boundary conditions. Chapter 3 deals with the simulation setup and the forcing, that was derived from data obtained in the LITFASS-2003 experiment. It also contains a recapitulation of the definition and calculation method of heterogeneity induced quantities from Uhlenbrock (2006). Results of the simulations are presented in chapter 4. Section 4.1 determines the minimum size of additional border areas for realistic surface heterogeneities in LES models with cyclic boundary conditions in dependence on different background wind velocities, while section 4.2 investigates the boundary layer structure as well as spatial and temporal characteristics of SCs. Section 4.3 contains a study on the correlation between SCs and surface heterogeneity with emphasis on simulation cases where roll-like structures were observed. A summary is given and final conclusions are drawn in chapter 5.

[6] German Research Foundation

2 The Parallelized Large-Eddy Simulation Model PALM

In the present study, the parallelized LES model PALM was used for simulating the turbulent flow in the atmospheric boundary layer. PALM is the parallelized version of an LES model which has been used at the Institute for Meteorology and Climatology (IMUK) at the Leibniz University of Hannover and other institutes all around the world (e.g. Nansen Environmental and Remote Sensing Center, Bergen, Norway; Department of Atmospheric Sciences, Yonsei University, Seoul, Korea and ForWind - Center for Wind Energy Research, Oldenburg, Germany). It has been developed by Raasch and Etling (1991, 1998) and Raasch and Schröter (2001) since 1989.

PALM is based on the non-hydrostatic, filtered, incompressible Navier-Stokes equations in Boussinesq-approximated form (see section 2.2). Section 2.3 deals with the numerical implementation, namely discretization and numerical schemes such as time integration and advection schemes. Section 2.4 is concerned with the subgrid-scale modeling, that is to say the parametrization of the fraction of relevant processes on scales smaller than the grid resolution. The treatment of those processes is well-known in turbulence theory as the *closure problem* (see e.g. Stull, 1988, Chapter 6). In section 2.5, initial and boundary conditions available in PALM and used for the present study are discussed. Section 2.6 gives an outline of the parallelization method for runs on parallel supercomputers.

This chapter will not be able to provide an extensive description of PALM, but should give a clipped and precise overview of the essential functionality and relevant model parts. Further details can be found in Raasch and Schröter (2001) and in the online documentation available from `http://www.muk.uni-hannover.de/~raasch/PALM_group` .

However, first of all, the fundamental principles of modeling turbulent flows shall be exposed with paying special attention to the advantages of LES.

2.1 Numerical modeling of turbulent flows

Flows in the ABL are usually turbulent flows, i.e. characterized by stochastic, three dimensional, non-periodic and non-linear motions of different scales. Superimposed on the mean wind, they can mathematically be seen as swirls of motion, so called *eddies*. In general, the turbulent flow consists of eddies of different scales regarding size, characteristic velocity and lifetime, superimposing each other and being responsible for mixing and transport of quantities, namely momentum, heat, humidity and other scalars, in the ABL. The spectrum of different scale eddies ranges in space and time from large-scale advection down to molecular diffusion.

The largest eddies in the ABL are on the scale of the boundary layer depth, that is about $100\ \mathrm{m}$ to $3000\ \mathrm{m}$ in diameter, limited by the ground at the bottom and the temperature inversion on top of the boundary layer (Stull, 1988, chapter 1). These eddies contain the bulk of TKE with a lifetime up to hours and are therefore responsible for most of the mixing processes. The production of TKE is caused by instabilities of the mean flow due to buoyancy force and wind shear. The benefit of TKE implies the withdrawal of the respective energy from the mean flow.

All eddies are in permanent interaction with the mean flow as well as with other eddies, which leads to further instabilities and hence to a decay of larger to smaller eddies. During this decay, energy is transfered from large-scale to small-scale. This process is called *energy cascade*.

The smallest eddies are on the scale of millimeters with a lifetime of a split second before they decay into even smaller whirls. Due to being in the range of molecular viscosity, their kinetic energy is directly converted into internal energy, resulting in a (though usually marginal) heating of the flow. Dissipation of TKE can also occur because of buoyancy force, e.g. in case of a strong stable stratification. Turbulent vertically moving air particles have to achieve work against the temperature gradient of the ambient air and thus dissipating TKE (Etling, 2002, chapter 20).

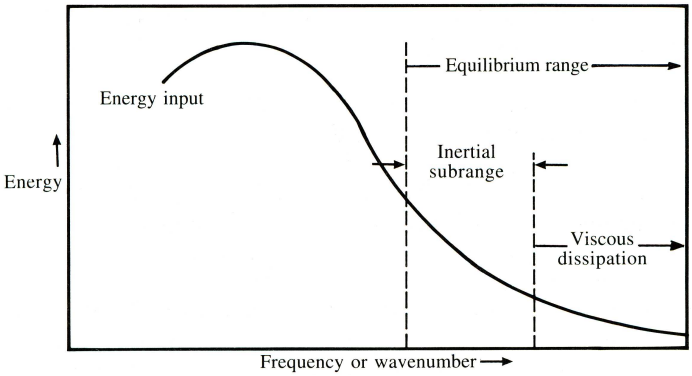

Figure 2.1: Schematic representation of the spectrum of TKE (after Garratt, 1992).

The TKE distribution in dependence on the eddy size is shown in Fig. 2.1. It clearly points out, that the larger eddies (smaller wave numbers) contain the bulk amount of TKE, while the smaller eddies (larger wave number) contain much less energy. Furthermore, a separation into three ranges of wave numbers, the large-scale spectrum, the inertial subrange and the dissipation range can be carried out related to the fact that production and dissipation are not taking place at same scales (Tennekes and Lumley, 1973). The former spectrum is characterized by the production of TKE and negligible molecular viscosity, while the latter is dominated by molecular viscosity. The smallest eddies are on the range of the Kolmogorov microscale η (this is the smallest scale of turbulence, see Stull, 1988, chapter 5). Because of their short lifetime, it can be assumed, that these eddies are statistically independent from larger eddies and the mean flow (Tennekes and Lumley, 1973) and should therefore be only dependent on the dissipation rate ε and the kinematic molecular viscosity ν_m. The Kolmogorov microscale is given by:

$$\eta = \left(\frac{\nu_m^3}{\varepsilon} \right)^{1/4} \quad . \tag{2.1}$$

Typical values for air are $\varepsilon \sim 10^{-3}$ m^{2}s^{-3} and $\nu_m \sim 10^{-3}$ m (e.g. Blackadar, 1997).

The range between the large-scale spectrum and dissipation range is neither affected by viscosity nor production of TKE. Eddies in the inertial subrange receive energy inertially from larger eddies and cede their energy to smaller eddies in a flow with constant energy flux across each wave number. Hence, the spectral energy E depends on ε and the wave number k. Following similarity theory with the aid of Buckingham Pi analysis (e.g. see Stull, 1988, chapter 9) this results in

$$E(k) = \alpha_k \, \varepsilon^{2/3} \, k^{-5/3} \quad , \tag{2.2}$$

where α_k is the Kolmogorov constant and k the wave number. In a spectrum log-log plot of E vs. k, the inertial subrange should appear as a straight line with a $-5/3$ slope (see Fig. 2.2) and is referred to as the *five-thirds power law*.

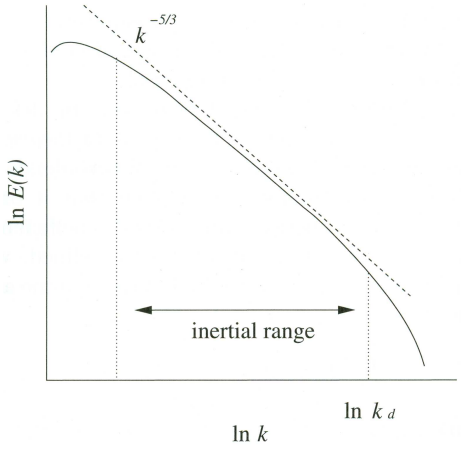

Figure 2.2: Schematic representation of the spectrum of TKE E against wave number (here k), logarithmically scaled (modified after Satoh, 2004). The inertial subrange follows five-thirds power law. $k_d = \dfrac{2\pi}{\eta}$ is the wave number at which dissipation works effectively and the power law is no longer valid.

There are three usual types of numerical models for simulating the ABL. The most precise one is called *Direct numerical simulation* (DNS). DNS models solve the Navier-Stokes equations numerically directly without the need of a turbulence model. Only numerical errors due to discretization in time and space occur and all scales of turbulence are directly resolved. This restricts the choice of the model resolution in time and space. On the one hand, the grid resolution has to be high enough to cover the Kolmogorov microscale η. On the other hand, the model domain has to be large enough to cover all the relevant TKE producing eddies (a length scale L follows). The ratio between the length scales L and η determines the necessary numbers of grid points N along one dimension:

$$N \sim \left(\frac{L}{\eta}\right) \sim Re^{3/4} \qquad , \tag{2.3}$$

where Re is the Reynolds number, defined as

$$Re = \frac{\text{inertial forcings}}{\text{viscous forcings}} = \frac{\upsilon\ L}{\nu_m} \qquad , \tag{2.4}$$

with the mean velocity υ in the boundary layer. In Eq. 2.3, the assumption

$$\varepsilon \sim \frac{\upsilon}{L} \tag{2.5}$$

was made according to measurements (e.g. Garratt, 1992). The Reynolds number is a common auxiliary number to determine similarity between different cases of flows in fluids regarding flow regimes, such as laminar and turbulent. Flows with Reynolds numbers $Re \gtrsim 10^3$ are assumed to be turbulent, while flows with Reynolds numbers $Re < 10^3$ are assumed to be laminar. A typical mean velocity for a CBL of $\upsilon \approx 1$ m/s and a characteristic length scale $L \approx 10^3$ m is leading to $Re \approx 10^8$ and thus is highly turbulent.

Assuming an equal number of grid points in each dimension and a Reynolds number for a CBL, one has to take into account a total amount of

$$N^3 \sim \left(Re^{3/4}\right)^3 \sim Re^{9/4} \sim 10^{18} \tag{2.6}$$

grid points. This extremely large number is barely applicable on today's supercomputers, despite the fact, that technical development is fast-paced in this area of research. Issues like computational power and data handling/storage will persist for the next couple of years and currently allow supercomputers the usage of up to 10^{11} grid points, an order of magnitude of seven below the suggested value, as stated by Steinfeld (2009) and Franke (2008). Moreover, paying attention to the cost-benefit-ratio is also compulsory for providing reasonable costs of computational time.

Another widely spread model type is based on the *Reynolds-averaged Navier-Stokes equations* (RANS). Here, the full spectrum of turbulence is parameterized. The main principle is the splitting of quantities Φ into a mean value $\overline{\Phi}$ and a statistical deviation Φ'

$$\Phi = \overline{\Phi} + \Phi' \qquad , \tag{2.7}$$

replacing the instantaneous quantities in the Navier-Stokes equations and time-averaging. In this way, only the temporal evolution of mean quantities is numerically simulated and all terms containing deviations are parameterized by a turbulence model. Hence, RANS models are computational cost-efficient, but the disadvantage is their strong dependence on the quality of the parametrization, which itself is not universal and depending on the purpose. Furthermore, the turbulent flow field is not simulated explicitly, thus inappropriate for a detailed study on boundary layer turbulence.

Large-eddy simulations

The popular LES technique tries to come to a compromise between DNS and RANS models by using advantages and reducing the disadvantages of both types. As already shown in Fig. 2.1, the large eddies contain most of the TKE, are more dependent on geometry and therefore much more important than small eddies, which are more universal (following from theory of self similiarity. See Kolmogorov, 1941, for a detailed explanation). The main concept behind LES is to explicitly solve the Navier-Stokes equations for the larger eddies and account for the smaller eddies by parameterization. The result is a separation of the flow into a resolved part, representing the large eddies, and a subgrid-scale part, representing the smaller eddies. Based on the theory by Kolmogorov (1941), the eddies in the inertial subrange lose their anisotropy while decaying into smaller eddies, which means, that they become less dependent on the flow regime and boundary conditions (unlike the large eddies). Due to this fact, the smaller eddies can be parameterized universally in a so-called subgrid-scale model (SGS). The separation of scales is realized by a filtering operation. Mathematically this can be seen as a phase space low-pass filtering which is explained in detail in section 2.2. Depending on the problem, the filtering lengths are in practice in a range from $0.01\ \mathrm{m}$ to $100\ \mathrm{m}$.

The advantages of LES are the possibility to simulate turbulent flows on high Reynolds numbers because the scale separation leads to a decreasing number of necessary grid points and the higher accuracy due to explicitly resolving the most relevant turbulent elements. Nevertheless, it should be mentioned, that LES does also imply some disadvantages. Especially in the vicinity of fixed borders and the entrainment zone as well as in generally stable boundary layers, the flow is dominated by small eddies and most of the TKE is parametrized. This is not following the principle of LES but cannot be avoided. However, due to the extensive computational needs, LES reaches the limits of today's supercomputers consistently.

2.2 Governing equations

All motions of atmospheric processes can be described with a system of equations, also called Navier-Stokes equations, for the conservation of momentum, mass, internal energy (potential temperature) and other scalars (active or passive). In tensor notation for a rotating Cartesian coordinate system, following Einstein summation convention, they can be written as

$$\frac{\partial u_i}{\partial t} + u_k \frac{\partial u_i}{\partial x_k} = \varepsilon_{ijk} f_j u_k - \frac{1}{\rho}\frac{\partial p}{\partial x_i} - g\delta_{i3} + \nu_m \left[\frac{\partial^2 u_i}{\partial x_j^2} + \frac{1}{3}\frac{\partial}{\partial x_i}\frac{\partial u_j}{\partial x_j}\right] \tag{2.8}$$

for the conservation of momentum, the continuity equation (conservation of mass)

$$\frac{\partial \rho}{\partial t} = -\frac{\partial(\rho u_i)}{\partial x_i}, \tag{2.9}$$

the first law of thermodynamics (internal energy)

$$\frac{\partial \theta}{\partial t} = -u_k \frac{\partial \theta}{\partial x_k} + \nu_h \frac{\partial^2 \theta}{\partial x_j^2} \tag{2.10}$$

and conservation of any given scalar S

$$\frac{\partial S}{\partial t} = -u_k \frac{\partial S}{\partial x_k} + \nu_S \frac{\partial^2 S}{\partial x_j^2} \ . \tag{2.11}$$

Here, ∂ is the partial derivative symbol. u_i, with the indices $i, j, k \in [1,2,3]$, are the velocities (also referred to as u, v, w) and x_i the space directions (x, y, z), respectively. $f_i = (0, 2\Omega\cos\varphi, 2\Omega\sin\varphi)$ is the Coriolis parameter, depending on the latitude φ and the angular velocity of the Earth Ω. The Levi-Civita symbol (also called permutation symbol) ε_{ijk} and the Kronecker delta δ_{ij} are used according to the Einstein notation. t is the time, ρ the air density, θ the potential temperature, g the gravitational constant and ν_m, ν_h, ν_S are the molecular viscosities belonging to momentum, temperature and the given scalar, respectively.

The given scalar S can be a passive scalar such as dust particle, but also a scalar quantity with an impact on the dynamics of the flow like humidity.

The Navier-Stokes equations 2.8 - 2.11 are partial differential equations with non-linear advection terms and therefore usually cannot be solved analytically and thus are solved numerically in PALM. Before being used in the model, the equations undergo the Boussinesq approximation and a filtering procedure. The former reduces the computational cost due to filtering sound waves, the latter is used to provide a separation between subgrid-scale and resolved-scale structures.

2.2.1 The Boussinesq approximation

The handling of atmospheric phenomena with vertical velocities of the same order of magnitude as the horizontal velocities like shallow convection, a Boussinesq approximation (named after the work of Boussinesq, 1903) leads to a significant simplification of the Navier-Stokes equations. A list of conditions for the CBL under which the approximation is valid can be found in Stull (1988). The air density is treated as incompressible and variations of density are neglected except for the buoyancy term. The approximation is based on splitting the variables $\Phi(x,y,z,t)$ into basic state $\Phi_0(z)$ and deviation field $\Phi^*(x,y,z,t)$ parts

$$\Phi(x,y,z,t) = \Phi_0(z) + \Phi^*(x,y,z,t) \ , \tag{2.12}$$

assuming that the basic state varies only with height and fulfills the equation of state for dry air

$$p_0 = \rho_0 R T_0 \ , \tag{2.13}$$

where p_0 is the pressure, R the gas constant and T_0 the temperature for dry air, as well as the hydrostatic equation

$$\frac{\partial p_0(z)}{\partial z} = -g\rho_0(z) \ . \tag{2.14}$$

Furthermore it is assumed, that the deviations of density, temperature and pressure are small compared to the basic states, i.e. $\rho^* << \rho_0$, $\rho^*/\rho_0 << 1$ and so forth. Due to this, most of the terms containing ρ^* disappear. The remaining deviations in the buoyancy term are replaced with deviations of potential temperature because of the convenience concerning measurements (Etling, 2002, Chapter 12):

$$\frac{\rho^*}{\rho_0} g\delta_{i3} = \frac{\theta^*}{\theta_0} g\delta_{i3} \ . \tag{2.15}$$

Applied to Eq. 2.9, the Boussinesq approximation leads to

$$\frac{\partial u_i}{\partial x_i} = 0 \ , \tag{2.16}$$

which is the continuity equation for an incompressible fluid. The resulting set of equations benefits from the incompressibility in this way, that the density is no longer time-dependent, thus sound waves cannot occur as a numerical solution and the timestep can be reduced by an order of magnitude. More detailed introductions to the Boussinesq approximation and its application can be found in Stull (1988, Chapter 3.3), Satoh (2004, Chapter 3.1) and Holton (2004, Chapter 5.1).

2.2.2 Filtering by Reynolds averaging

The separation of scales is realized by averaging over discrete grid volumes after Schumann (1975). The respective filter function reads as follows:

$$\overline{\Phi}(V,t) = \frac{1}{\Delta x \Delta y \Delta z} \int\int\int_V \Phi(V',t) \ dV' \tag{2.17}$$

for grid volumes

$$V = \left[x - \frac{\Delta x}{2}, x + \frac{\Delta x}{2}\right] \times \left[y - \frac{\Delta y}{2}, y + \frac{\Delta y}{2}\right] \times \left[z - \frac{\Delta z}{2}, z + \frac{\Delta z}{2}\right] \ . \tag{2.18}$$

The filtered quantity $\overline{\Phi}(V,t)$ is the spatial average of the size V at time t and available at the discrete grid points in the model domain. The subgrid-scale portion $\Phi(V',t)$, defined as

$$\Phi(V',t) = \Phi(V,t) - \overline{\Phi}(V,t) \tag{2.19}$$

represents the subgrid-scale local turbulent elements, which cannot be resolved by the model. It is similar to explicit filtering, using a top-hat filter with grid length as filter width (Letzel, 2007). This *volume-balance approach* is referred to as *implicit filtering* by Fröhlich (2006, chap. 5) and acts as a Reynolds operator (Schumann, 1973). Reynolds (1895) stated, that any atmospheric variable Φ can be decomposed into an average $\overline{\Phi}$ (slowly varying) and a turbulent fluctuation Φ'' (rapidly varying). Translated to Eq. 2.17, $\overline{\Phi}(V,t)$ is the spatial mean value and Φ'' represents

the subgrid-scale fluctuation. For any atmospheric variable, the Reynolds operator yields the following properties:

$$\overline{\Phi''} = 0 \quad \text{and} \quad \overline{\Phi\Psi} = \overline{\Phi}\,\overline{\Psi} + \overline{\Phi''\Psi''} \ . \tag{2.20}$$

Contrary to this chapter, where the overbar represents the resolved portion, the following chapters (Chapter 3 onwards) will use other notations, where the overbar is used for a spatial average and turbulent fluctuations are marked with prime or double prime.

2.2.3 Final set of governing equations in PALM

The application of the Boussinesq-approximation and the Reynolds averaging to the Navier-Stokes equations 2.8 - 2.11 and neglecting molecular diffusion, which is much smaller than turbulent diffusion, leads to the final set of equations used in PALM:

$$\frac{\partial \overline{u}_i}{\partial t} = -\frac{\partial(\overline{u}_i\overline{u}_k)}{\partial x_k} - \varepsilon_{ijk} f_j \overline{u}_k + \varepsilon_{i3k} f_3 \overline{u}_{g_k} - \frac{1}{\rho_0}\frac{\partial \overline{p}^*}{\partial x_i} + g\frac{\overline{\theta}^*}{\theta_0}\delta_{i3} - \frac{\partial \tau_{ki}}{\partial x_i}, \tag{2.21}$$

$$\frac{\partial \overline{u}_i}{\partial x_i} = 0 \ , \tag{2.22}$$

$$\frac{\partial \overline{\theta}}{\partial t} = -\frac{\partial(\overline{u}_k\overline{\theta})}{\partial x_k} - \frac{\partial(\overline{u_k''\theta''})}{\partial x_k} \ , \tag{2.23}$$

$$\frac{\partial \overline{S}}{\partial t} = -\frac{\partial(\overline{u}_k\overline{S})}{\partial x_k} - \frac{\partial(\overline{u_k''S''})}{\partial x_k} \ . \tag{2.24}$$

Here, u_{g_k} is the geostrophic wind and $\tau_{ki} = \overline{u_k''u_i''}$ is the subgrid-scale stress tensor. The geostrophic wind is defined by

$$\frac{1}{\rho_0}\frac{\partial p_0}{\partial x_i} = \varepsilon_{i3k} f_3 \overline{u}_{g_k} \ , \tag{2.25}$$

and takes into account pressure gradients on synoptic scales.

2.3 Discretization and numerical schemes

2.3.1 Discretization

In order to solve Eqs. 2.21 - 2.24 numerically, a discretization in time and space is necessary. PALM uses finite differences to achieve the discretization. Hence, differential operators are approximated by finite differences ($\partial \approx \Delta$). The variables are stored on a cartesian staggered grid (Arakawa-C grid, Arakawa and Lamb, 1977). Scalar quantities are defined at the center of each grid box, defined by the grid lengths Δx, Δy and Δz, while velocity components are defined at the grid box edges. The horizontal components are staggered by half a negative grid length, while the vertical velocity is staggered by half a positive grid length in their respective direction compared to scalar quantities. Owing to this, it is possible to calculate second-order approximations of spatial derivatives over only one grid length and the effective spatial model resolution can be increased by a factor of two in comparison with non-staggered grids (Letzel, 2007).

Contrary to the horizontal grid lengths Δx and Δy, which are equidistant, the vertical grid length Δz can be stretched above a user-defined height level k_s and the grid lengths are defined by

$$\Delta z(k+1) = \Delta z(k) \cdot a_s \ \forall \ k > k_s \ . \tag{2.26}$$

The stretch factor a_s is preset to 1.08. This method is used to save computational time in the upper model domain ($z > z_i$).

2.3.2 Numerical schemes

All terms, except the advection term are discretized by central differences. In this study, the second-order advection scheme (PALM default) of Piacsek and Williams (1970) is used. Alternatively, an *upstream-spline* scheme after Mahrer and Pielke (1978) is available in PALM. In addition, the monotone *Bott-Chlond* scheme (Chlond, 1994) is available for the advection of scalars. Ferziger and Perić (2002) and Letzel (2007) stated, that second-order schemes generate artifical $2 \cdot \Delta x_i$ oscillations upstream of solid walls owing to the poor handling of sharp gradients. It is worth mentioning, that the present study found this feature in flat terrain as well. In the early morning hours of the LITFASS simulations, these oscillations were observed and can be ascribed to the horizontal gradients (discontinuities) of the surface heterogeneity in the absence of a well-developed CBL.

PALM provides several time step schemes for the discretization in time. The present study uses the default *3rd-order Runge-Kutta* scheme (RK3, Durran, 1999). Furthermore, *Euler* and *leapfrog* schemes are also available, the latter with an *Asselin* time filter (Asselin, 1972).

The optional cloud physics mode (evaporation, condensation, precipitation) of PALM, described in Schröter (2003), is not used in this study. The density in PALM is set to a constant value of $\rho \equiv 1 \text{ kg/m}^3$.

The time integration of the Boussinesq equations is carried out for discrete points in time (time step Δt). Although a constant Δt can be prescribed, the time step is usually dynamically computed and varies according to the atmospheric properties and is restricted by two criteria. The CFL[1] criterion (Courant et al., 1928) reads as

$$\Delta t_{CFL} \leq \min \left(\frac{\Delta x_i}{\overline{u}_{i_{max}}} \right) , \tag{2.27}$$

but Δt is also restricted by the diffusion criterion (Roache, 1985):

$$\Delta t_{diff} \leq 0.125 \cdot \min \left(\frac{\Delta x_i^2}{\max(K_h, K_m)} \right) . \tag{2.28}$$

K_h and K_m are the turbulent diffusion coefficients of heat and momentum (see section 2.4), respectively. Both criteria secure the numerical stability by ensuring, that information is not transported farther than one grid length during one time step. Hence, PALM uses a time step of

$$\Delta t = 0.9 \cdot \min(\Delta t_{CFL}, \Delta t_{diff}) , \tag{2.29}$$

including a safety reduction by 10 %.

The continuity equation 2.22 requires incompressibility of the flow, but due to the fact that the time integration of Eq. 2.21 does not account for the continuity equation, it constantly generates divergences. For providing a divergence-free flow field, the *fractional step* method after Chorin (1968) and Chorin (1969) with the modifications of Patrinos and Kistler (1977) is applied after every step of the RK3 scheme. In a first step, a preliminary velocity field $\overline{u}_{i,pre}^{t+\Delta t}$ is calculated by time integration of Eq. 2.21 while excluding the pressure term $\frac{1}{\rho_0} \frac{\partial \overline{p}^*}{\partial x_i}$. The

[1] Courant-Friedrich-Lewy

occuring divergences can be ascribed to the pressure term and thus the prognostic velocity can be decomposed:

$$\overline{u}_i^{t+\Delta t} = \overline{u}_{i,pre}^{t+\Delta t} - \frac{r\Delta t}{\rho_0}\frac{\partial \overline{p^*}^t}{\partial x_i} \ . \tag{2.30}$$

Here, r is a constant, depending on the time integration scheme. The last step is the demand of incompressibility of $\overline{u}_i^{t+\Delta t}$. Eq. 2.30, inserted into Eq. 2.22 yields

$$\frac{\partial(\overline{u}_i^{t+\Delta t})}{\partial x_i} = \frac{\partial}{\partial x_i}\left(\overline{u}_{i,pre}^{t+\Delta t} - \frac{r\Delta t}{\rho_0}\frac{\partial \overline{p^*}^t}{\partial x_i}\right) \stackrel{!}{=} 0 \tag{2.31}$$

The result is a Poisson equation for the perturbation pressure $\overline{p^*}^t$:

$$\frac{\partial^2 \overline{p^*}^t}{\partial x_i^2} = \frac{\rho_0}{r\Delta t}\frac{\partial \overline{u}_{i,pre}^{t+\Delta t}}{\partial x_i} \ , \tag{2.32}$$

whose exact solution would make $\overline{u}_i^{t+\Delta t}$ free of divergence. However, practically the divergence can be reduced by several orders of magnitude which is found to be sufficient.

Besides iterative SOR[2] and multigrid, PALM provides a Fast Fourier Transformation (FFT) solver for the Poisson equation. The latter is used in case of cyclic boundary conditions like in the present study. A detailed description of the FFT can be found in Schröter (2003).

2.4 Subgrid-scale modeling

One of the main challenges in LES and RANS modelling is the turbulence closure. The filtering process yields to three covariance terms, which cannot be calculated explicitly: the second-order subgrid-scale stress tensor $\tau_{ki} = \overline{u_k'' u_i''}$ as well as the subgrid-scale fluxes of temperature and other scalars $\overline{u_k'' \theta''}$ and $\overline{u_k'' S''}$. The parametrization of these terms in the form of resolved-scale quantities is necessary to solve the prognostic equations and is called turbulence closure problem. PALM uses the turbulence closure proposed by Deardorff (1980). The scheme uses flux-gradient relationships in a $1\frac{1}{2}^{\text{th}}$ order closure, assuming that the energy transport by turbulent subgrid-scale eddies is proportional to the local gradients of the mean quantities:

$$\tau_{ki} = -K_m\left(\frac{\partial \overline{u}_i}{\partial x_k} + \frac{\partial \overline{u}_k}{\partial x_i}\right) \ , \tag{2.33}$$

$$\overline{u_k'' \theta''} = -K_h \frac{\partial \overline{\theta}_i}{\partial x_k} \ , \tag{2.34}$$

$$\overline{u_k'' S''} = -K_s \frac{\partial \overline{\theta}_i}{\partial x_k} \ . \tag{2.35}$$

The turbulent diffusion coefficients of momentum K_m and heat $K_h = K_s$ are expressed by the subgrid-scale turbulent kinetic energy (SGS-TKE) $\overline{e}$ and the mixing length l:

$$K_m = c_m l \sqrt{\overline{e}} \ , \tag{2.36}$$

$$K_h = K_m\left(1 + \frac{2l}{\Delta}\right) \ , \tag{2.37}$$

[2] Successive Over-Relaxation

where $c_m = 0.1$ is the Smagorinsky constant and $\Delta = \sqrt[3]{\Delta x \cdot \Delta y \cdot \Delta z}$. The mixing length can be regarded as measure for the size of the eddies. Physically it is the free path length of air molecules (Etling, 2002). It can be expressed in dependence of the stratification:

$$l = \begin{cases} \min\left(\Delta, 0.7z, 0.76\sqrt{\overline{e}}\left(\frac{g}{\theta_0}\frac{\partial\overline{\theta}}{\partial z}\right)^{-\frac{1}{2}}\right), & \frac{\partial\overline{\theta}}{\partial z} > 0\ , \\ \min\left(\Delta, 0.7z\right), & \frac{\partial\overline{\theta}}{\partial z} \leq 0\ . \end{cases} \tag{2.38}$$

Here, height z is the distance from the bottom surface and consequently, it is accounted for the requirement of l to be smaller than the grid length and not larger than the distance from the surface. The remaining unknown $\overline{e}$, which is defined as

$$\overline{e} = \frac{1}{2}\overline{u_i'' u_i''}\ , \tag{2.39}$$

requires an additional prognostic equation (see Stull, 1988, chap. 5)

$$\frac{\partial\overline{e}}{\partial t} = -\frac{\partial(\overline{u}_j\overline{e})}{\partial x_j} - \tau_{ij}\frac{\partial\overline{u}_i}{\partial x_j} + \frac{g}{\theta_0}\overline{u_3''\theta_j''} - \frac{\partial}{\partial x_j}\left[\overline{u_j''\left(e + \frac{p''}{\rho_0}\right)}\right] - \varepsilon\ . \tag{2.40}$$

Eq. 2.40 requires further parametrizations of the subgrid-scale terms that complete the closure in PALM:

$$\overline{u_3''\theta''} = -K_h\frac{\partial\overline{\theta}}{\partial x_3}\ , \tag{2.41}$$

$$\overline{u_j''\left(e + \frac{p''}{\rho_0}\right)} = -2K_m\frac{\partial\overline{e}}{\partial x_j} \tag{2.42}$$

and for the SGS-TKE dissipation rate ε:

$$\varepsilon = \left(0.19 + 0.74\frac{l}{\Delta}\right)\frac{\overline{e}^{\frac{3}{2}}}{l}\ . \tag{2.43}$$

2.5 Initial and boundary conditions

Initial and boundary conditions are necessary to solve Eqs. 2.21 - 2.24. Boundary conditions are required since, contrary to the Earth, the model domain is finite. In the majority of cases as well as in this study, cyclic lateral boundary conditions are chosen. In consideration of non-regular surface heterogeneities in the present study, the choice of cyclic boundaries implies some problems, which will be discussed in chapter 3. However, cyclic boundaries offer the advantage of an infinite, horizontal repeating model domain and outflowing eddies match inflowing eddies. Dirichlet boundary conditions were chosen at top of the model domain for the velocity components and perturbation pressure ($\overline{u}(x,y,z_{max}) = u_g$, $\overline{v}(x,y,z_{max}) = v_g$, $\overline{w}(x,y,z_{max}) = 0$, $\overline{p*}(x,y,z_{max}) = 0$) and Neumann conditions for the SGS-TKE ($\overline{e}(x,y,z_{max}) = \overline{e}(x,y,z_{max} - \Delta z)$). The top boundary condition for the scalar quantities is constant in time and calculated from the vertical gradient:

$$\left.\frac{\partial\overline{\theta}}{\partial z}\right|_{z_{max}} = \left.\frac{\partial\overline{\theta}}{\partial z}\right|_{z_{max}, t=0}\ . \tag{2.44}$$

The bottom boundary of the model corresponds to the Earth's surface. Therefore a Dirichlet boundary condition is used for the vertical velocity ($\overline{w}(x,y,z=0)=0$). Potential temperature, perturbation pressure and SGS-TKE hold Neumann conditions:

$$\overline{e}\left(-\frac{\Delta z}{2}\right)=\overline{e}\left(+\frac{\Delta z}{2}\right)\ ,\ \overline{\theta}\left(-\frac{\Delta z}{2}\right)=\overline{\theta}\left(+\frac{\Delta z}{2}\right)\ ,\ \overline{p*}\left(-\frac{\Delta z}{2}\right)=\overline{p*}\left(+\frac{\Delta z}{2}\right)\ . \tag{2.45}$$

No-slip boundary conditions for the horizontal velocity components requires $\overline{u}$ and $\overline{v}$ to equal 0 at the surface. Since they are defined on the staggered grid at height $z=\pm\frac{\Delta}{2}$, this is realized by mirror boundary conditions:

$$\overline{u}\left(-\frac{\Delta z}{2}\right)=\overline{u}\left(+\frac{\Delta z}{2}\right)\ ,\ \overline{v}\left(-\frac{\Delta z}{2}\right)=\overline{v}\left(+\frac{\Delta z}{2}\right)\ . \tag{2.46}$$

Between the bottom surface and the first vertical grid point, a Prandtl-layer is assumed. Heat and momentum fluxes are calculated in this layer with the aid of MOST. Since heat fluxes will be prescribed directly for the simulations in the present study, only momentum fluxes are calculated by MOST and by means of the friction velocity u_*. A more detailed description of the Prandtl-layer used in PALM can be found in Schröter (2003) and Steinfeld (2009).

Initial profiles of all scalar quantities can be prescribed explicitly by the user. Owing to the Coriolis force, prescribed profiles of the geostrophic velocity components would be unbalanced. To avoid this, one-dimensional precursor runs are integrated in PALM. With a given geostrophic wind and constant temperature profiles, precursor runs are carried out to obtain balanced wind profiles as initial conditions for the simulations. By default, the initial state of the three-dimensional quantities is horizontally homogeneous. Section 3.1 reveals how heterogeneous initial conditions are accomplished in the present study.

A system-specific random generator is used to impose random perturbations on the homogeneous velocity field during the first time steps to provoke turbulence until the resolved TKE reaches a threshold value. The random generator provides a series of uncorrelated numbers with Gaussian distribution in the range of $[0,1]$ which are multiplied by the velocity fields.

2.6 Parallelization

The programming language of PALM is FORTRAN 95. The model is parallelized and optimized for the usage on massively parallel and vector computers since 1998 (Raasch and Schröter, 2001). The parallelization uses the Message Passing Interface (MPI, Gropp et al., 1999) with one- or two-dimensional grid decomposition and optional OpenMP[3] parallelization for shared-memory machines. It allows the simulation of the ABL with a large number of grid points and high grid resolutions. The model domain is decomposed into several columns which are distributed to the given number of processors (processor element, PE). Each PE is solving the governing equations described in section 2.2. Thereby dependencies on data points of other PEs occur. To make this data accessible, ghost borders are defined at each of the column's edges that contain data from the surrounding PEs. The data exchange of the ghost points (communication) is realized with MPI. The parallelization of PALM and its performance are documented e.g. by Raasch and Schröter (2001) and Schröter (2003) and do not need to be discussed further at this point.

All simulations in the present study were carried out on the SGI Altix supercomputers of the HLRN[4] in Hannover and Berlin.

[3] Open Multi-Processing, visit `http://www.openmp.org`

[4] Norddeutscher Verbund für Hoch- und Höchstleistungsrechnen (The North-German Supercomputing Alliance)

3 Simulation Setup for the "Golden Days" of the LITFASS-2003 Experiment

3.1 Model initialization and driving mechanism

There are several LES studies that investigated surface heterogeneities. Most of them used 1D or 2D idealized heterogeneities with arbritary surface forcings. Some studies, for instance Hechtel et al. (1990) and Avissar and Schmidt (1998) used measurement data for initializing their LES models with idealized surface heterogeneities. During the last years, LSM and SVAT models, coupled to LES models have often been used to prescribe the surface forcing for idealized heterogeneities (e.g. Patton et al., 2005; Courault et al., 2007 and Huang et al., 2009). Real heterogeneities have been prescribed for example by surface temperatures from airborne measurements (Bertoldi et al., 2008) or by satellite data for initializing a coupled SVAT-LES model (e.g. Albertson et al., 2001; Kustas and Albertson, 2003). Uhlenbrock (2006) as well as the studies of Prabha et al. (2007) and Huang et al. (2008) used surface heat fluxes, derived from energy balance stations to prescribe realistic surface heterogeneities. This approach is also used in the present study. In contrast to the implementation of SVAT models, this technique is not able to explicitly simulate processes of surface and vegetation. Reen et al. (2006) stated, that the use of LSM/SVAT models is only profitable in case of well-defined input parameters, which is usually difficult to achieve. Heinemann and Kerschgens (2006) used a mesoscale model with a grid resolution of $250\ \mathrm{m}$, coupled to a SVAT model, to simulate the surface fluxes of selected days for the LITFASS experiment. They found a bias (defined as SVAT model $-$ measurements) of $70\ \mathrm{W/m^2}$ for the sensible heat flux, but no significant bias for latent heat flux and net radiation. However, in the present study, the feedback processes are accounted for by using measurements, which already include the realistic feedbacks. Thus, the prescribed fluxes can be assessed as applicable, since, even though they might not resemble the actual fluxes, they suffice the intended purpose to study the effects of SCs.

3.1.1 Specification of the surface heterogeneity

The LITFASS area (LFA) can be divided into several land use classes that hold different characteristics. Since the distribution of these characteristics follows the actual land surface properties in the LFA, the heterogeneities can be called realistic. The map in Fig. 3.1 shows the land use classes in the LITFASS and surrounding area, derived from a modified CORINE[1] data set. Displayed is a $40\ \mathrm{km} \times 40\ \mathrm{km}$ patch, centered around the LFA ($20\ \mathrm{km} \times 20\ \mathrm{km}$). The CORINE data set contains 44 different land use classes with a grid spacing of $100\ \mathrm{m}$, from which 16 were found to be dominant in the greater LITFASS area. For simplification, the classes "pastures" and "natural grasslands" were merged into the class "grass". The forest patches "mixed forest", "broad-leaved forest" and "coniferous forest" as well as artifical areas (such as settlements) were merged into the class "forest". The latter is valid since settlements

[1] Abbr. "Coordinated Information on the European Environment", published by the European Environment Agency (`http://www.eea.europa.eu/publications/COR0-landcover`)

exhibit similar values of heat fluxes and roughness properties as forest areas (Beyrich et al., 2004). Agricultural areas were treated as triticale/rye, since this was the dominant type in the greater LITFASS area according to Beyrich et al. (2004). For the LFA itself, the tilled fields were observed by staff of the MOL, subdivided into land use classes and georeferenced. The result is shown in Fig. 3.1, containing 7 different land use classes: water, wood, rape, triticale, corn (maize), barley and grass. A statistical distribution of the land use classes in the greater LITFASS area is shown in Tab. 3.1. Especially Lake Scharmützel in the north, the large forest patch in the west as well as the agricultural dominated area in the east of the LFA will be of major importance for the simulation results.

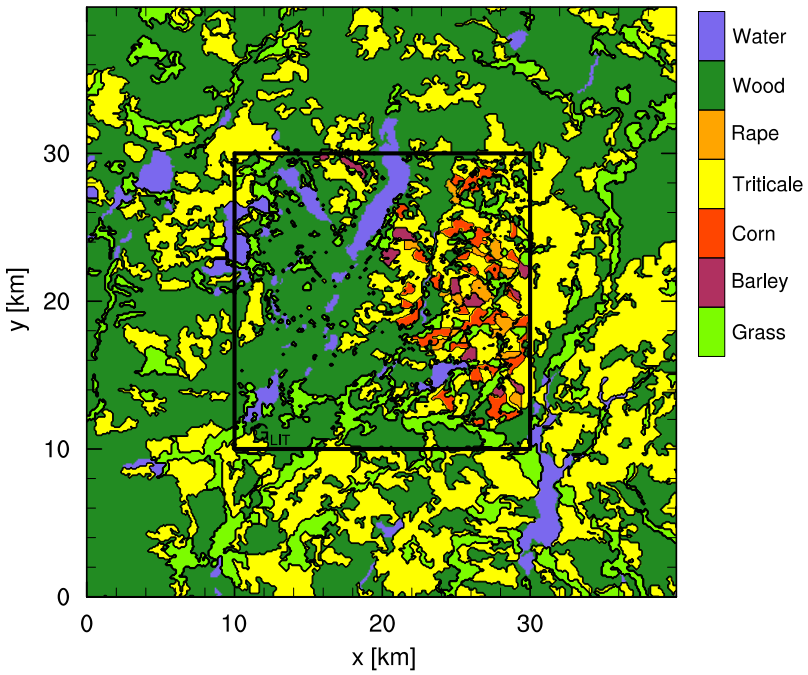

Figure 3.1: Map of the (simplified) land use classes in the greater LITFASS area. The framed area represents the LFA.

Land use class	Incidence [total]	Incidence [%]
Water	6505	4
Wood	86356	54
Rape	962	0.6
Triticale	46620	29
Corn	2006	1
Barley	692	0.4
Grass	16859	11

Table 3.1: Distribution of simplified land use classes in the greater LITFASS area of size $40\ \mathrm{km} \times 40\ \mathrm{km}$

Unless otherwise noted, all horizontal figures will show the LFA since the surrounding areas suffer from boundary effects as will be further discussed in section 4.1. The labels of the axes will thus begin with $0\ \mathrm{km}$ and end at $20\ \mathrm{km}$.

3.1.2 Initialization and forcing of the simulations

During the LITFASS-2003, several energy balance stations were located on the different land use classes. The quality control was carried out using different methods, for instance sensor comparison/calibration and assigning quality flags with the method of Foken and Wichura (1996). For a detailed description please refer to Beyrich et al. (2006a) and Mauder et al. (2006).The quality assurance showed, that the measurements were representative for the respective land use class. Therefore, the local measurements can be treated as averaged values and linked to the land use class in the LFA. Regional differences of plant characteristics such as height cannot be considered. Beyrich et al. (2004) showed that values of the sensible and latent heat fluxes from the energy balance stations (via eddy-covariance technique) do not show significant differences on equal land use classes, thus, in the study of Uhlenbrock (2006) as well as in this study, the fluxes from the local measurements were prescribed to all patches of the same land use class. To obtain better statistics, measurements over equal land use classes were averaged arithmetically. However, this forms an idealization to a certain degree. Please note, that the sensible surface heat flux will hereafter also simply be referred to as *surface heat flux*, since it is the dominant forcing for the boundary layer development.

Uhlenbrock (2006) stated, that the heat fluxes do not close the energy balance (the well-known imbalance of the energy balance), but showed that the prescribed fluxes yield to a similar boundary layer development in comparison with measurement data (e.g. radiosondes). Foken et al. (2009) discussed small-scale SC as a possible cause for the imbalance. The closure problem will thus not be further discussed at this point.

The complete initialization and driving mechanism of PALM was carried out as follows:

- As already mentioned, the eddy-covariance fluxes of sensible and latent heat from energy balance stations were prescribed to the land use classes and constituted the main forcing. Since this forcing varies in time, values were available half-hourly. To avoid discontinuous step functions, the values are interpolated each minute of simulation time, which can be mathematically written as

$$\overline{w'\Phi'}_0(x,y,t) = \overline{w'\Phi'}_0(x,y,t-\delta t) + \frac{\delta t}{1800\ \mathrm{s}}\left[\overline{w'\Phi'}_0(x,y,t+1800\ \mathrm{s}-\delta t)) - \overline{w'\Phi'}_0(x,y,t-\delta t)\right] . \tag{3.1}$$

  Here, the quantity Φ represents either θ (sensible heat flux) or q (latent heat flux), while $\delta t = 60, 120, \cdots, 1800$ s is the time since the last reference point.

- The bottom boundary of the model domain was assumed to be flat and was referenced to 73 m AMSL, which is approximately the average height of the LFA.

- Besides the surface fluxes, the heterogeneity is characterized by a roughness length z_0, which was estimated by $z_0 \approx 0.1 \cdot$ crop height (after Shuttleworth et al., 1997). The resulting two-dimensional field of z_0 accounts for the effect of friction, which leads to shear of the mean wind and thus to production of TKE (e.g. Stull, 1988). Areas of large z_0, such as forest areas, exhibit a much higher generation of TKE than for instance lakes with a small z_0. The canopy layer itself was thus not simulated.

- The initial values of surface temperature and humidity were calculated for each land use class from the measurements of the energy balance stations. During the simulations, the surface values are implicitely derived from the prescribed fluxes.

- Initial profiles of temperature and humidity were calculated from radiosonde data. The resulting profiles were subsequently recomposed by linear segments to make the profiles

consistent with the user interface of PALM. Since the radiosondes did not provide data for height levels below 112 m AMSL and the profiles are used for the entire model domain, a linear interpolation between the heterogeneous surface temperature (and humidity) and the near-surface temperature inversion z_{si} was carried out:

$$\Phi(x,y,z) = \Phi(x,y,0) + \frac{z}{z_{si}} \left(\overline{\Phi}(z_{si}) - \Phi(x,y,0) \right) \ , \quad \forall z \leq z_{si} \ , \tag{3.2}$$

where Φ is either θ or q. The values of z_{si} varied for the "Golden Days" between 75 m and 175 m and were obtained from point measurements at MOL. The point measurements of $\Phi(z_{si})$ were assumed to be respresentative for the entire area and are thus regarded as horizontal mean values.

- A one-dimensional precursor run over 10 days of simulation time was carried out to generate a steady-state wind profile. Data from radiosondes and a tropospheric wind profiler was originally used by Uhlenbrock (2006) to initialize one-dimensional precursor runs to estimate adequate wind profiles that are in accordance with tower measurements at $z = 100$ m. The resulting prescribed wind velocities are listed in Tab. 3.3 and were used in the present study as well.

- In some cases, a large-scale subsidence was applied by prescribing a subsidence velocity $w_s(z_{max})$ at the top of the model domain which was interpolated down to the surface, where $w_s(0) = 0$. This was realized analogous to Letzel and Raasch (2003) by correcting the tendency term for the potential temperature (tend_θ) in PALM as follows:

$$\text{tend}_\theta(x,y,z) = \text{tend}_\theta(x,y,z) - w_s(z) \cdot \frac{\partial \theta(x,y,z)}{\partial z} \tag{3.3}$$

  In this way, the stabilizing effect of the large-scale subsidence was directly applied without affecting the turbulent flow. Tab. 3.3 shows the applied subsidence velocities for the LITASS simulations.

3.2 Synoptic conditions during the "golden days" and case definition

3.2.1 Synoptic conditions

The synoptic conditions have a strong effect on the boundary layer turbulence and SCs. First of all, suitable conditions for the simulation with PALM are characterized by undisturbed radiation and little advection. In the presence of clouds, the incoming radiation shows a high spatial variability that is superimposing the surface heterogeneity. An overcast sky eliminates the influence of the land use classes to a great extent. The effect of advection by background wind, on the one hand, "smears" the heterogeneity signal. On the other hand, advected air masses are influenced by areas of different synoptic conditions like the Mediterranean Sea (hot and moist air) or Northern Europe (cold air). Since cyclic boundary conditions in PALM cannot account for advection, a small background wind is prefered. Five days were selected by Uhlenbrock (2006) according to the restrictions mentioned above. Four of these days were investigated in the present study: 05/30/03, 06/02/03, 06/13/03 and 06/17/03, hereafter referred to as the "Golden Days".

A selection of synoptic observations during the "Golden Days" are listed in Tab. 3.2 (from Beyrich et al., 2004). All days are characterized by temperatures between 13 °C and 29 °C and

light winds between 2 m/s and 6 m/s. There was no precipitation, but some cirrus and cumulus clouds were present in the daytime in three cases, which were not taken into account in the LES.

Date	Weather conditions		Temp. [°C]		Cloud cover	Wind [m/s]
	High	Surface	T_{min}	T_{max}		
05/30/03	Anticyclonic flow, ridge with axis from Scandinavia to Benelux	High over Belarus, ridge over Middle England, low pressure differences over Middle Europe	13	28	Clear sky	2 – 3 ESE
06/02/03	Influence of a strong ridge from Central Europe to the Norwegian Sea	SW-side of a high over the Baltic Sea	14	29	0 – 2 Ci, from 10 UTC 1 – 2 Cu	3 – 4 ESE
06/13/03	In the area of a zonal front	Rising high pressure influence from NW, advection of fresh maritime air	15	24	Overcast at 5 UTC, to 1 – 2 Cu/Sc from 7 – 9 UTC	3 – 4 NW → 5 – 6 W
06/17/03	Approaching and passing of a weak ridge from Middle Europe to the North Atlantic Ocean	West side of a High pressure zone from Sweden to East Europe	13	25	0 – 2 Cu/Sc/Ci, from 8 UTC 1 – 2 Cu, from 10 UTC Ci, thickening	2 – 3 ENE

Table 3.2: Synoptic conditions during the "Golden Days"

3.2.2 Case definition

Tab. 3.3 shows some model setup properties, such as prescribed background wind and duration. It is apparent that the west-east wind direction component ($|u|$) is dominant for all simulations. The prescribed wind velocity varies between 2 m/s (hereafter also called weak wind case) and 6 m/s. Despite the fact that 6 m/s corresponds to a moderate breeze (Beaufort scale), the latter will be called a high background wind. The four simulations are hereafter referred to as cases B3005, B0206, B1306 and B1706. Homogeneous control runs (HCR) with an spatially averaged but temporally varying surface heat flux according to Fig. 4.4 are called BH3005, BH0206, BH1306 and BH1706, respectively.

The results of section 4.1 will show that it is compulsory to use additional border areas to each side of the LFA owing to the cyclic boundaries and depending on the prescribed wind velocity. Therefore, the total horizontal model domain ($x \times y$) varied between $40\ \mathrm{km} \times 40\ \mathrm{km} = 1600\ \mathrm{km}^2$ and $56\ \mathrm{km} \times 56\ \mathrm{km} = 3136\ \mathrm{km}^2$ (see Tab. 3.3). Due to this large domain size and the fact, that for each simulation (including HCR) 16 ensemble runs were necessary (see section 3.3 for further explanations), a grid spacing of 100 m for the horizontal ($\Delta x, \Delta y$) and 50 m for the vertical direction (Δz) was chosen. About 80 grid points were used in the vertical direction and a stretch level ($\gg$ boundary layer height) was defined. Above the stretch level the vertical grid was

Case	Date	Simulation time Start [UTC]	Simulation time End [UTC]	ff [m/s]	dd [°]	Domain [km × km]	$z_{i,max}$ [m]	$w_{*,max}$ [m/s]	$w_s(z_{max})$ [m/s]
B3005	05/30/03	5 : 00	17 : 00	2.0	90	40×40	2200	2.4	-0.01
B0206	06/02/03	5 : 00	17 : 00	4.0	113	48×48	3050	3.0	-
B1306	06/13/03	4 : 30	17 : 00	6.0	320	56×56	2400	2.3	-
B1706	06/17/03	4 : 30	17 : 00	3.2	110	48×48	2400	2.7	-0.005

Table 3.3: Properties of the LITFASS simulations. $z_{i,max}$ and $w_{*,max}$ are results of the simulations. The domain size refers to the horizontal extent of the model.

stretched to save computational time in the free atmosphere. The overall number of grid points thus varied between $400 \times 400 \times 80 \approx 1.2 \cdot 10^7$ and $560 \times 560 \times 80 \approx 2.5 \cdot 10^7$. Uhlenbrock (2006) used up to $1.2 \cdot 10^7$ and reported that a higher grid resolution does not yield an improvement by comparing profiles of a reference simulation with $\Delta x,y = 50$ m and $\Delta z = 25$ m. Within the scope of the present study, three simulation cases with $\Delta x,y = 20$ m and $\Delta z = 10$ m were performed. 8 ensemble runs were carried out for each case (homogeneous surface, heterogeneous surface, heterogeneous surface with topography). The results of the simulations showed that there is no significant modification of the SCs due to the higher resolution or the weak-developed topography. The proposed grid resolution ($\Delta x,y = 100$ m, $\Delta z = 10$ m) is therefore assumed to be sufficient.

3.3 Quantitative measures of heterogeneity induced quantities

In order to isolate the effects of surface heterogeneities, Uhlenbrock (2006) used an ensemble-averaging method that shall be recapitulated here briefly. It is based on the separation of atmospheric variables into global-, meso- und small-scale part. The method is described for a constant surface forcing.

Chen and Avissar (1994a) used a mesoscale model which is able to directly separate the mesoscale and small-scale partitions, since the model calculates both fractions explicitly. Thus, a quantity Φ can be separated as follows:

$$\Phi(x,y,z,t) = \overline{\Phi}(z,t) + \widetilde{\Phi'}(x,y,z,t) + \Phi''(x,y,z,t) \quad , \tag{3.4}$$

where $\overline{\Phi}$ is the large-scale (global) average, $\widetilde{\Phi'}$ is the resolved mesoscale deviation from the global average and $\Phi''(x,y,z,t)$ is the subgrid-scale turbulent part. Owing to the fact that LES resolve both, mesoscale and small-scale turbulence, this method had to be modified. Patton et al. (2005) used a LES model to investigate 1D heterogeneities and used the phase average to separate the heterogeneity induced fraction. The underlying equation reads:

$$\Phi(x,y,z,t) = \overline{\Phi}(z) + \widetilde{\Phi'}_p(x,z) + \Phi''(x,y,z,t) \quad , \tag{3.5}$$

where $\widetilde{\Phi'}_p(x,z)$ is the phase average, representing the heterogeneity induced partition and Φ'' is called *background turbulence* (contains resolved and subgrid-scale portions). For realistic heterogeneities, however, both concepts are not applicable, neither explicit separation nor phase-averaging. Hence, Uhlenbrock (2006) used an ensemble of 8 simulations for each case. At the beginning of each simulation random perturbations of the velocity fields from a random generator are used to initiate turbulence. For each ensemble run these perturbations were

changed by modifying the random generator. This leads to a totally different local development of turbulent structures because eddies are interacting non-linear, which is already present for smallest modification of the initial state. Statistically, the turbulence development is equivalent and the choice of random perturbations is not affecting the horizontal averaged profiles. An ensemble-averaging is thus able to filter the heterogeneity induced (mesoscale) partition by deleting the small-scale fraction. For an ensemble average over N runs, the following relations are valid:

$$\frac{1}{N}\sum_{i=1}^{N}\langle\overline{\Phi}_i\rangle = \langle\overline{\Phi}\rangle \approx \overline{\Phi} \quad , \tag{3.6}$$

$$\frac{1}{N}\sum_{i=1}^{N}\langle\widetilde{\Phi'}\rangle = \langle\widetilde{\Phi'}\rangle \approx \widetilde{\Phi'} \quad , \tag{3.7}$$

$$\frac{1}{N}\sum_{i=1}^{N}\langle\Phi''\rangle = 0 \text{ for } N \to \infty \quad . \tag{3.8}$$

Applied to Eq. 3.5, heterogeneity induced quantities can be calculated as follows:

$$\widetilde{\Phi'}(x,y,z) = \frac{1}{N}\sum_{i=1}^{N}\left(\langle\Phi(x,y,z)\rangle - \langle\overline{\Phi}(z)\rangle\right) \quad . \tag{3.9}$$

The definition of Patton et al. (2005) can thus be modified for the LITFASS simulations with complex heterogeneities:

$$\Phi(x,y,z,t) = \overline{\Phi}(z) + \widetilde{\Phi'}(x,y,z) + \Phi''(x,y,z,t) \quad . \tag{3.10}$$

Please note, that $\widetilde{\Phi'}$ is not available for every time step, since time-averaging ($\langle\ldots\rangle$) is necessary. It will hereafter be referred to as *heterogeneity induced quantity* or *mesoscale quantity*.

A boundary layer over homogeneous surfaces should yield to $\widetilde{\Phi'} = 0$, since no heterogeneity effects are present. However, Eq. 3.9 is only valid for $N \to \infty$ and it is not possible to delete the background turbulence completely. For the LITFASS simulations, $N = 8$ was found to be sufficient, based on the results of a homogeneous simulation with a background wind of 6 m/s, shown in Fig. 3.2. Fig. 3.2 (a) shows that the height-averaged ($0.0 - 1.0\ z_i$) standard deviation of $\widetilde{w'}$ decreases from 11.5 % to 4.2 % with an asymptotic decline. It proves that more ensemble runs would not further decrease the standard deviation to a significant amount. Fig. 3.2 (b) and (c) display the corresponding fields of $\widetilde{w'}$ for $N = 1$ and $N = 8$ at height level 0.4 z_i, time-averaged over 1 h. While for $N = 1$ updraft structures are clearly visible, for $N = 8$ the bulk of these turbulent structures have been successfully filtered by the ensemble-averaging method.

Eq. 3.10 is also applicable for (vertical) turbulent fluxes $w\Phi$. Following Chen and Avissar (1994a), the turbulent fluxes can be decomposed:

$$w\Phi = \overline{w}\overline{\Phi} + \widetilde{w'}\widetilde{\Phi'} + w''\Phi'' + \overline{w}\widetilde{\Phi'} + \widetilde{w'}\overline{\Phi} + \overline{w}\Phi'' + w''\overline{\Phi} + \widetilde{w'}\Phi'' + w''\widetilde{\Phi'} \ . \tag{3.11}$$

The ensemble average simplifies Eq. 3.11 to

$$\widetilde{w\Phi} = \overline{w}\overline{\Phi} + \widetilde{w'}\widetilde{\Phi'} + \widetilde{w''\Phi''} + \widetilde{w'}\overline{\Phi} + \overline{w}\widetilde{\Phi'} \ . \tag{3.12}$$

Since the global contribution of the mesoscale flux is of major interest, a horizontal average is carried out. The resulting relations ($\overline{\overline{\Phi}} = \overline{\Phi}$, $\overline{\widetilde{\Phi'}} = 0$, $\overline{\widetilde{w\Phi}} = \overline{w\Phi}$ and $\overline{\widetilde{w''\Phi''}} = \overline{w''\Phi''}$) are further improving the equation to

$$\overline{w\Phi}(z) = \overline{w}(z)\overline{\Phi}(z) + \overline{\widetilde{w'}\widetilde{\Phi'}}(z) + \overline{w''\Phi''}(z) \ . \tag{3.13}$$

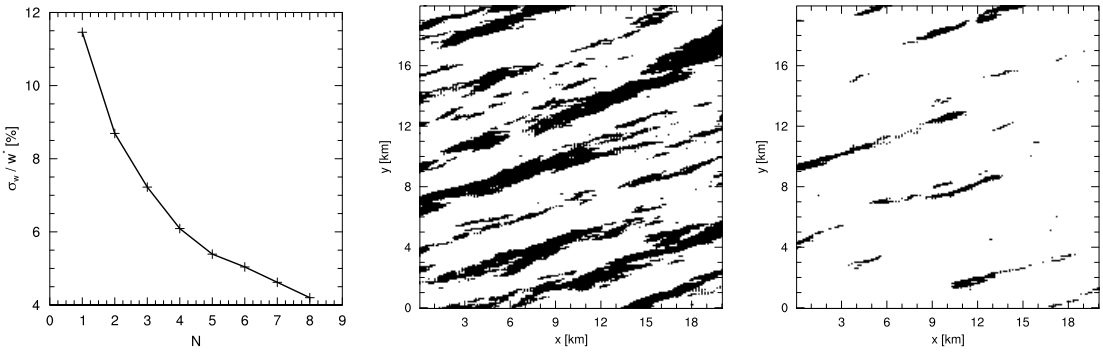

(a) σ_w (b) $N = 1$ (c) $N = 8$

Figure 3.2: Illustration of the consequences of the ensemble average. Shown is the height-averaged standard deviation of the vertical velocity in dependency of the number of ensemble runs N (a) and horizontal cross-sections of the vertical velocity $w > 0.08\ w_*$ at $z = 0.4\ z_i$ for $N = 1$ (b) and $N = 8$ (c). The data was time-averaged over 1 h.

$\overline{w\Phi}$ is the horizontal averaged total flux which can be decomposed into the global part $\overline{w}(z)\overline{\Phi}(z)$, the mesoscale part $\widetilde{\overline{w'}}\widetilde{\overline{\Phi'}}(z)$ and the small-scale turbulent part $\overline{w''\Phi''}(z)$. In the present simulations, the global part is zero, since the horizontal average is $\overline{w} = 0$ due to continuity reasons. This holds also for cases where a large-scale subsidence was applied, since this was implicitely done by correcting the potential temperature.

4 Simulations for the LITFASS-2003 Experiment Data

4.1 Sensitivity study on the effect of horizontal boundary areas

For simulating the turbulent flow over the LFA, cyclic boundary conditions in the horizontal directions were used in PALM. Hence, inflowing turbulent structures are exactly matching the corresponding outflowing structures. For the case of a real surface heterogeneity, this is leading to an unrealistic flow field because the incoming flow should be affected by the surface structure in the upstream region instead of the outflowing region. Therefore, the LFA domain was not sufficient to simulate the realistic CBL, which would develop in situ. The area was enlarged in all horizontal directions to avoid boundary effects in the analysis of the LFA. Due to the additional border area, especially in upstream direction, the flow is affected by the surface heterogeneity before it reaches the analysis area and should be less dependent on the outflow by the cyclic boundaries. Uhlenbrock (2006) studied the influence of additional boundary areas up to $14\ \mathrm{km}$ with $N = 4$ ensemble runs and a wind velocity of $5\ \mathrm{m/s}$. As a result, Uhlenbrock stated, that an additional boundary area of $10\ \mathrm{km}$ would be sufficient. The present sensitivity study attempts to reassess and enhance the results of the former study by varying the wind velocity as well as the border area. Due to the capability of today's supercomputers, it was feasible to use 8 ensemble runs, on the contrary to the study of Uhlenbrock (2006), whose extent was restricted by computational costs.

The key aspect of the present sensitivity study concerning lateral boundary areas is the influence of advection on the flow over the LFA and the question how large the border area actually has to be in order to achieve realistic results, because the heterogeneity of the border area itself may have a strong effect on the turbulent flow over the analysis area.

For answering this question, the heterogeneity induced quantity $\widetilde{\Phi}'$ can be used according to section 3.3. By increasing the border area, the standard deviation of $\widetilde{\Phi}'$ should converge to a final value which is not changing with a further increase of the border area.

Simulation setup

For the sensitivity study, a grid resolution of $100\ \mathrm{m} \times 100\ \mathrm{m} \times 50\ \mathrm{m}$ was used according to Uhlenbrock (2006). With the LFA of size $20\ \mathrm{km} \times 20\ \mathrm{km}$ and border areas of $2\ \mathrm{km}, 6\ \mathrm{km}, 10\ \mathrm{km}, 14\ \mathrm{km}, 18\ \mathrm{km}$ (and partially $22\ \mathrm{km}$) which were applied to three sides of the lateral boundaries (and $2\ \mathrm{km}$ to the downstream boundary), the total numerical model domain varied between $240 \times 240 \times 80 \approx 4.6 \cdot 10^6$ and $420 \times 640 \times 80 \approx 21.5 \cdot 10^6$ grid points. The land surface heterogeneity was set according to the modified and enhanced CORINE data set (Fig. 3.1 shows the LFA with a border area of $10\ \mathrm{km}$). Please note that the CORINE data from 2000 was frequently updated, i.e. post-processed, until 2007 and thus the additional borders of $14\ \mathrm{km}, 18\ \mathrm{km}$ and $22\ \mathrm{km}$ had to be mapped on the available $40\ \mathrm{km} \times 40\ \mathrm{km}$ map that was used by Uhlenbrock (2006). Due to projection updates in the CORINE data set, some though negligible but existent differences between the two maps occured. For producing strong effects

Land use class	$\overline{w'\theta'}_0$ $\left[\mathrm{K}\frac{\mathrm{m}}{\mathrm{s}}\right]$	$\overline{w'q'}_0$ $\left[\frac{\mathrm{kg}}{\mathrm{kg}}\frac{\mathrm{m}}{\mathrm{s}}\right]$
Grass	0.15	$4.83 \cdot 10^{-5}$
Barley	0.23	$3.36 \cdot 10^{-5}$
Corn	0.15	$3.5 \cdot 10^{-5}$
Triticale	0.24	$3.8 \cdot 10^{-5}$
Rape	0.18	$6.3 \cdot 10^{-5}$
Wood	0.39	$2.2 \cdot 10^{-5}$
Water	-0.003	$3.1 \cdot 10^{-5}$

Table 4.1: Prescribed sensible and heat fluxes for each land use class for the border area sensitivity study. The fluxes are assigned and approximated by measurements of 05/30/2003 at about noon.

of the surface heterogeneity, constant sensible and latent surface heat fluxes were prescribed to each land use class for 6 h of simulation time. The fluxes were assigned by approximated values of measurements about noon at the golden day of 05/30/2003 (see Tab. 4.1). In comparison with the other golden days, the 05/30/03 led to the strongest secondary circulation in the CBL (Uhlenbrock, 2006), with the highest heat fluxes at about noon and thus was an adequate thermal forcing for the sensitivity study. The roughness lengths were approximated like in the former LITFASS simulations (see section 3.3) with $z_0 \approx 0.1 \cdot$ crop height.

The geostrophic wind velocity v_g in the LITFASS experiment data varied between 2 m/s and 6 m/s (Tab. 3.3). Consequently, three cases were chosen for the study: 2 m/s, 4 m/s and 6 m/s. The effect of advection strongly depends on the wind velocity. Roughly speaking, the strength of the heterogeneity induced circulations decreases with higher wind speed, in spite of a strong dependence of the orientation of the heterogeneities on the geostrophic wind (Raasch and Harbusch, 2001; Avissar and Schmidt, 1998) . Hence, a wind speed of 6 m/s should be sufficient to cover all cases with a significant heterogeneity induced effect. A wind direction of 90 ° (east) was chosen, because during most of the golden days winds from eastern directions were observed (Tab. 3.2). Due to this choice for the wind direction, the border area in the west of the LFA becomes more or less unimportant. The inflowing turbulence should be affected by the upstream region only. But the western border area still plays a role for the development of turbulent structures in the outflow region of the LFA. For allowing a more realistic development, the additional border was set to a constant value of 2 km (actually, it varied owing to numerical reasons from $1.1 - 2.0$ km), while an equal-sized border area ($2 - 22$ km) was applied to the other three borders. The maximum additional border of 22 km was only applied for a geostrophic wind velocity of 6 m/s, because it was not expected to be relevant for cases with lower wind speed and thus a smaller effect of advection. So, the actually used model domain was in the range of $24 - 44$ km along the x-direction and $24 - 64$ km along the y-direction.

Resulting from this setup, 16 cases were simulated as shown in Tab. 4.2 over 6 h of simulation time. For each case, 8 ensemble runs were carried out, following the ensemble-averaging method of section 3.3 (see also Fig. 3.2). Therefore, the ensemble-averaged fields could be compared directly, which was not possible with only 4 ensemble runs in the former sensitivity study of Uhlenbrock (2006).

Unlike the sensitivity study of Uhlenbrock (2006), the simulations in the present study used humidity as well as Coriolis force. Furthermore, a different wind direction was used. The vertical profile of potential temperature was initialized by a slightly stable stratification of 0.08 K/100m

Simulation	Border area [km]						v_g [m/s]		
	2	6	10	14	18	22	2	4	6
A022	X						X		
A062		X					X		
A102			X				X		
A142				X			X		
A182					X		X		
A024	X							X	
A064		X						X	
A104			X					X	
A144				X				X	
A184					X			X	
A026	X								X
A066		X							X
A106			X						X
A146				X					X
A186					X				X
A226						X			X

Table 4.2: List of PALM simulation cases for different geostrophic wind v_g velocities and border areas used in the present study.

up to a height of 1200 m and stable stratification above with a gradient of 0.74 K/100m to provide a fast growth of a CBL. A moisture decrease with height like in a typical CBL (cf. Stull, 1988, Fig. 11.1) in agreement with the results of Uhlenbrock (2006), was prescribed (gradients of $-0.0001/100$ m up to 1200 m height, $-0.001/100$ m up to 1500 m, and $0.0/100$ m above), respectively. The differences between the setup compared to Uhlenbrock (2006) are listed in Tab. 4.3.

Setup	dd [°]	ff [m/s]	Border area [km]	Ensemble runs	Other features
Present study	90	$2-6$	$2-18(22)$	8	Coriolis force, humidity
Uhlenbrock (2006)	-90	5	$2-14$	4	-

Table 4.3: Sensitivity study setup differences between the present study and Uhlenbrock (2006).

Simulation results

For quantifying the effect of the additional border area on the boundary layer circulation, the height-averaged standard deviations σ_w were calculated analogous to the simulation with a homogenous heating and $N = 1-8$ ensemble runs (see section 3.3). The results show an asymptotic decline for all cases (Fig. 4.1). With $N = 8$ ensemble runs, the approaching process is almost completed, thus the amount of ensemble runs seems to be sufficient for further analysis. Furthermore, the final value of σ_w is approaching a much higher value than in the homogeneous simulation. This is an effect of the heterogeneities, because σ_w can be seen as a measure for the strength of the circulations in the boundary layer, which will reach higher values, if circulations

occur. Moreover, the comparison of the three cases with different velocities (Fig. 4.1 (a), (b) and (c)) shows that a higher wind speed is leading to a decreased value of σ_w. For $2\ \mathrm{m/s}$, the final value is in the range of $20-21$ %, while the final value for $4\ \mathrm{m/s}$ is of $9-14$ % and $8-11$ % for $6\ \mathrm{m/s}$, respectively. It also contains the background turbulence, thus it is unclear if the deviations between the simulations with different border areas are caused by the heterogeneity induced effect or the background turbulence. This result is in agreement with the former studies of Avissar and Schmidt (1998), Raasch and Harbusch (2001) and Uhlenbrock (2006).

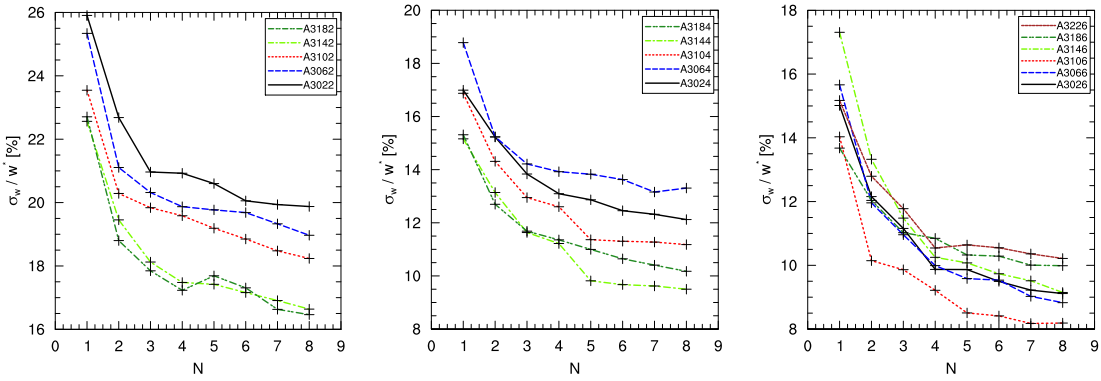

(a) $v_g = 2\ \mathrm{m/s}$ (b) $v_g = 4\ \mathrm{m/s}$ (c) $v_g = 6\ \mathrm{m/s}$

Figure 4.1: Height-averaged $(0.0-1.0\ z_i)$ standard deviation σ_w from the horizontal average of the vertical velocity (referring to the LFA), normalized by the characteristic velocity in the CBL, plotted against the number of ensemble runs N for different values $v_g = 2,4,6\ \mathrm{m/s}$ of the geostrophic wind. The data was time-averaged over $1\ \mathrm{h}$ after $6\ \mathrm{h}$ of simulation time.

Uhlenbrock (2006) suggested, that the difference of the curves for the individual border areas decreases with increasing the border areas, because the advection effect of the additional border should decrease with the distance from the analysis area. However, the present study cannot confirm this suggestion. Neither for a geostrophic wind velocity of $2\ \mathrm{m/s}$, nor for $4\ \mathrm{m/s}$ and $6\ \mathrm{m/s}$, a successive decrease is visible (cf. Uhlenbrock, 2006, Fig. 4.5 (a)). Hence, the key aspect of the study cannot be answered by the analysis of σ_w. Nevertheless, a detailed look at the three velocity cases yields further interesting characteristics.

Looking at Fig. 4.1 (a), a successive decrease of the standard deviation with border area increase is visible. The cases A142 and A182 have very similar standard deviations of ~ 16.5 % and a remarkable gap of ~ 1.7 % exists between A102 and A142 at $N = 8$. As a conclusion, the proposed border area of Uhlenbrock of $10\ \mathrm{km}$ for a geostrophic wind of $5\ \mathrm{m/s}$ (an even smaller border area was proposed for lower wind speeds) seems not to be sufficient for realistic simulations, especially because the gap between $10\ \mathrm{km}$ and $14\ \mathrm{km}$ shows a significant change of the circulation strength even for a low wind speed. Another feature shall be explained briefly: the increase of the standard deviation of A182 from $N = 4$ to $N = 5$. Usually more ensemble runs should reduce σ_w. Anyhow, this is not always the case. This is due to the different random perturbations in each ensemble run which have accidentally led to a similar development of turbulent elements in the LFA. This was proved by setting up a new set of ensemble runs with a different initializing of the random generator (not shown). Hence, the increase is a simulation relict and has no physical cause.

The already mentioned gap between $10\ \mathrm{km}$ and $14\ \mathrm{km}$ is also noticeable in Fig. 4.1 (b) and (c) and thus is assumed to find itself caused in the added hetereogeneity at the distance

$10-14$ km as will be discussed later on. Here, a successive decrease of the standard deviation does not appear. In Fig. 4.1 (c), the standard deviation is decreasing for border areas from 2 km ($\sigma_w = 9$ %) to 10 km ($\sigma_w = 8.1$ %) but then is increasing again from 14 km ($\sigma_w = 9.1$ %) to 22 km ($\sigma_w = 10.25$ %), while in (b) no remarkable trend is visible and the standard deviations at $N = 8$ vary between 9.5 % and 13.5 %.

In order to study the circulation structure more quantitatively, Fig. 4.2 shows cross-sections of the ensemble-averaged vertical velocity $\widetilde{w}$ in the LFA at a height level of 0.4 z_i for selected simulation cases. The weak wind cases A022, A102 and A142 display similar structures. Advection seems to have only little influence on the flow over the LFA. Furthermore, corresponding updraft structures of markable surface heterogeneities like Lake Scharmützel in the north ($x = 9-12$ km,$y = 14-20$ km), Lake Groß-Selchow in the north west ($x = 0-3$ km,$y = 9-15$ km) and a large longitudinal patch of forest area in the western part of the LFA ($x = 0-9$ km,$y = 4-6$ km) can be retrieved. As a first result, the proposed border area of 10 km is confirmed for the weak wind case. For a higher geostrophic velocity of 4 m/s (cases A104, A144 and A184 are shown), the visible correlation between surface heterogeneity and updrafts has mostly disappeared and roll-like structures have developed. As can be seen easily, the velocity field shows distinct changes with an increasing border area. While there are well-defined rolls in the cases A024, A064 and A104 (only A104 is shown), in case A144 most structures have vanished. Similar structures can be found very rarely. The simulation case A184 displays a very similar structure to A144, thus it can be assumed that the gap between 10 km and 14 km, which was discussed above, is pointing at a significant change in the flow field owing to the additional border area and that advection is a relevant factor for a geostrophic wind of 4 m/s. Fig. 4.2 (g), (h) and (i) show cross-sections for a geostrophic wind velocity of 6 m/s, respectively. Here, roll convection along the mean wind direction is the dominating feature. The location of the updraft structure is changing in the simulations with a border area smaller than 14 km significantly (not shown), while there are only minor differences between simulations with a border area of 14 km, 18 km and 22 km. Hence, the effect of advection seems to be the chief cause and a minimum border area of 14 km is suggested for all cases with stronger wind velocities.

For a more detailed analysis of the differences between the different additional border sizes, the deviation of the ensemble-averaged velocities at every horizontal grid point of the LFA of two different simulation cases with different border areas of size $b(i)$ ($b(1) = 2$ km,$b(2) = 6$ km etc.), normalized by the characteristic velocity w_* were calculated as follows:

$$\mathcal{A}_{[b(i+1),b(i)]}(x,y,z) = \frac{\mid \widetilde{w}_{i+1}(x,y,z) - \widetilde{w}_i(x,y,z) \mid}{0.5 \cdot \left(w_{_{i+1}*} + w_{i*}\right)} \qquad \text{with } i = 1,2,3,4,(5)\ . \tag{4.1}$$

Theoretically, the deviation $\mathcal{A}$ should in general become smaller and structures of deviations > 15 % should disappear with increasing border sizes, owing to the converging flow field. The deviations $\mathcal{A}_{[b(i+1),b(i)]}$ at height $z = 0.4$ z_i for the simulations with a geostrophic wind of 6 m/s are in good agreement with this (Fig. 4.3). The maximum value of $|\mathcal{A}_{[b(i+1),b(i)]}|$ decreases from 39 % to 26 %, while the structures (the shown absolute magnitude > 15 % can be seen as representative) vanish successively. The strongest decline exists between Fig. 4.3 (c) and (d) in the order of ~ 8 % and is yet another indicator for the significance of the border area between 10 km and 14 km away from the LFA. Due to the constant maximum of ~ 26 % of Fig. 4.3 (d) and (e), no further appreciable improvement is expected for a border area > 14 km, also taking into account the rising computational costs.

Another feature of the visible structures in Fig. 4.3 deserves closer attention: the orientation is longitudinal to the mean wind and most of the deviations structures are arranged in pairs of

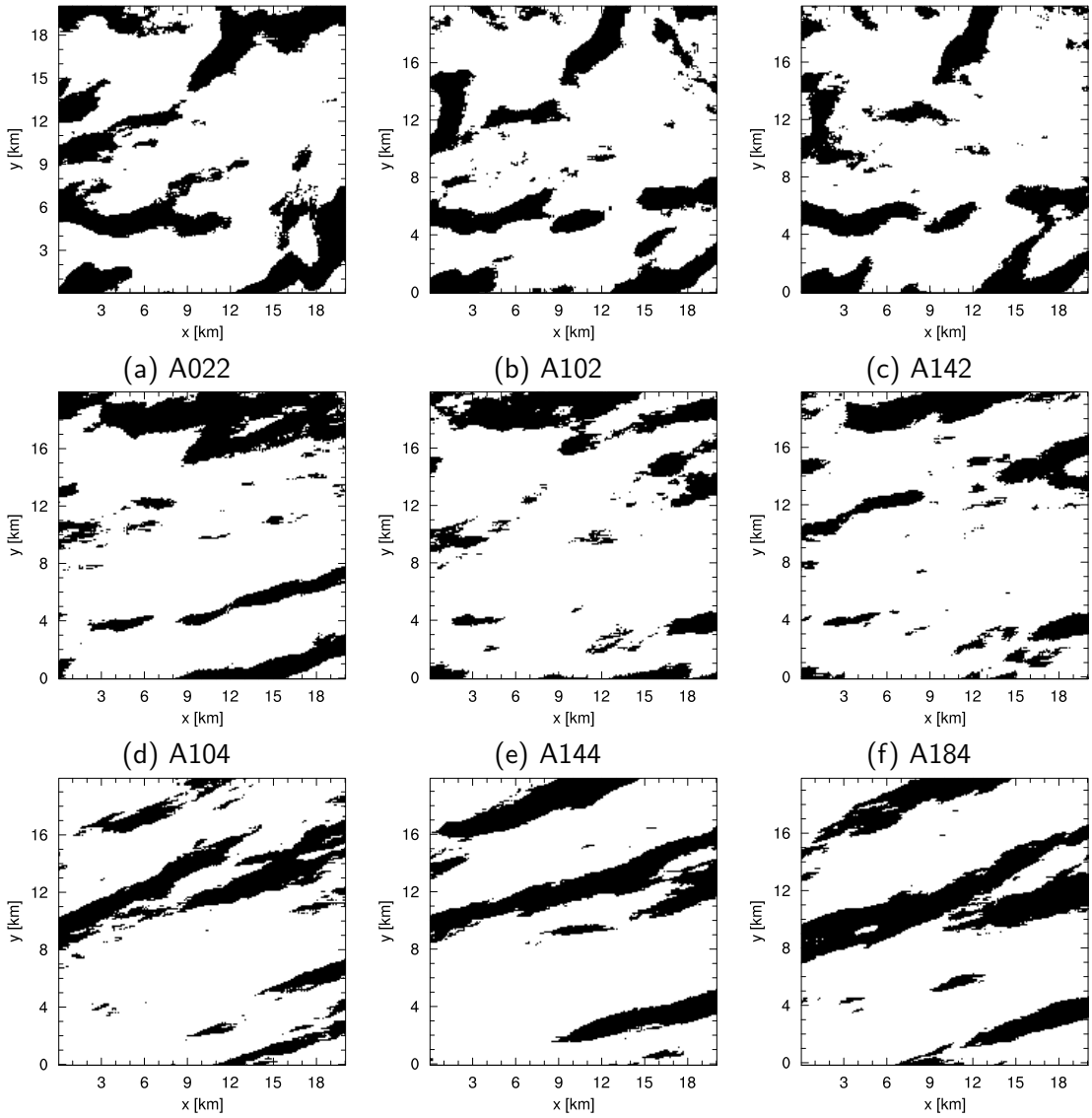

Figure 4.2: Cross-sections of the ensemble-averaged ($N = 8$) vertical velocity $\widetilde{w} > 0.08\ w_*$ in the LFA at height level $z = 0.4\ z_i$ after 6 h of simulation time for selected simulation cases. The fields are averaged over 1 h.

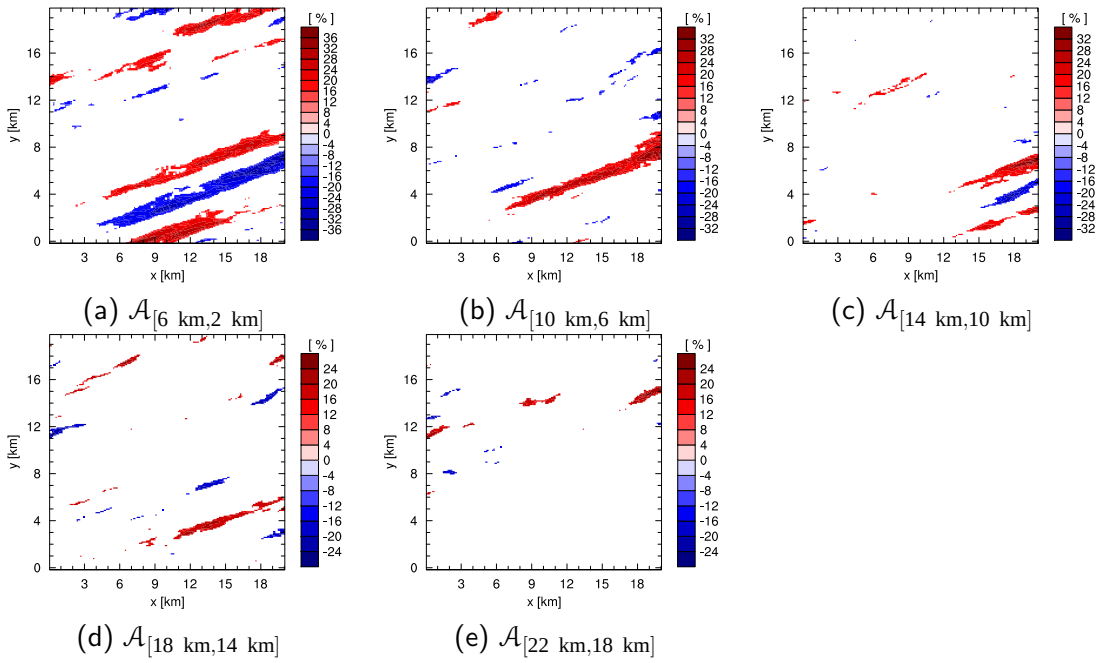

(a) $\mathcal{A}_{[6\ \mathrm{km},2\ \mathrm{km}]}$ (b) $\mathcal{A}_{[10\ \mathrm{km},6\ \mathrm{km}]}$ (c) $\mathcal{A}_{[14\ \mathrm{km},10\ \mathrm{km}]}$

(d) $\mathcal{A}_{[18\ \mathrm{km},14\ \mathrm{km}]}$ (e) $\mathcal{A}_{[22\ \mathrm{km},18\ \mathrm{km}]}$

Figure 4.3: Cross-sections of deviations of different additional border areas $\mathcal{A}_{[b(i+1),b(i)]}$ for $v_g = 6$ m/s, normalized by w_*. Only absolute values > 15 % are shown.

positive/negative deviations, for instance Fig. 4.3 (a) displays two broad bands in the southeast and Fig. 4.3 (d) smaller bands in the southwestern part. There is evidence to suggest that this feature is caused by a shift of the roll-like structures in the CBL perpendicular to the mean wind by the effect of the border area heterogeneities. This dominant characteristic was found to occur in all simulation cases, even the weak wind simulations (not shown).

Conclusions

In contrast to Uhlenbrock (2006), the present study shows, that there is an non-negligible effect of the surface heterogeneities in the border area up to 22 km due to advection, especially for wind speeds between 4 m/s and 6 m/s. For 2 m/s, advection only has a minor effect. However, the results suggest a minimum border area of 10 km for the weak wind case. A look at the extended CORINE map might be able to explain the strong effect, because the distribution of heterogeneous patches changes significantly when increasing the border area to the east, north and south to values > 10 km (not shown). In the northeast, a large patch of arable land is added, while in the east / southeast, forest is the dominating land cover. This would also explain the results of Uhlenbrock. By the choice of a mean wind from western directions, advection from surface heterogeneities in the west of the LFA was forced. This region displays more homogeneously distributed heterogeneities and therefore an effect of a remarkable change in the distribution could not be studied. This yields to the finding, that large-scale heterogeneities, even at great distance from the LFA, have to be considered by choosing a sufficient border area in the upstream direction. For further studies, border areas of 18 km for geostrophic wind velocities > 4 m/s and 14 km for 4 m/s $\geq v_g > 2$ m/s were used in agreement with the results in this section.

The question, how large the border area needs to be for realistic simulations, still remains, especially in regard to the time-dependent surface heat fluxes under realistic conditions. Since an air particle needs ~ 39 min to pass an upstream border area of 14 km with a mean velocity of

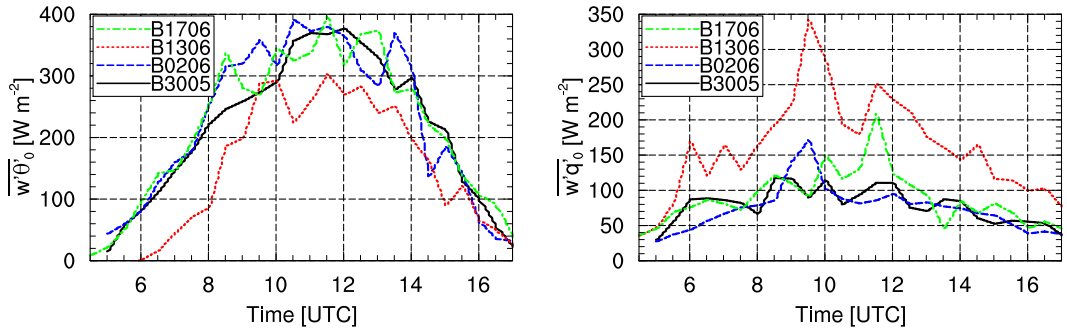

(a) Prescribed sensible surface heat flux (b) Prescribed latent surface heatlux

Figure 4.4: Time series of the horizontal average of prescribed sensible and latent surface heat fluxes for the LITFASS simulations, derived from the weighted sum of energy balance station measurements.

$6\ \mathrm{m/s}$ and a time average of $1\ \mathrm{h}$ during the ensemble-averaging process, it might be necessary to take into account a larger border area. For further studies, a $10-18\ \mathrm{km}$ border area was applied anyway, as discussed above.

The results in this section show, that the necessary additional border area in some other studies was chosen far too small. For example Prabha et al. (2007) used a horizontal model domain of size $3.5\ \mathrm{km} \times 3.5\ \mathrm{km}$ with an additional border of $1\ \mathrm{km}$ and background wind speeds of $2\ \mathrm{m/s}$ and $5\ \mathrm{m/s}$. Based on the present border area study, Prabha et al. (2007) chose a dramatically too small border area to simulate the flow over an non-repeating surface heterogeneity which clarifies the shortcomings of this study.

4.2 Boundary layer structure and secondary circulations during the "Golden Days"

The driving mechanism for the PALM simulations was discussed in section 3.1. For the border area study, a constant surface forcing was used, but for the simulation of the "Golden Days", time-depending surface fluxes were prescribed, including the diurnal cycle and the synoptic conditions (see section 3.2). Thus, the time series of the sensible and latent heat flux of the four simulations differ to a significant amount in time and magnitude. Fig. 4.4 shows the prescribed turbulent surface fluxes $\overline{w'\theta'}_0$ and $\overline{w'q'}_0$ for all simulation cases, derived from measurements of the energy balance stations. It is obvious that the prescribed sensible surface heat flux reaches higher values, typically maximum values between $300-400\ \mathrm{W/m^2}$ during the course of day, whereas the latent heat flux maxima vary between $120-325\ \mathrm{W/m^2}$. For the latter, typical values are less than $200\ \mathrm{W/m^2}$, a factor of 2 smaller than $\overline{w'\theta'}_0$. Thus the bowen ratio is between 3 and 4 at noon. Case B1306, with a bowen ratio of 1, is exceptional from this finding, owing to intense precipitation on 06/05/03 and 06/09/03. Furthermore, $\overline{w'\theta'}_0$ starts to raise comparatively late (6 UTC) under the influence of an overcast sky in the early morning hours (see Tab. 3.2) and reaches a smaller maximum value of $300\ \mathrm{W/m^2}$.

For an overview of the relative contribution and development of the heterogeneous surface, Fig. 4.5 displays the time series for each land use class for case B3005. Note that Fig. 4.4 represents the weighted sum of this time series. Fig. 4.5 (a) points out that the forest patches are the dominant land use class regarding the heat input with values up to $500\ \mathrm{W/m^2}$. The water areas show no significant contribution to the heat input and rather tend to take up energy in

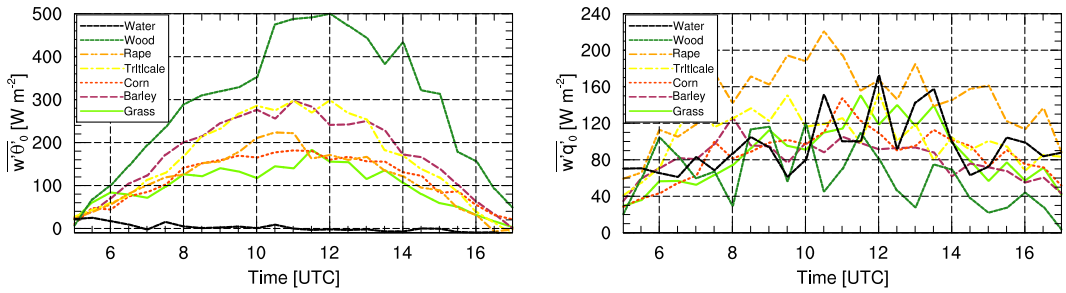

(a) Prescribed sensible surface heat flux (b) Prescribed latent surface heat flux

Figure 4.5: Time series of sensible and latent surface heat flux for the different land use classes, measured by energy balance stations.

the late afternoon, since the high heat capacity of water is leading to a lower water temperature than the near-surface air temperature when the land surface is heating up during daytime. Areas tilled with triticale and barley exhibit maximum values of $300\ \mathrm{W/m^2}$, while grass, maize (corn) and rape reach $180-230\ \mathrm{W/m^2}$. The large amplitude difference between forest and water will be of major importance for the development of SCs (section 4.2.3).

Contrary to the sensible heat flux, the latent heat flux is characterized by high fluctuations during the course of day with amplitudes up to 50 % of the total flux (e.g. forest areas). The diurnal cycle is only weakly developed and the maximum values are within the range of $100-220\ \mathrm{W/m^2}$. Summed up, the forest patches are linked to the smallest water-vapor input to the atmosphere, while rape is associated with the highest input. But due to the high fluctuations, it can be concluded that the surface is chiefly characterized by a sensible heat flux heterogeneity.

4.2.1 Time series

Due to the different synoptic conditions during each "Golden Day", the evolution of the boundary layer in the four simulations shows different features and characteristics. Fig. 4.6 shows the temporal development of scaling parameters, which were calculated according to the definitions of Wyngaard et al. (1974b), derived from MOST from horizontal averaged values as follow:

$$w_* = \left(\frac{g}{\overline{\theta}} \cdot z_i \cdot Q_0\right) \quad , \tag{4.2}$$

$$\theta_* = \frac{Q_0}{w_*} \quad , \tag{4.3}$$

$$q_* = \frac{V_0}{w_*} \quad , \tag{4.4}$$

$$t_* = \frac{z_i}{w_*} \quad . \tag{4.5}$$

Here, $V_0 = \overline{w'q'}_0$ and $Q_0 = \overline{w'\theta'}_0$. The boundary layer height z_i was calculated using the method of Sullivan et al. (1998), modified by Uhlenbrock (2006) since it was found to be more stable and yield a smoother development:

$$\begin{aligned} z_i = z \quad &, \text{ where z is the lowest height level, where } \quad \frac{\partial\theta(z)}{\partial z} > \Gamma \\ \wedge \quad \frac{\partial\theta(z')}{\partial z} \quad &\text{is maximum with} \quad \Gamma = 0.2\ \mathrm{K/100m} \quad \text{and} \quad z' \in [z, z+4\Delta z]. \end{aligned} \tag{4.6}$$

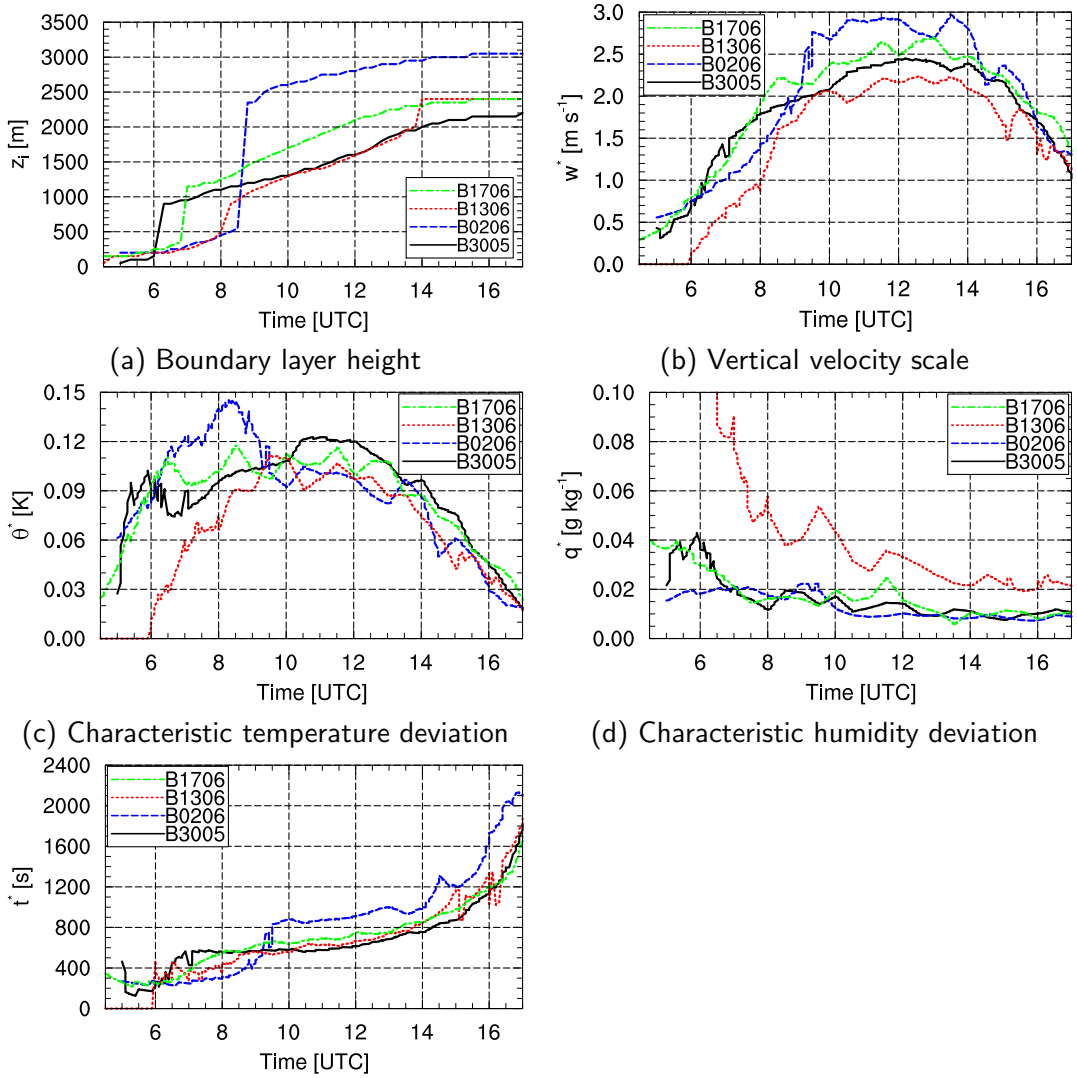

(a) Boundary layer height

(b) Vertical velocity scale

(c) Characteristic temperature deviation

(d) Characteristic humidity deviation

(e) Convective time scale

Figure 4.6: Time series of scaling parameters of the LITFASS simulations, derived from horizontal averaged variables.

The scaling parameters are valid for homogeneously heated surfaces and the proposed relation $z_i \sim \sqrt{t}$ by Wyngaard et al. (1974b) is caused by the fact that the available amount of energy at the surface remains constant while the boundary layer grows and thus more air has to be heated by this energy input. w_* is called the vertical velocity scale, representing the characteristic velocity an air parcel has, while rising from the surface to the top of the boundary layer. θ_* is the temperature scale and can be interpreted as the characteristic temperature deviation of large eddies to the ambient air. The characteristic humidity scale q_* is the humidity deviation of large eddies. t_* represents the convective time scale, the characteristic span of time an air parcel needs to rise from the surface to the top of the boundary layer. Despite the fact, that these parameters are derived for a homogeneously heated surface, they might be applied to heterogeneous cases and are often used (e.g. Patton et al., 2005; Uhlenbrock, 2006; Courault et al., 2007). Thus, the present study will use the scaling parameters, particularly z_i.

The evolution of z_i (Fig. 4.6, (a)) shows, that the boundary layer height in cases B3005 and B1306 is relatively equal around noon (1600 m and 1700 m, respectively), whereas it is higher

in cases B1706 (2300 m) and B0206 (2800 m). All simulations display markable jumps which are associated with the dissipation of nocturnal inversions with residual layers atop. Since these residual layers are nearly neutrally stratified, rising thermals can rise to the top of the residual layer and thus z_i jumps up. This process will be discussed in section 4.2.4 as well. These jumps can be found at 6 UTC, 7 UTC, 8 UTC and 8 : 40 UTC. The jump magnitude is depending on the prescribed temperature profiles (see Fig. 4.7) and varying between 400 m (B1306) and 1700 m (B1306). Noteworth is also a secondary inversion in case B1306 which is located higher and dissipating at 14 UTC, leading to a z_i jump of 400 m (see Fig. 4.7, (f)). After the nocturnal inversions have dissipated, the boundary layer is growing nearly linear until the late afternoon, when the surface forcing is decreasing and convection weakens, so that z_i reaches its maximum.

The characteristic velocity scale benefits from a high boundary layer depth because updrafts are able to accelerate over a larger vertical distance before they slow down due to the temperature inversion at the top of the boundary layer. Thus, w_* is found to be largest for case B0206 with maximum values of about 3 m/s (Fig. 4.6, (b)). The characteristic temperature deviation shows a diurnal cycle which can be directly linked to the surface heat flux (Fig. 4.6 (c), cf. Fig. 4.4, (a)). θ_* has typical values of 0.1 K. The same reason applies to the humidity deviation q_*, shown in Fig. 4.6 (d), which is connected to the latent surface heat flux (see Fig. 4.4, (b)). Owing to the fact, that B1306 offers the highest water-vapor release into the boundary layer, this case also exhibits the highest values of q_* of about 0.035 g/kg at noon.

The convective time scale is increasing slightly with time until 14 UTC before it is rapidly increasing (Fig. 4.6, (e)). The latter is caused by the dimishing surface forcing, so that a rising air parcel contains less energy (heat) to rise to the top of the boundary which is resulting in a decrease of w_* as shown in Fig. 4.6, (b). In daytime turbulence conditions, t_* typically holds values of $600 - 1000$ s and in the last hour of simulation time values up to 2100 s.

4.2.2 Vertical profiles

The good agreement of vertical profiles of the LES with measurements during the LITFASS-2003 campaign was already stated by Uhlenbrock (2006). The temporal development of potential temperature and humidity profiles shall be reported here briefly for the sake of completeness. Profiles of horizontal averaged temperature and humidity are shown in Fig. 4.7 for every 3 h of simulation time. The initial profiles can be reconstructed by the solid black lines.

Case B3005 shows a strong inversion near the surface in the early morning. At 8 UTC, this inversion has already been torn down by turbulent mixing and a CBL has developed, whose depth is about 1 km. During the course of the day, the temperature of the mixing layer rises from 292.6 K to 299.3 K, while the boundary layer height grows to ~ 2 km, in accordance with the time series of z_i (see Fig. 4.6, (a)). In the afternoon the surface forcing decreases, leading to slower heating and growth of the CBL until 17 UTC. The humidity profile in the early morning is characterized by a strong gradient between the moist boundary layer up to 700 m and the dry air atop. In the free atmosphere, above a height level of 2 km, there is less dry air. However, in comparison with the other "Golden Days", the near-surface humidity of 5 g/kg is low. In the course of the day, evaporated water-vapor from the surface is transported vertically upward by turbulent mixing and dry air from above the CBL is entrained. The mixing provides a height-constant humidity profile in the CBL. Since the entrainment is prevailing over the water-vapor input at the surface, the CBL is drying out slowly. The specific humidity thus decreases from 5 g/kg to 3.7 g/kg. Due to the growing of the boundary layer and the entrainment of less dry air from above 2 km, the humidity minimum is continuously decreasing from 0.5 g/kg to 2.2 g/kg. It is noteworthy that the water-vapor input by the latent surface heat flux is able to

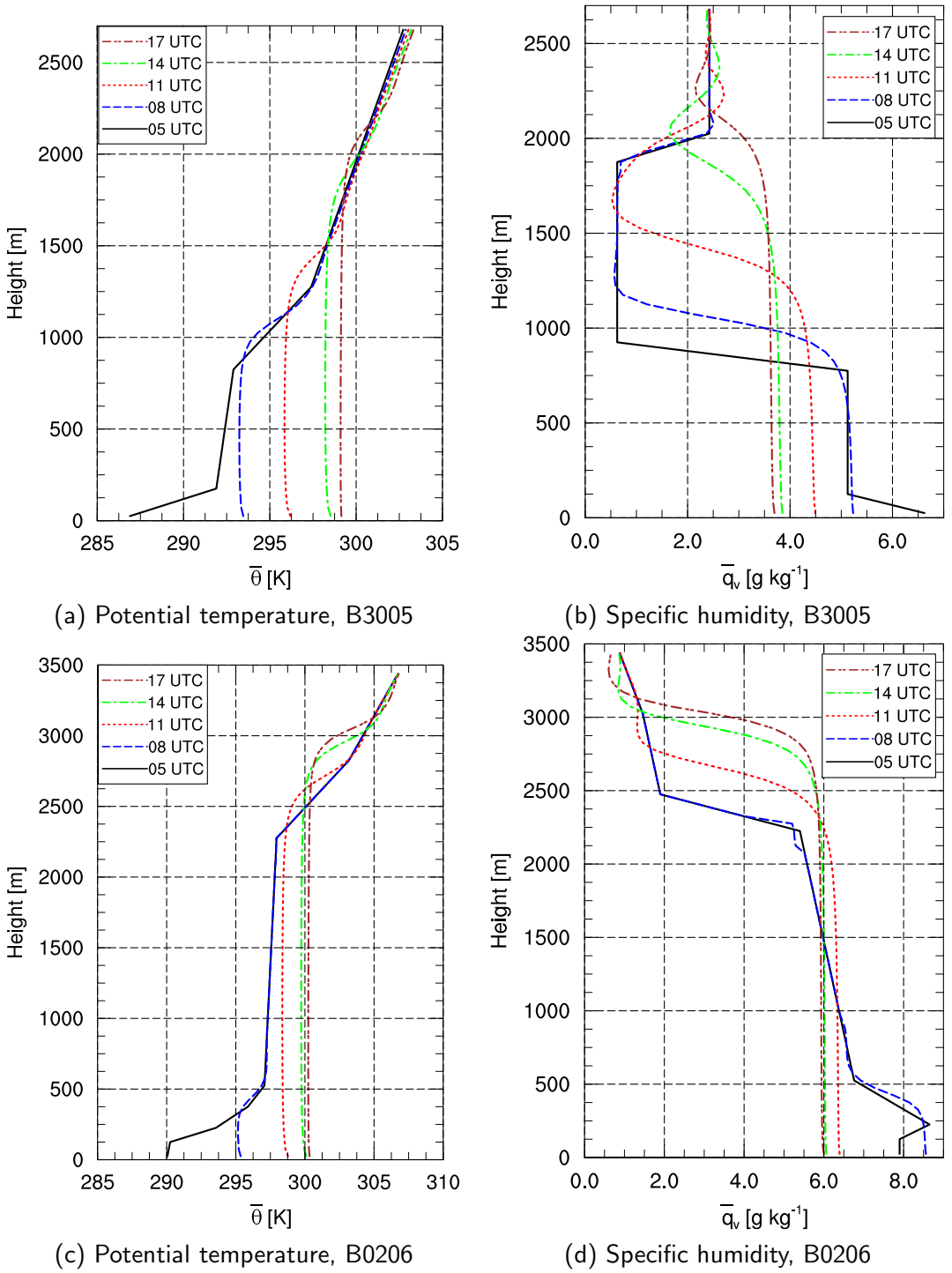

(a) Potential temperature, B3005

(b) Specific humidity, B3005

(c) Potential temperature, B0206

(d) Specific humidity, B0206

Figure 4.7: Vertical profiles of potential temperature (left) and specific humidity (right) from the LITFASS simulations, time-averaged over 900 s (part I).

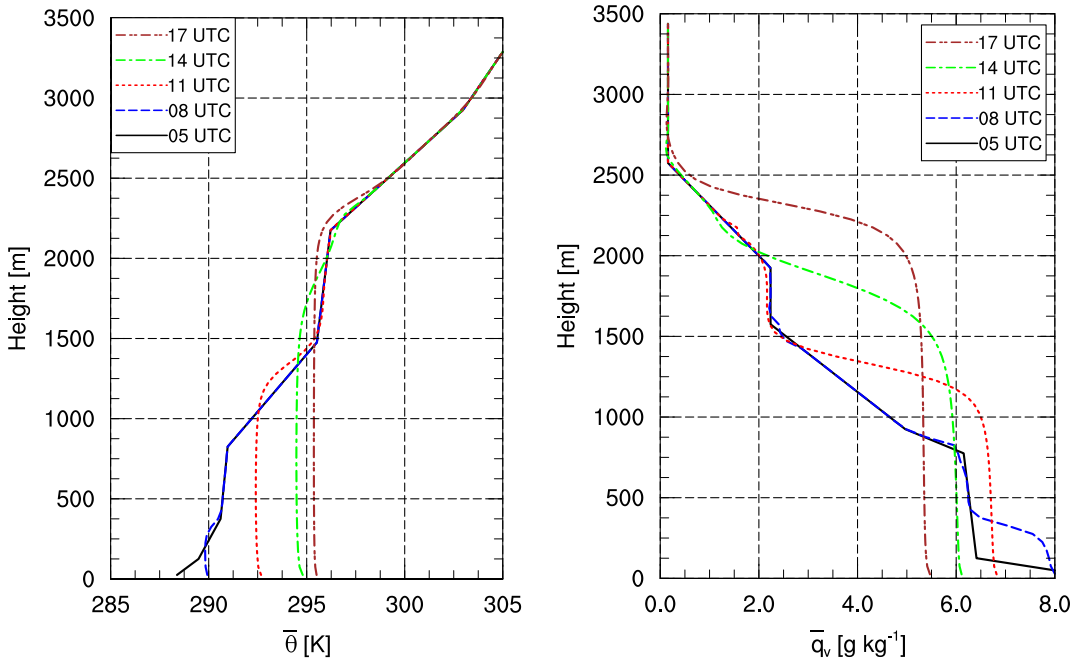

(e) Potential temperature, B1306

(f) Specific humidity, B1306

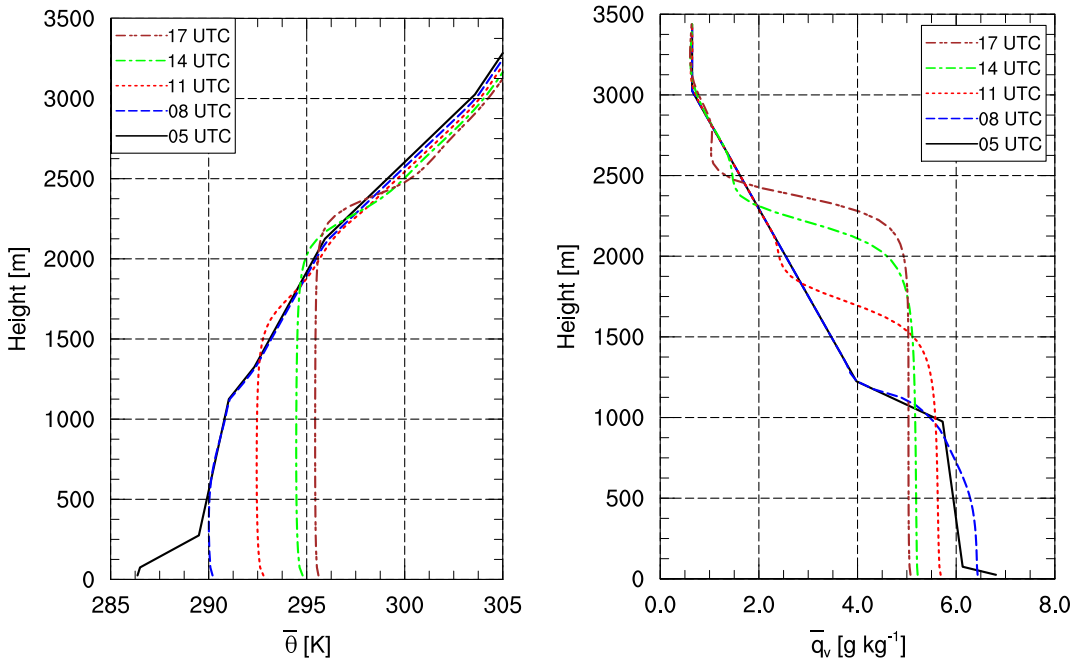

(g) Potential temperature, B1706

(h) Specific humidity, B1706

Figure 4.7: Vertical profiles of potential temperature (left) and specific humidity (right) from the LITFASS simulations, time-averaged over 900 s (part II).

increase the humidity of the mixing layer within the first three hours of simulation time. The mixing layer in case B1306 does not even start to dry out before 11 UTC.

A similar near-surface inversion can be found in case B0206, but the enormous residual layer atop the inversion is leading to the boundary layer depth jump mentioned in section 4.2.1 and to a smaller increase of the mixing layer temperature (~ 2.5 K), because more air mass must be heated up. The humidity decreases in the lower 400 m by 2 g/kg, while in the upper part no significant change occurs. In comparison, the gradient from moist air in the CBL and dry air in the free atmosphere is significantly higher than in case B3005.

Due to the presence of clouds in the morning hours on 06/13/03 (see Tab. 3.2), the LES initial profiles for case B1306 have been fitted to the radiosonde profile of 8 UTC (not shown). B1306 shows a weak near-surface inversion. Furthermore, two higher inversions are of relevance for the boundary layer development, as was already discussed in section 4.2.1. The mixing layer is heating up by 5 K during the course of the day and the humidity is decreasing by 1 g/kg. The free atmosphere is very dry (0.2 g/kg), thus a high gradient of $\Delta\overline{q} \approx 5$ g/kg persists between the mixing layer and free atmosphere.

Case B1706 exhibits a nocturnal inversion of 4 K and an increase of the mixing layer temperature of 5 K. The humidity is decreasing by about 1.5 g/kg.

Fig. 4.8 shows vertical profiles of the turbulent heat fluxes at 13 UTC for the LITFASS simulation and their HCRs. Both, sensible and latent heat flux display classical profiles (see e.g. Stull, 1988; Wyngaard and Coté, 1974a; Deardorff, 1974), that do not require further description. The sensible heat flux exhibits a higher entrainment flux $\overline{w'\theta'}_{min}$ in the HCRs of up to 20 W/m^2 (BH3005) compared to the LITFASS simulations. Apart from that, no differences between the heterogeneous and the homogeneous runs occur. The latent heat flux maxima and entrainment minima (moist air) of the LITFASS simulations show deviations from the HCRs of up to 30 W/m^2. While the cases B3005, B1306 and B1706 show a slightly lower heat flux in comparison to the HCRs, B0206 indicates an increase in the lower and a decrease in the upper boundary layer. Thus, a general statement whether or not the heterogeneous land surface implies an increased or decreased latent heat flux cannot be made. In sections 4.2.4 and 4.2.5 this issue will be further investigated.

The findings in this section are generally in agreement with the former study of Uhlenbrock (2006). However, the different border areas, and thus the horizontal averaged values, differ due to the non-homogeneous distribution of land use classes in the additional border areas, resulting in a modified total input of heat and moisture into the boundary layer. Small deviations from quantitative results that appear to arise from the modified model setup will therefore not be reported further.

4.2.3 Mesoscale circulations during the "Golden Days"

In the course of the LITFASS simulations, heterogeneity induced (thermal) secondary circulations occured, which form the main component for all further investigations in the present study. Since these circulations are on the mesoscale, they will hereafter be referred to as secondary circulations or, synonymically, mesoscale circulations. This section investigates the spatial structure and temporal evolution of SCs during the "Golden Days" simulations.

It was found that the heterogeneity induced vertical velocity $\widetilde{w'}$ (see section 3.3) is an appropriate indicator, since SCs are characterized by warm updrafts and cold downdrafts. Fig. 4.9 shows isosurfaces of $\widetilde{w'}$ at 12 UTC for the four LITFASS simulations. The red surface represents an isovalue of $\widetilde{w'} = 0.4$ m/s and the blue surface an isovalue of $\widetilde{w'} = -0.4$ m/s.

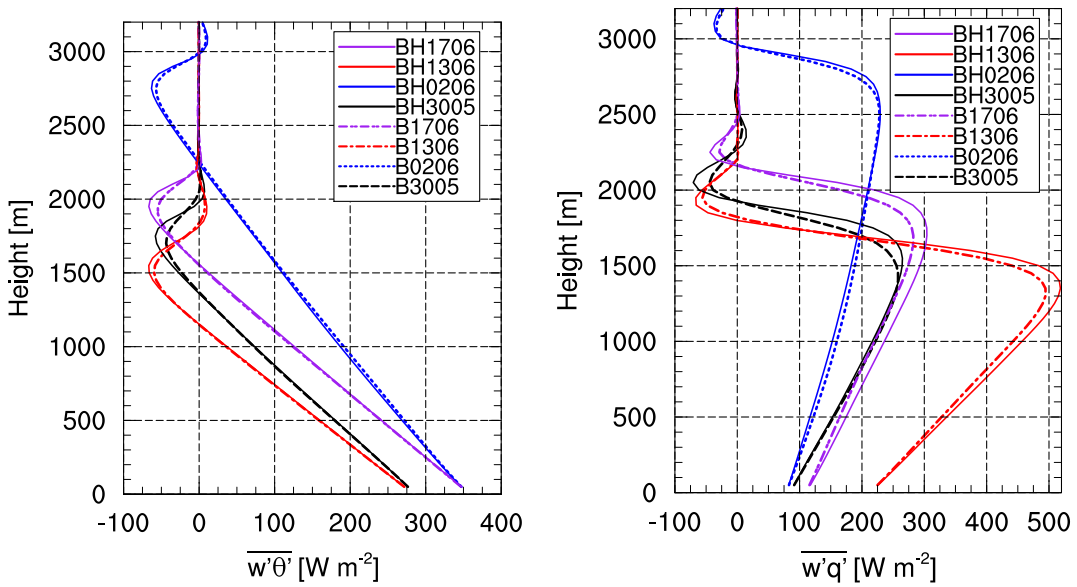

(a) Sensible heat flux (b) Latent heat flux

Figure 4.8: Vertical profiles of horizontal averaged sensible and latent turbulent heat fluxes of the LITFASS-Simulation (dashed lines) and the HCRs (solid lines). Plotted are profiles at 13 UTC, time-averaged over 900 s.

For case B3005, the shown structures can be considered as representative for the time span of $10-16$ UTC, while the other days display a higher variability in time, owing to the enhanced effect of advection and wind shear. The observed structures in Fig. 4.9 (a) are comparable to the structures shown by Uhlenbrock (2006). The other three cases show significant differences compared to Uhlenbrock (2006), which are most likely connected to the additional boundary area and supporting the results of section 4.1, that a border area of 10 km is not sufficient for background winds higher than 2 m/s. Most of the SC structures in case B3005 are associated with the underlying heterogeneity. Especially the water areas are connected to downdrafts and forest patches with updrafts (cf. Fig. 3.1), because on the one hand, the high heat capacity of water yields to no significant heat flux during the course of day, while on the other hand, forest patches exhibit high heat fluxes (see. Fig. 4.4). This contrast is leading to strong SCs, which allow to identify the surface heterogeneity. The light background wind from the east only has a small effect and allows a more or less free development of SCs. There is a tendency of updrafts to merge into elongated chains, like it is visible, for instance, running from the east of Lake Scharmützel in the north ($x = 17-21$ km, $y = 22-32$ km, Fig. 3.1) to the large forest patch in the west of the LFA. Furthermore, it is observable that the forest-water discontinuities are leading to strong SCs, whereas the SCs over the agricultural dominated area are weaker and the influence of agricultural land use heterogeneity can be regarded as small. This is also supported by the fact, that these agricultural heterogeneities are usually of a size smaller than the boundary layer height and thus do not effect the boundary layer structure (Shen and Leclerc, 1995).

Overall, the SC structures exhibit typical values of about 15 % of the convective velocity scale w_* and hence are not dominant in the boundary layer. They are rather superimposed on small-scale turbulent motions.

The other three cases are influenced by the background wind to a greater extent in such a way, that conclusions on the surface heterogeneity cannot be drawn prior to further investigation.

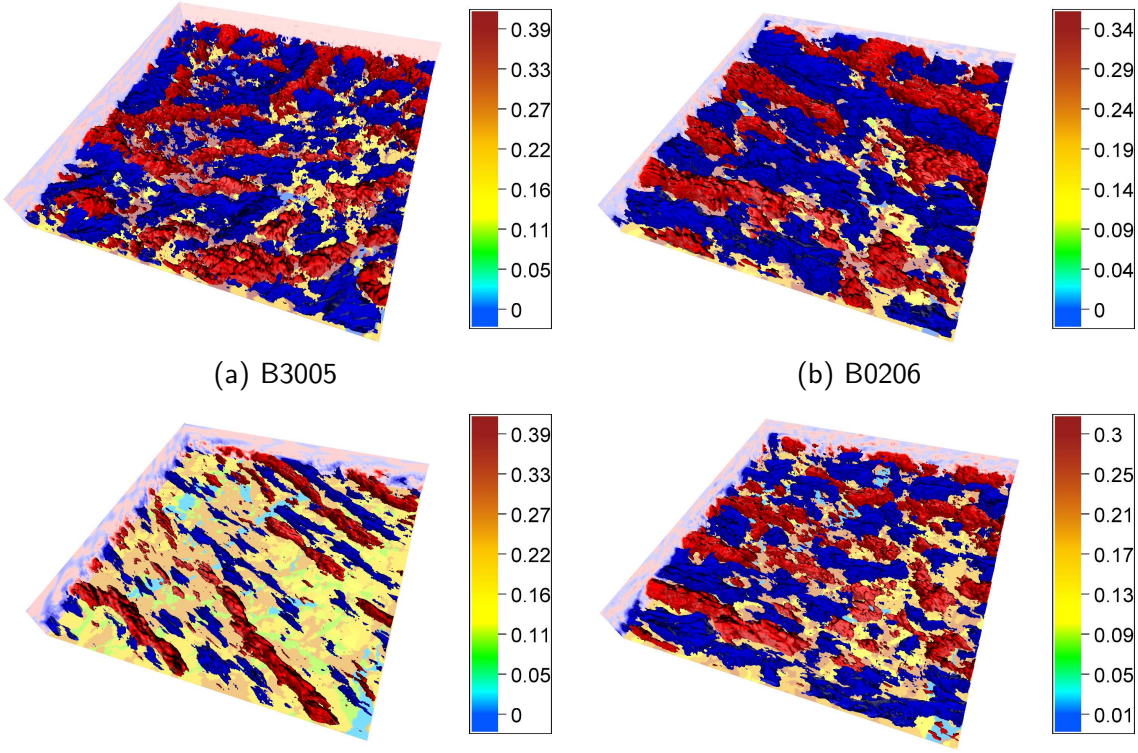

(a) B3005 (b) B0206

(c) B1306 (d) B1706

Figure 4.9: Structure of secondary circulations at 12 UTC during the "Golden Days", time-averaged over 900 s. The figure shows isosurfaces of the heterogeneity induced vertical velocity $\widetilde{w'}$. The red isosurface refers to $\widetilde{w'} = 0.4$ m/s (updrafts), the blue one to $\widetilde{w'} = -0.4$ m/s (downdrafts). The bottom surface displays the sensible surface heat flux according to the legend. Please note that the LFA is shown with an additional border area of 2.5 km at each side.

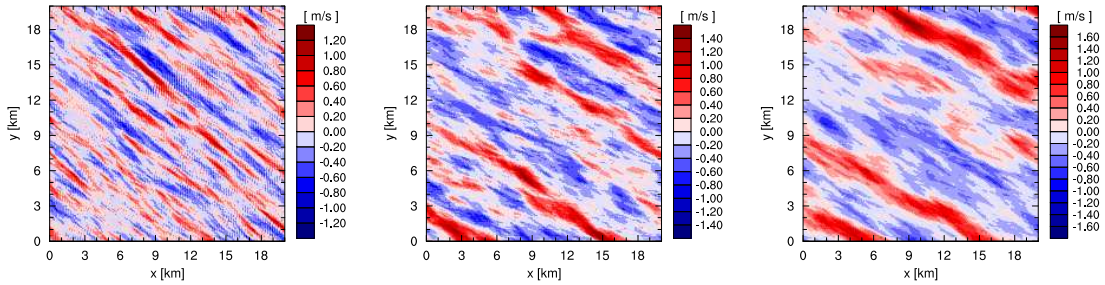

(a) 9 UTC (b) 12 UTC (c) 15 UTC

Figure 4.10: Horizontal cross-sections of the vertical velocity $\widetilde{w}'$ at $z = 0.5\ z_i$ at 9 UTC (a), 12 UTC (b) and 15 UTC (c) for case B1306, time-averaged over 900 s.

Section 4.3 will show that correlations between the heterogeneity and the SC also persist for cases with background wind of $4-6$ m/s. The structures in three cases are oriented to the mean wind direction, leading to more complex shapes. Cases B0206 and B1706 show roll-like structures, but the temporal evolution proves, that these structures are relatively short and advected by the mean wind (not shown). Nevertheless, updrafts and downdrafts evolve statistically over the same areas (disregarding the diurnal evolution). A comparison of B0206 and B1706 yields to the finding that many structures occur at the same locations (see SC bands in the southwest and the north in Fig. 4.9 (b), (d)) in both simulations. One can conclude that in consideration of background wind speed and direction, some structures appear to be generally located over certain areas. However, a forecast based on the results above is not feasible.

Case B1306 shows distinct development of long-ranged rolls all day long, oriented to the mean wind (Fig. 4.9 (c)). The rolls appear to be more slender than the structures in the other cases, caused by the visualization of the isosurfaces of $\widetilde{w}' = \pm 0.4$ m/s, while the SC strength is significantly decreased.

The temporal evolution of the SC is in general characterized by roll convection in the early morning hours, when the surface heterogeneity is still unincisive, and broadening of the SC structure during the course of day (see Fig. 4.10 (a)). The occuring rolls in the morning hours are oriented to the mean wind and are present within the entire LFA. Couvreaux et al. (2005) found rolls in their LES after 2 h of simulation time (morning hours) as well and stated the consistency with the moderate value of stability parameter $-z_i/L \approx 25$ (L is the Monin-Obkuhov length) proposed by Deardorff (1972). Etling and Brown (1993) reported that observations of thermal convections with roll-vortices might be found for $-z_i/L \approx 5$ to 25. In Couvreaux et al. (2005) as well as in the present study, the stability parameter was found to be in this range (not listed). Avissar and Schmidt (1998) also stated in their study of one-dimensional heterogeneities, that rolls can develop under conditions with a small heat flux amplitude, which is the case in the morning hours. Later on, when more incoming radiation is enforcing the heterogeneity, $-z_i/L$ increases and free convection as well as the superimposed SC replace those rolls. In the last hour of simulation time, the surface forcing is significantly weakened, thus the SCs start to vanish as well.

As already mentioned, case B3005 shows more or less constant SCs during the course of day, which are, however, also broadening with increasing z_i. The broadening holds for all cases, and is exemplarily shown for case B1306 in Fig. 4.10. Due to the fact that heterogeneities smaller than z_i do not influence the boundary layer structure, the surface heterogeneity is changing with increasing boundary layer height in such way that larger heterogeneities become more important with time. This is resulting in larger (broader) SC structures.

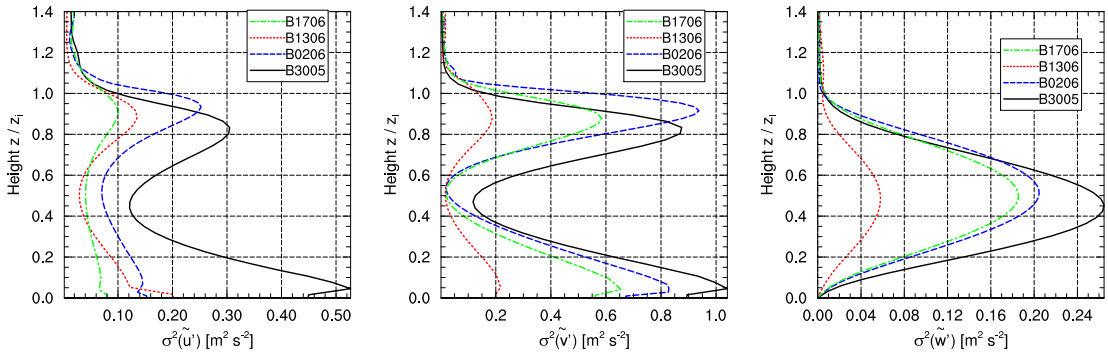

(a)$\sigma(\widetilde{u'})$ (b) $\sigma(\widetilde{v'})$ (c) $\sigma(\widetilde{w'})$

Figure 4.11: Variance profiles of the dynamic heterogeneity induced variables $\widetilde{u'}$, $\widetilde{v'}$ and $\widetilde{w'}$ at 12 UTC, averaged over 1 h.

The variance profiles of the dynamic variables $\widetilde{u'}$, $\widetilde{v'}$ and $\widetilde{w'}$ are shown in Fig. 4.11 and can be regarded as a measurement for the circulation strength. The variance of the vertical velocity $\sigma(\widetilde{w'})$ displays a gaussian distribution, which peak values at $0.45-0.5\ z_i$. The peak magnitude is decreasing from case B3005 ($0.26\ \mathrm{m^2/s^2}$) to B1306 ($0.06\ \mathrm{m^2/s^2}$), showing that the circulation strength is strongly dependent on the background wind. It is apparent that the height level of the maximum is slighty shifted downwards in the weak wind case.

The profiles of $\sigma(\widetilde{u'})$ and $\sigma(\widetilde{v'})$ both exhibit double peaks, a lower one at $0.05\ z_i$ and an upper one at $0.8-0.95\ z_i$. These peaks are connected to horizontal compensational branches of the SCs, which typically occur near the top and the bottom of the boundary layer, showing that the SCs bestride the entire boundary layer. This behavior was also shown by Prabha et al. (2007). Owing to the prescribed wind direction, the SCs are not perfectly aligned to any of the grid axes and thus the variances of $\widetilde{u'}$ and $\widetilde{v'}$ cannot show a perfect dependency on the background wind. However, it is clearly observable that the horizontal velocity variances resemble the relation of the SC strength and background wind. It is noticeable that $\sigma(\widetilde{v'})$ shows values approximately twice as high as $\sigma(\widetilde{u'})$, which indicates, that north-south compensational flows are dominating in the simulations. This is obvious, since the SCs are in all cases mainly oriented in west-east direction and the horizontal branches of the SCs thus are oriented in north-south direction. Furthermore, B3005 displays downward shifted peaks, which is in accordance with $\sigma(\widetilde{w'})$.

Global maximum and minimum values as well as the maximum standard deviations and the respective height levels are listed in Tab. 4.4. Compared to Uhlenbrock (2006), similar maximum und minimum global values of $\widetilde{w'}$ for cases B3005 and B1306 are obtained. The other two cases show slightly higher absolute values (cf. Uhlenbrock, 2006, Tab. 5.4). The scalar quantities are generally found to be larger than respective absolute values of Uhlenbrock (2006). The highest standard deviations are located near the top of the boundary layer ($0.98\ z_i$ in case B3005, above z_i otherwise). This will be discussed in detail in section 4.2.4. The differences might be explainable by the fact that Uhlenbrock (2006) did not take into account values above the top of the boundary layer. However, the results of this section show overall higher absolute values and thus suggest slightly stronger SCs. The relation $|\widetilde{w'}_{max}| > |\widetilde{w'}_{min}|$ holds for all cases and proves that the updrafts are more intense than the downdrafts, as expected. Usually, small-area updrafts transport warm air to the top of the boundary layer. The compensational downdrafts are of large-scale and due to continuity reasons significantly weaker. For the heterogeneity induced temperature, the relation $|\widetilde{\theta'}_{max}| < |\widetilde{\theta'}_{min}|$ is observable and can be related to the updrafts and the inversion strength as will also be discussed in detail in section 4.2.4.

Case	$\widetilde{\Phi'}$	Global min.	Global max.	$\sigma_{\widetilde{\Phi'}_{max}}$	$z(\sigma_{\widetilde{\Phi'})_{max}}$ $[z/z_i]$
B3005	$\widetilde{w'}$ [m/s]	−1.29	2.89	0.51	0.45
	$\widetilde{\theta'}$ [K]	−1.64	0.97	0.45	0.98
	$\widetilde{q'}$ [g/kg]	−1.60	3.04	0.89	0.98
B0206	$\widetilde{w'}$ [m/s]	−1.20	1.86	0.45	0.51
	$\widetilde{\theta'}$ [K]	−1.82	1.24	0.57	1.07
	$\widetilde{q'}$ [g/kg]	−2.43	2.47	0.90	1.05
B1306	$\widetilde{w'}$ [m/s]	−0.86	1.03	0.24	0.49
	$\widetilde{\theta'}$ [K]	−0.96	0.87	0.26	1.05
	$\widetilde{q'}$ [g/kg]	−1.55	2.00	0.58	1.02
B1706	$\widetilde{w'}$ [m/s]	−1.20	2.05	0.44	0.48
	$\widetilde{\theta'}$ [K]	−1.78	0.92	0.36	1.04
	$\widetilde{q'}$ [g/kg]	−1.81	1.92	0.64	1.01

Table 4.4: Global maximum and minimum values as well as maximum standard deviations of heterogeneity induced quantities at 13 UTC, time-averaged over 1 h

In summary and by means of Fig. 4.11 and Tab. 4.4, weak wind case B3005 features the strongest SC, followed by the cases B0206 and B1706, which exhibit similar characteristic as will be shown during the course of this study. The case with the highest background wind B1306 shows the weakest SC, which is in agreement with Uhlenbrock (2006), but in disagreement with Prabha et al. (2007) who suggested, that higher background winds and the formation of rolls strenghtens the SCs. The dependency on the background wind was stated in several studies as mentioned in section 1.3 and also holds for realistic surface heterogeneities.

4.2.4 Structure of other heterogeneity induced quantities

Structure of scalar quantities

The previous section illustrated the structure of secondary circulations during the "Golden Days", but the behavior and development of the scalar quantities $\widetilde{\theta'}$ and $\widetilde{q'}$ have not been discussed yet. Since these structure are highly related to the circulation structure and $\widetilde{w'}$, this section will also examine $\widetilde{w'}$, but always in connection and with emphasis on the scalar quantities. Unless otherwise noted, the data used in this section is time-averaged over 1 h from $12-13$ UTC.

Spatial characteristics A first look at horizontal cross-sections at 0.5 z_i shows, that the scalar quantities in general behave differently from the circulation and above all its variance is dominated by different (larger) length scales (Figs. 4.12 and 4.13). $\widetilde{\theta'}$ structures of weak wind case B3005 can be easily linked to the underlying surface heterogeneity. Areas of high surface heat flux, especially forest patches in the north and the west of the LFA, reflect in a high positive value, while the rest of the area shows accordingly negative values. On this visual basis it is not possible to relate the pattern to the SC. For the other cases, this surface signal is vanished due to enhanced advection. For Case B1306, the wind speed becomes even more important, resulting in an orientation of the structures in bands along the mean wind direction (see Fig. 4.12 (c)). The latter finding holds for $\widetilde{q'}$, too (Fig. 4.13 (c)). Apart from that, the

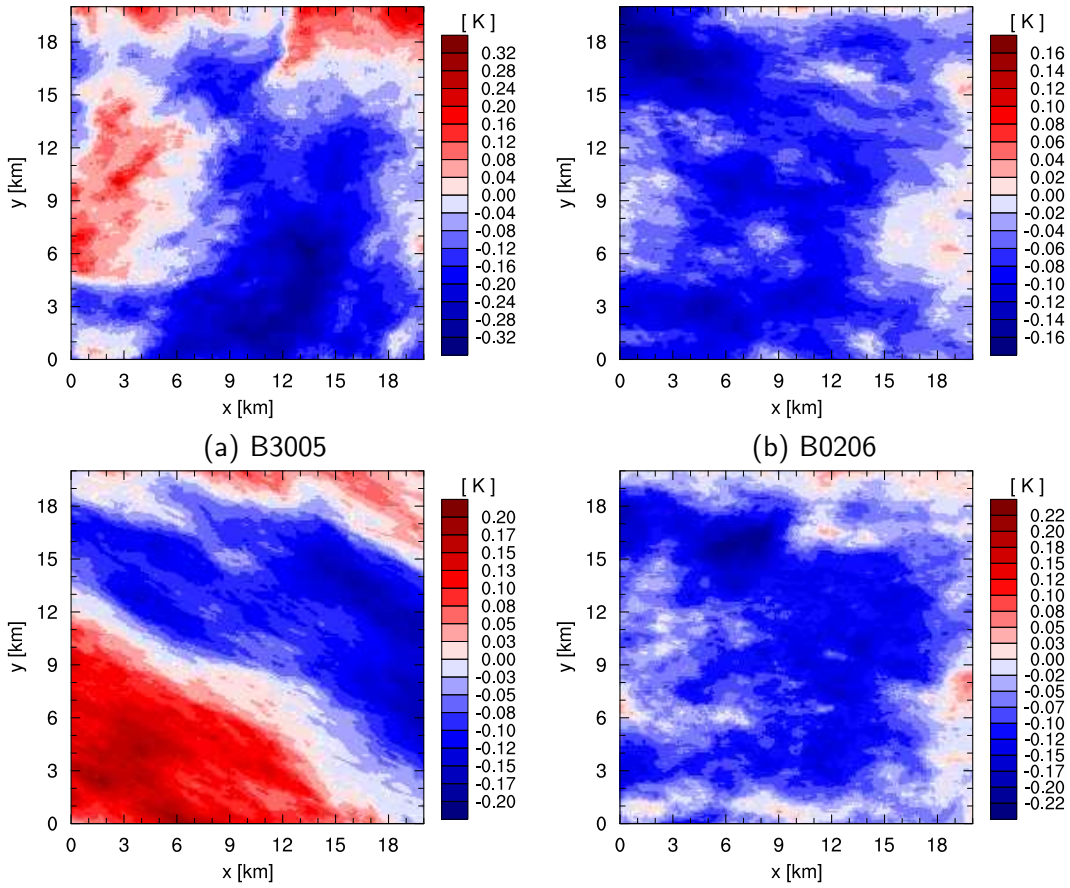

Figure 4.12: xy-cross-sections of the heterogeneity induced temperature $\widetilde{\theta}'$ at 13 UTC at 0.5 z_i, averaged over 15 min.

humidity structures in all cases do not show any connection with the surface properties or the SC and are also significantly dominated by larger scales of at least the size of the LFA.

In contrary to the vertical velocity $\widetilde{w}'$, the variance profiles of $\widetilde{\theta}'$ and $\widetilde{q}'$ exhibit high maxima at the top of the boundary layer (Fig. 4.14, cf. Fig 4.11 (c)). These maxima are caused by folding of the inversion layer due to rising thermals. This process is discussed in detail in section 4.2.4. The scheme in Fig. 4.15 illustrates that the height of the interface between boundary layer and inversion layer is varying horizontally owing to rising updrafts of relatively warm air. The ambient air in the inversion layer is much warmer and drier than the air in the boundary layer and also warmer than the thermals penetrating into the inversion layer. Since the boundary layer height is treated as horizontally constant in the analysis (represented as dashed line in Fig. 4.15), this is leading to high spatial variances of the scalar quantities. The absolute peak values are depending on the wind speed and inversion strength. A strong inversion, characterized by a high temperature jump, will lead to a higher variance than a weak inversion layer. Higher background winds cause a decreased SC strength and less intense updrafts that do not rise deep into the inversion layer. The peak of case B0206 is larger than that of B3005 for both scalars. This is in contrast to Uhlenbrock (2006), who found the highest variances on B3005. This difference must be ascribed to the additional border area of 8 km in the present study. Near the surface, the temperature variance shows a lower secondary maximum which is generated by the surface heat flux distribution of the heterogeneity. The humidity variance does not show this

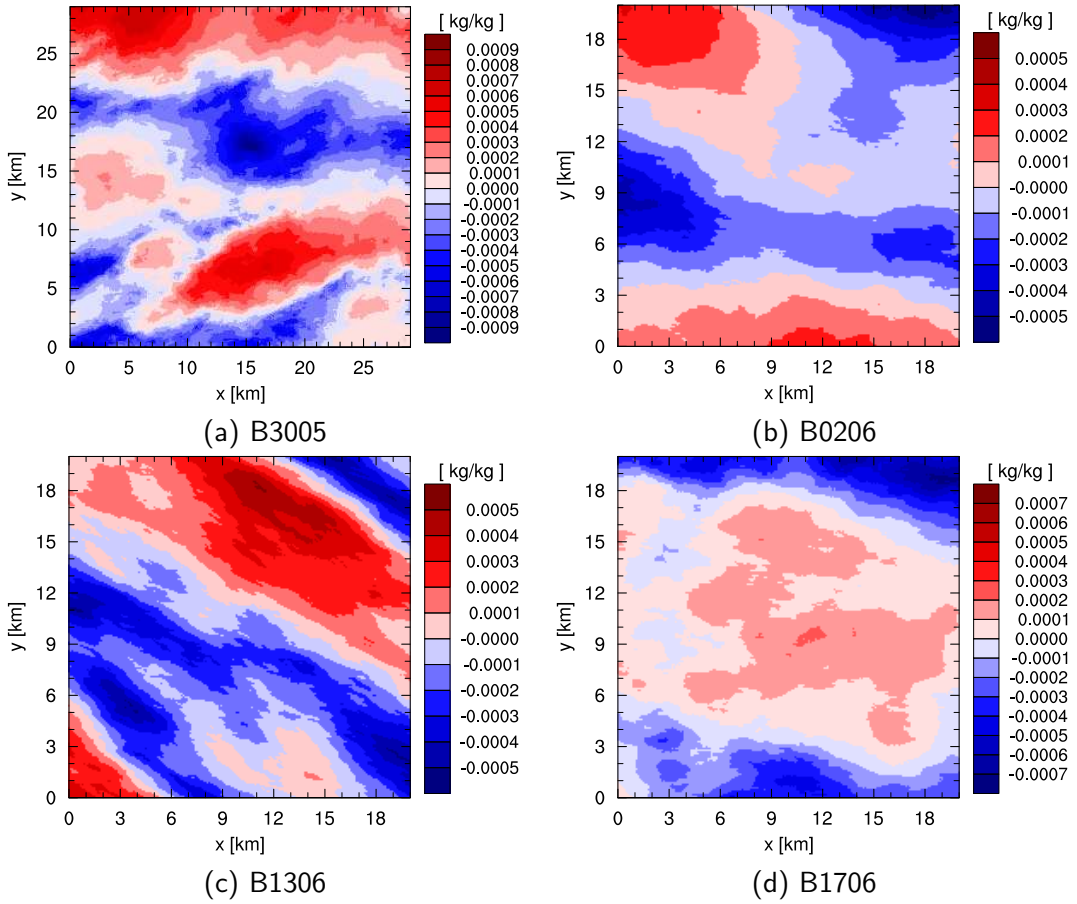

Figure 4.13: xy-cross-sections of the heterogeneity induced humidity $\widetilde{q'}$ at 13 UTC at 0.5 z_i, averaged over 15 min.

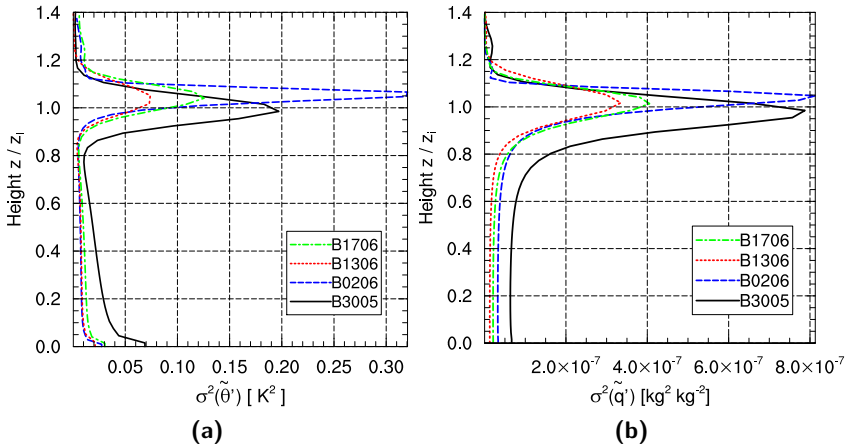

Figure 4.14: Variance profiles of the heterogeneity induced scalar quantities $\widetilde{\theta}'$ (a) and $\widetilde{q}'$ (b) at 13 UTC, averaged over 15 min.

secondary peak which proves that the latent surface heat flux distribution in the model domain is only of minor importance for the heterogeneity induced structures and small compared to the variance at the top of the boundary layer. Within the boundary layer, the temperature variance is slightly decreasing with height, while the humidity variance is constant with height. $\widetilde{\theta}'$ and $\widetilde{q}'$ show classical profiles and coincide with several studies (e.g. Stull, 1988, modeled from measurement data; Couvreaux et al., 2005, observations and LES; Courault et al., 2007, LES; Kang and Davis, 2008, LES; van Heerwaarden and Vilà-Guerau de Arellano 2008, LES). In the idealized study of Courault et al. (2007), a high humidity variance was found near the surface due to the explicit specification of the heterogeneities. Since the variance of $\widetilde{\theta}'$ is decreasing with height, it can be assumed that temperature structures are generated by surface properties and propagating into the boundary layer by SC, where they are broadening and blending with height.

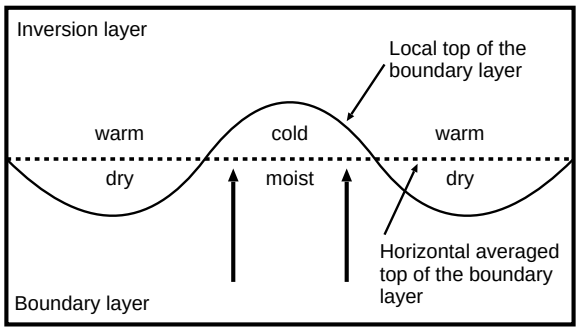

Figure 4.15: Schematic figure, showing the folding of the interface between boundary layer and inversion layer due to rising thermals.

For further studying the vertical structure and the relations betweeen scalar quantities, the 2D-correlation-coefficient, defined as

$$\rho_{\widetilde{\Phi}',\widetilde{\Psi}'} = \frac{\iint \widetilde{\Phi}'(x,y) \cdot \iint \widetilde{\Psi}'(x,y)\ dx\ dy}{\sqrt{\iint \left[\widetilde{\Phi}'(x,y)\right]^2\ dx\ dy}\sqrt{\iint \left[\widetilde{\Psi}'(x,y)\right]^2\ dx\ dy}} \quad , \tag{4.7}$$

was used to calculate the cross-correlations $\rho_{\widetilde{\theta}',\widetilde{q}'}$, $\rho_{\widetilde{w}',\widetilde{q}'}$ and $\rho_{\widetilde{\theta}',\widetilde{w}'}$ as well as $\rho_{\widetilde{\theta}',\widetilde{\theta}'_0}$ and $\rho_{\widetilde{q}',\widetilde{q}'_0}$

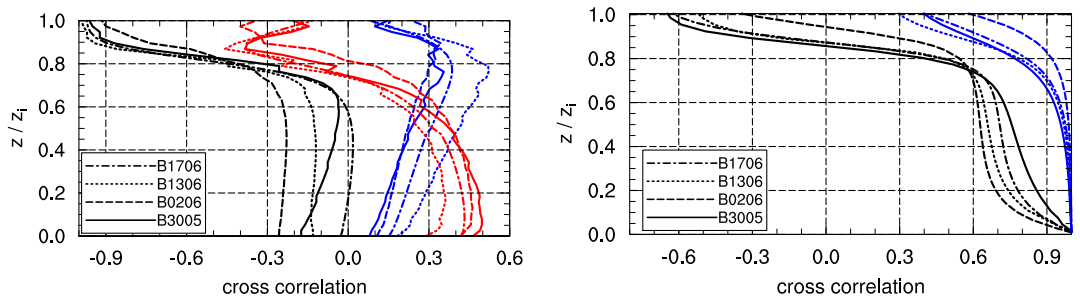

Figure 4.16: 2D cross-correlation profiles of heterogeneity induced quantities, averaged over 1 h. (a) shows $\rho_{\widetilde{\theta}',\widetilde{q}'}$ (black), $\rho_{\widetilde{w},\widetilde{q}'}$ (blue) and $\rho_{\widetilde{\theta}',\widetilde{w}'}$ (red), (b) shows the cross correlation to the near surface values $\rho_{\widetilde{\theta}',\widetilde{\theta}'_0}$ (black) and $\rho_{\widetilde{q}',\widetilde{q}'_0}$ (blue).

against height level (Fig. 4.16). Since the obtained curves for the different simulations differ only slightly, their general characteristics will be discussed only. $\rho_{\widetilde{\theta}',\widetilde{q}'}$ (black curves) reveals no significant correlation in the boundary layer. From $0.7z_i - 1.0z_i$, $\rho_{\widetilde{\theta}',\widetilde{q}'}$ decreases rapidly to nearly perfect anti-correlation. This is originated from the folding of the inversion layer, where warm and cold areas match dry and moist areas, respectively (see Fig. 4.15). $\rho_{\widetilde{w}',\widetilde{q}'}$ (blue curves) displays only small correlation near the surface, increasing with height up to $0.8z_i$ ($\rho_{\widetilde{w}',\widetilde{q}'} \leq 0.5$) and decreasing above. The medium correlation at $0.8z_i$ can again be ascribed to the folded interface between inversion and boundary layer. Moist air is therefore correlated to areas with positive $\widetilde{w}'$ and dry air to negative $\widetilde{w}'$. The decrease above is due to the fact, that the spatial variation and the strength of $\widetilde{w}'$ decreases rapidly near the top of the boundary layer (see also Fig. 4.11 (c)). The correlation of moist air and strong updrafts near the top of the boundary layer was also shown by van Heerwaarden and Vilà-Guerau de Arellano (2008) and seems to apply to heterogeneity induced mesoscale quantities, too. The temporal evolution of $\rho_{\widetilde{w}',\widetilde{q}'}$ leads to the finding, that the correlation is markably higher in the first hours of simulation and is decreasing in time towards the end of the simulation (not shown). De Roode et al. (2004) found a large anti-correlation between the mesoscale fluctuations of $\widetilde{\theta}'$ and $\widetilde{q}'$ over homogeneous heated surfaces by calculating the cospectral energy. This doesn't seem to hold for heterogeneity induced mesoscale fluctuations. The 2D cross-correlation $\rho_{\widetilde{\theta}',\widetilde{w}'}$ shows medium to high correlations up to $0.6z_i$ and a fast decrease above to negative values about -0.3. Thus, the large correlation in the lower part of the boundary layer can be linked to the circulation structure. Surface patches are heated and thermals rise usually above those patches. However, the evolving of updrafts is connected to local surface temperature gradients as well, but the definition of $\widetilde{\theta}'$ refers to the horizontal domain average. This decreases the correlation coefficient. Due to a smeared effect of the surface heterogeneity on the development of SC (shown in section 4.3.1), the correlation decreases with increasing background wind. The negative values above $0.8z_i$ are again caused by the folding of the inversion layer and can in addition be treated as resulting combination of $\rho_{\widetilde{\theta}',\widetilde{q}'}$ and $\rho_{\widetilde{w}',\widetilde{q}'}$.

The cross-correlations between $\widetilde{\theta}'$, $\widetilde{q}'$ and their respective surface values $\widetilde{\theta}'_0$, $\widetilde{q}'_0$ proves that the vertical structure of the scalar quantities is relatively constant. Humidity structures are highly correlated to the surface values up to $0.8z_i$ (Fig. 4.16 (b)). The decrease in the upper boundary layer displays the transition to the interfacial layer where the humidity variances increase (see Fig. 4.14). $\rho_{\widetilde{\theta}',\widetilde{\theta}'_0}$ decreases slightly with height but holds values ≤ 0.6 up to a height level of $0.7z_i$. It clarifies that the temperature structures change to a greater extent with height than the humidity structures, but that there is still a high correlation to the surface characteristics.

Above $0.7z_i$ the correlation is decreasing fast to a final value around -0.6, showing the anti-correlation of temperature variations in the boundary layer with those near the inversion layer (warm updrafts are relatively cool compared to the ambient air of the inversion layer).

As already mentioned, the most interesting characteristic is that humidity structures seem to be constant in the boundary layer, while the temperature structures change significantly with height. Furthermore it is still unclear how these structures develop. The finding that the scalar fluctuations are dominated by large scales was also observed by Jonker et al. (1999), who studied mesoscale fluctuations in a CBL with LES by comparing energy spectra with emphasis on passive scalars. They found a dependency of the dominant length scale of a passive scalar S on the ratio

$$r = \frac{\overline{w'S'_e}}{\overline{w'S'_0}} \quad , \tag{4.8}$$

where $\overline{w'S'_e}$ is the entrainment flux and $\overline{w'S'_0}$ is the surface flux. They supposed that the length scales of S are dominated by small scales ($\sim z_i$) if $r \approx -0.5$, while for most other ratios, the scalar fluctuations are dominated by the largest resolved length scales. De Roode et al. (2004) stated that the findings of Jonker et al. (1999) are also applicable to active scalars, such as temperature and humidity and that mesoscale fluctuations are negligible for $r \approx -0.25$. van Dop et al. (2005) tried to prove the findings of Jonker et al. (1999) and De Roode et al. (2004) in laboratory water tank experiments and found some evidence of the distinct different behavior (particularly length scales) between the dynamic and passive variables. The present study uses some of the techniques of Jonker et al. (1999) and De Roode et al. (2004) to investigate the mesoscale fluctuations $\widetilde{\theta}'$ and $\widetilde{q}'$. It must be stated *a priori* that the simulation data does not show any dependency on the ratio r and that $\overline{w'\theta'_0}$ exhibits ratios from -0.15 to -0.26, which does not lead to a significant shift to smaller length scales. Couvreaux et al. (2005) investigated the length scales of the humidity variability by observations and LES and concluded from their results that the dominant length scales are governed by dry drowndraughts from the inversion layer.

A two-dimensional FFT is used to calculate discrete variance (energy) spectra from horizontal planes of the heterogeneity induced quantities. The transformation provides a 2D-matrix of the spectral density $S_{\widetilde{\Phi}'}(k_x, k_y)$, where k_x and k_y are the wave numbers. Since the FFT assumes periodic fields, the full model domain was used for the calculation. Following the methods of Schröter (2003) and De Roode et al. (2004), a one-dimensional representation of the variance spectrum $S_{\widetilde{\Phi}'}(k)$ can be calculated by summing up equal wave numbers $k = \sqrt{k_x^2 + k_y^2}$ ($k \leq Ny$, where Ny is Nyquist frequency). Fig. 4.17 shows spectra in the middle of the boundary layer for the heterogeneity induced quantities $\widetilde{w}'$, $\widetilde{\theta}'$ and $\widetilde{q}'$ against wave numbers. The curves have been normalized in such a way that the area under the curves equals the dimensionless variance of the quantity. The spectral peaks' wave numbers of $S_{\widetilde{w}'}$ are usually in the range of $1.5 \cdot 10^{-4} - 3.0 \cdot 10^{-4} \mathrm{m}^{-1}$, which corresponds to wave lengths of $3.3 - 6.7$ km, which is in good agreement with the visual analysis of the SC in section 4.2.3 (B0206 also shows a markable secondary peak at $4 \cdot 10^{-5}$ m^{-1}). All spectra show no variance contribution of wave numbers higher than $6.0 \cdot 10^{-4}$, showing that the ensemble-averaging filtered small-scale turbulence signals successfully. $S_{\widetilde{\theta}'}$ and $S_{\widetilde{q}'}$ show a clear shift of the peaks to smaller wave numbers, which implies the occurance of larger structures. $S_{\widetilde{\theta}'}$ shows maximum values at the smallest resolved wave numbers, which are depending on the model domain size. No delimited peak value can be found, leading to the finding that the main part of the variance of $\widetilde{\theta}'$ is characterized by structures of the size of the model domain. This follows from the assumption of periodicity of the FFT, which yields some problems, since structures that occur once in the data fields are treated as waves with a wave length of the model domain. On the other

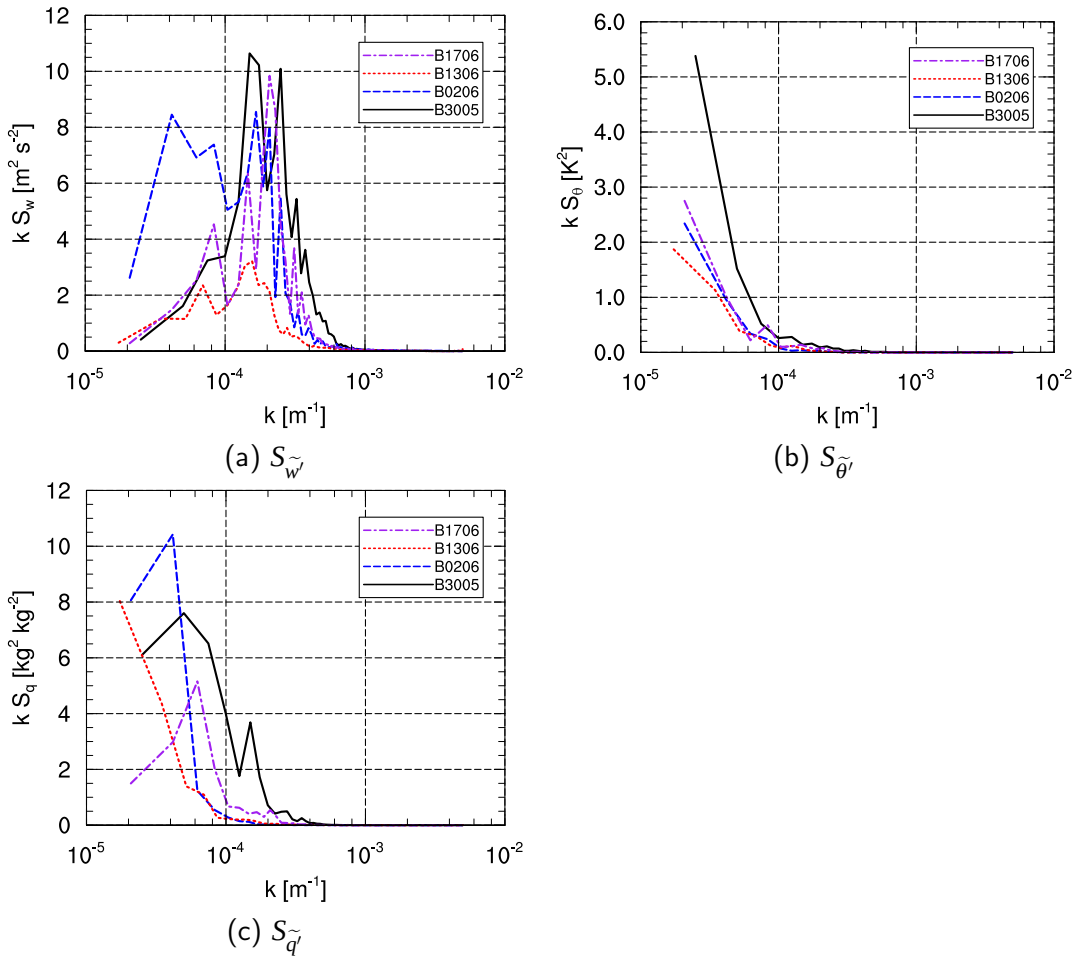

Figure 4.17: Variance spectra of the heterogeneity induced quantities in log-linear presentation at $0.5 \cdot z_i$, 13 UTC, averaged over 1 h. The area under the curves is normalized such that it equals the dimensionless variance of the variable.

hand, $S_{\widetilde{q}'}$ shows a distinct peak at low wave numbers for three cases. The gained shapes are in accordance with the spectra showed by Kang and Davis (2008) and Kang (2009), who used LES and mesoscale surface heterogeneities, as well as with the spectra from measurements of the BOREAS and AMTEX studies, presented by Lenschow and Sun (2007).

Jonker et al. (1999) already stated that the peak values are vulnerable to errors, thus several methods of calculating a length scale Λ are proposed in literature. The method used by Jonker et al. (1999), based on a weighted integral of the spectrum was refined by Pino et al. (2006b) as follows:

$$\Lambda_{\widetilde{\Psi}'}^{-a} = \frac{\int S_{\widetilde{\Psi}'}(k)\ k^a\ dk}{\int S_{\widetilde{\Psi}'}(k)\ dk} \quad , a \neq 0 \quad , \tag{4.9}$$

where a is a user-defined weighting parameter. De Roode et al. (2004) suggested the usage of the ogive, defined by Oncley et al. (1996) as

$$O_{\widetilde{\Psi}'} = \int_{k_c}^{k_{Ny}} S_{\widetilde{\Psi}'}(k)\ dk \quad . \tag{4.10}$$

The ogive gives the integrated contribution to the variance of all wave numbers above a critical wave number k_c. De Roode et al. (2004) defined a critical wave number k_c from the ogive

by calculating the wave number where the ogive equals $2/3$ of the total variance ($\Lambda = 1/k_c$). However, this method was found to be unstable for the data of the present study. Hence, Eq. 4.9 was adopted. In contrary to Pino et al. (2006b), who used $a = -1$ and argued that the choice of $a = 1$ by Jonker et al. (1999) put too much weight on small scales, the present study uses $a = 1$ in consideration of the filtering of small-scale contributions by the ensemble average. Eq. 4.9 reduces with $a = 1$ to

$$\Lambda_{\widetilde{\Psi'}} = \frac{\int S_{\widetilde{\Psi'}}(k)\ dk}{\int S_{\widetilde{\Psi'}}(k)\ k\ dk} \quad , \tag{4.11}$$

where $\Lambda_{\widetilde{\Psi'}}$ is the "dominant length scale" (Jonker et al., 1999).

Vertical profiles of dominant length scales The length scales $\Lambda_{\widetilde{w'}}$, $\Lambda_{\widetilde{\theta'}}$, $\Lambda_{\widetilde{q'}}$ are shown against height level in Fig. 4.18 (a). Both axes are normalized by the boundary layer height z_i. Near the surface, $\Lambda_{\widetilde{w'}}$ (black curves) scales with z_i. It is increasing with height to maximum values of about $3-4 \cdot z_i$, located just above the middle of the boundary layer. Though case B1306 shows a slightly different characteristic near the surface (slow increase with height), the four simulation cases show a generally similar behavior. The shapes are consistent with the finding of the observational study (homogeneous surface) of Kaimal et al. (1976) that the spectral peak value of the vertical velocity moves to higher wave lengths with height. De Roode et al. (2004) found a similar profile. In contrast to the present study, $\Lambda_{\widetilde{w'}}$ was generally found to scale with z_i. This is no contradiction to the found values of $3-4 \cdot z_i$, since only heterogeneity induced mesoscale quantities are investigated. Thus, generally larger length scales than in the homogeneous simulations of De Roode et al. (2004) are expected. $\Lambda_{\widetilde{\theta'}}$ (blue curves) displays explicit different behavior. At ground level $\Lambda_{\widetilde{\theta'}}$ scales with $4-8 \cdot z_i$. The length scale is increasing rapidly with height up to values between $13-17 \cdot z_i$, except for case B1306, which reaches a value of $24 z_i$ at a downward shifted maximum at height $0.4 z_i$, while for the other cases, the maximum is located further up at $0.7 z_i$. Atop the maximum, the length scale is again decreasing to values similar to ground level values. This decrease is found for humidity as well and can be ascribed to the processes at the inversion layer interface. The dominant humidity length scale $\Lambda_{\widetilde{q'}}$ (red curves) is also much larger than $\Lambda_{\widetilde{w'}}$. It shows, again except case B1306 that the length scale of the humidity structure is constant to a great extent within the boundary layer (values of about $8-12 \cdot z_i$) and supports the previous finding of a high cross-correlation $\rho_{\widetilde{q'},\widetilde{q'_0}}$ in the boundary layer (see Fig. 4.16 (b)). In contrary to other studies (e.g. De Roode et al., 2004; Couvreaux et al., 2005), $\Lambda_{\widetilde{q'}}$ appears to be smaller than $\Lambda_{\widetilde{\theta'}}$ in the middle of the boundary layer. De Roode et al. (2004) found a similar shape of the virtual potential temperature profile, which is comparable to $\Lambda_{\widetilde{\theta'}}$, with maximum values of about $3\ z_i$ and mentioned that the length scales of $\Lambda_{\widetilde{\theta'}}$ are similar to $\Lambda_{\widetilde{q'}}$ and fast-growing. Corresponding humidity length scales were found to be time-dependent (shape and magnitude) and varied between $4\ z_i$ to $6\ z_i$. However, the shape of $\Lambda_{\widetilde{q'}}$ in Fig. 4.18 differs from the results of De Roode et al. (2004).

The considerable deviation of the length scales of case B1306 raises the question of possible causes for this behavior which results in much higher values. The main characteristics of B1306 are the high background wind and the large domain size. The visual analysis showed that B1306 is the only case where scalar structures clearly oriented to the mean wind. This leads to a decrease in the variance contribution of smaller scale structures (see Fig. 4.12 (c) and Fig. 4.13 (c)), since smaller structures near the top or bottom of the boundary layer are affected by wind shear and broadened. Especially $\Lambda_{\widetilde{\theta'}}$ benefits from this effect. Another reason might be attributed to the model domain size, since this is the maximum length scale the FFT can provide. On the one hand, any structure occuring only once in the model domain is seen by the FFT as periodic with wave lengths equal to the domain size. A larger domain size can therefore

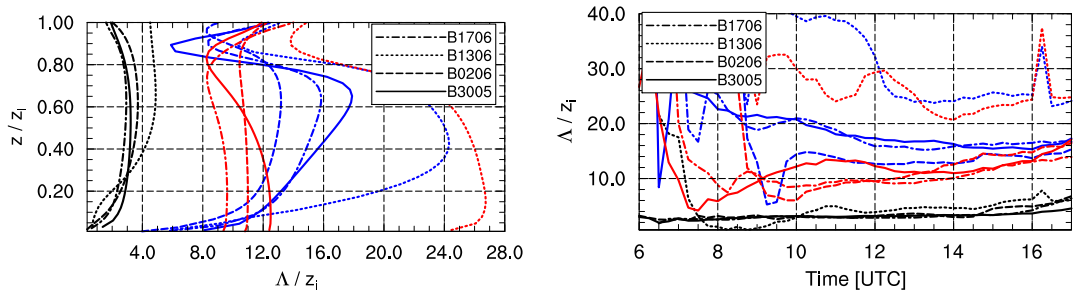

Figure 4.18: Profiles (a) and time series (b) of the dominant length scale Λ, calculated by Eq. 4.11, at 13 UTC , averaged over 1 h. The figure shows the length scales of $\widetilde{w'}$ (black), $\widetilde{\theta'}$ (blue) and $\widetilde{q'}$ (red).

bring forward larger length scales. This can be the case when no peak value in the spectra is found. The definition of Λ tries to eliminate this effect to a certain extent. On the other hand, in this case only a single dominant structure can occur in the model domain. This leads to the physical interpretation that the scalars scale with the model domain, if a moderate background wind is prescribed. Anyhow, case B1306 should be interpreted very carefully.

Summing up, the calculated dominant length scales $\Lambda_{\widetilde{w'}}$, $\Lambda_{\widetilde{\theta'}}$ show expected shapes, while $\Lambda_{\widetilde{q'}}$ is more or less constant with height, showing a different behavior. $\Lambda_{\widetilde{\theta'}}$ displays a high dependency on height, which is probably caused by vertical transport by the SC and wind shear. Since the scalar length scales in Fig. 4.18 (a) show no identifiable correlation with the background wind and partially different behavior, the boundary layer height as scaling parameter z_i might be applicable to the velocity length scales only. This coincides with Gopalakrishnan and Avissar (2000), who stated this problem as well and decided not to use z_i as scaling parameter. It was possible to prove that the length scales increase with increasing background wind by using the dominant length scale of the surface heat fluxes $\Lambda_{\overline{w'\theta'_0}}$ and $\Lambda_{\overline{w'q'_0}}$ as scaling parameters (not shown). This experimental scaling shows ratios $\Lambda_{\widetilde{\theta'}}/\Lambda_{\overline{w'\theta'_0}}$ and $\Lambda_{\widetilde{q'}}/\Lambda_{\overline{w'q'_0}}$ in the range of 0.5 to 1.9, which allows the speculation that the dominant mesoscale length scales of temperature and humidity are usually scaling with the dominant length scale of the surface heterogeneity. In any case, this concept needs further systematic investigation, which would exceed the scope of this study.

Temporal evolution of length scales Fig. 4.18 (b) shows the temporal development of Λ at $0.5z_i$. During the first hours of simulation time, Λ varies due to the quickly changing boundary layer conditions. Suitable results are thus found from 10 UTC onwards and case B1306 will be excluded from the interpretation due to the different behavior. $\Lambda_{\widetilde{w'}}$ is constant during the course of the day, but increases slightly in the last hour of simulation time, where the decay of the SC is already present. Pino et al. (2006b) studied the characteristic length scales during sunset turbulence and determined marginally increasing length scales for the vertical velocity and persistently increasing temperature length scales, which is in line with the run of the curves in Fig. 4.18 (b). $\Lambda_{\widetilde{q'}}$ in contrast is increasing considerably in time, which is also in agreement with Jonker et al. (1999) and De Roode et al. (2004). Suprisingly, $\Lambda_{\widetilde{\theta'}}$ seems to decrease slightly in time in case B3005, while the other cases show an increase in time. The latter cases are in agreement with the length scale evolution of $\widetilde{\theta'}$ and $\widetilde{q'}$ presented by De Roode et al. (2004). They showed that humidity and temperature structure develop at the same scale, both increasing in time, while the length scale of the vertical velocity remains constant. The minor

differences to the curves in the figure might be linkable to the time-dependent surface forcing in the simulations.

Conclusions This section showed that the characteristic length of scalar quantities is considerably larger than that of the vertical velocity. In comparison to several LES and observational studies, the heterogeneity induced quantities in the present study are dominated by larger scales up to mesoscale values between $9z_i$ and $26z_i$. In the presence of a strong background wind, the scalar quantities organize in bands oriented to the mean wind direction and smaller scale contributions are suppressed, leading to larger characteristic length scales.

The structures of $\widetilde{\theta}'$ and $\widetilde{q}'$ near the inversion layer are widely influenced by the structure of the interface between the inversion and the boundary layer and thus have to be treated separately. Occuring variances in the horizontal planes near the top of the boundary layer do not relate to structures in the lower boundary layer. Since both scalar quantities are not proportional to z_i, this scaling parameter can be called into question.

The temperature structures are generated by the surface heterogeneity and correlated to the SC, particularly near the surface, since updrafts correspond to warm rising air in comparison with the colder downdrafts. Updrafts are generated by local temperature gradients and dominated by larger scales in the middle of the boundary layer due to the fact that structures are affected and broadened by wind shear. Humidity structures do not seem to be much affected by wind shear, except case B1306, and display more or less height-constant characteristics. This yields to the assumption that updrafts are responsible for the vertical transport of humidity from the surface into the boundary layer. Of major importance for this transport process is the availability of water-vapor near the surface. Released water-vapor will be transported by horizontal compensational flows to areas with updrafts. By reason that both, the availability of water-vapor and the updrafts, are varying in space and time, the total transport is of accumulative nature. This idea follows the concept called "memory effect" (the scalar field is a result of a long history of up- und downdrafts) proposed by Jonker et al. (1999). This process is also affected by entrained air from the inversion layer above by downdrafts, which are typically of larger scales and which are transporting dry air downwards. As a consequence, the humidity structures appear to be more complex than temperature and velocity. On the one hand they are governed by the large-scale downdrafts of dry air and on the other hand updrafts are transporting available humidity from the surface to the top of the boundary layer. As explained, the latter are supposed to transport either dry or moist air, depending on the near surface conditions and thus can hardly be directly correlated to the humidity structures. The finding that the 2D-cross correlation $\rho_{\widetilde{w}',\widetilde{q}'}$ decreases in time, but shows medium to large correlations in the first hours of simulation time (not shown), supports this hypothesis, owing to the undeveloped effect of accumulation and broadening on the heterogeneity induced humidity. Section 4.2.5 further examines the mesoscale contribution to vertical fluxes of heat and latent heat.

The main question of the paper of De Roode et al. (2004), how large the model domain of LES studies should be to cover all relevant mesoscale fluctuations, has to be answered separately for simulations with non-homogeneous surface properties. The calculated dominant length scales reached values up to $26 \cdot z_i \approx 43$ km after 8.5 h of simulation time with a horizontal model domain size of 56 km $\times 56$ km. Thus, the statement by De Roode et al. (2004), to take into account the total simulation time (scalar mesoscale length scales increase in time) has to be adopted to heterogeneity induced fluctuations and with respect to background winds as well. Since no spectral peaks are found for mesoscale temperature structures (see Fig. 4.17, (b)), the consequences of larger border areas should be studied in future by using idealized surface

heterogeneities.

Boundary layer height and entrainment rate

This section deals with the temporal and spatial evolution of the boundary layer height and its impact on point measurements, which often use z_i as scaling parameter and are therefore sensible to variations. Furthermore, the impact of mesoscale circulations on the entrainment rate will be discussed. The evolution of the mean boundary layer height was already part of the analysis in section 4.2.1, but the local structure and development of the boundary layer depth under the influence of a heterogeneous forcing and SC and its impact on the entrainment is still an open question. Sullivan et al. (1998) showed, that rising plumes play an important role for entrainment processes and their folding effect on the interface to the overlying inversion layer. Avissar and Schmidt (1998), Raasch and Harbusch (2001) and Letzel and Raasch (2003) suggested a faster growth of the CBL, thus a higher entrainment rate due to a heterogeneous surface forcing. On the contrary, the study of Patton et al. (2005) found a dependency of the entrainment rate on the wave length of their idealized striplike surface heterogeneity. They stated that generally, the entrainment rate is more dependent on the rate of surface heating than on the scale of the heterogeneity. Nevertheless, they found a tendency of a decreased entrainment for wave lengths of the scale of the boundary layer height and increased entrainment for larger heterogeneities of $5-9\cdot z_i$. Recently, van Heerwaarden and Vilà-Guerau de Arellano (2008) disagreed with Avissar and Schmidt (1998) and Letzel and Raasch (2003) and stated that there is no impact of heterogeneities and found equal entrainment rates for heterogeneous and homogeneous surfaces, when the model is in quasi-stationary state.

In consideration of the relatively low resolution of the LITFASS simulations, a first assessment of the entrainment rate (also called entrainment velocity), defined as

$$w_e = \frac{\partial z_i}{\partial t}, \tag{4.12}$$

in a realistic diurnal cycle shall be part of this section. However, the main focus of attention is on the spatial variation of z_i and its possible causes. For the analysis of the boundary layer height a modified gradient method after Sullivan et al. (1998) is used. With the aid of this method it is possible to calculate a local boundary layer height $z_{i,loc}(x,y)$ at each horizontal grid point.

Boundary layer height The method of Sullivan et al. (1998) for the estimation of the PBL height z_i was modified by Uhlenbrock (2006) by adding a threshold gradient of $\Gamma = 0.2\ \mathrm{K/100m}$ z_i (see section 4.2.1), because the vertical profiles of temperature show inversions during the "Golden Days" (see Fig. 4.7, particularly initial profiles), that cannot be handled by the gradient method and would result in unrealistic boundary layer heights. For the present study a threshold of $0.3\ \mathrm{K/100m}$ was applied, because temperature gradients over heterogeneities with a very low sensible surface heat flux, such as lakes, exhibit inversions near the surface with temperature gradients (potential temperature was ensemble-averaged here) of the same magnitude as the threshold. With this modification, Eq. 4.6 can be written as

$$\begin{aligned} & z_{i,loc}(x,y) = z \quad \text{, where z is the lowest height level, where} \quad \frac{\partial\theta(x,y,z)}{\partial z} > \Gamma \\ \wedge \quad & \frac{\partial\theta(x,y,z')}{\partial z} \quad \text{is maximum with} \quad \Gamma = 0.3\ \mathrm{K/100m} \quad \text{and} \quad z' \in [z, z+4\Delta z]. \end{aligned} \tag{4.13}$$

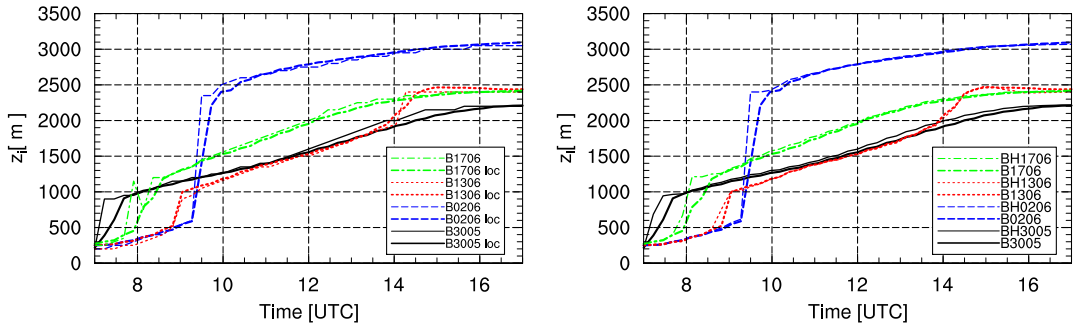

(a) z_i and $\overline{z_{i,loc}}$ (b) $\overline{z_{i,loc}}$ for the "Golden Days" and HCRs

Figure 4.19: Time series of the boundary layer height z_i for the "Golden Days" calculated with the gradient method.

Fig. 4.19 (a) shows the temporal evolution of the horizontal averaged local boundary layer height $\overline{z_{i,loc}}$ compared to the boundary layer height z_i, calculated from the averaged vertical temperature profile. The temperature field for the calculation was ensemble-averaged and time-averaged over 900 s to filter variations due to small-scale turbulence. Since the two calculation types show similar results, an superiority of $\overline{z_{i,loc}}$ over z_i can be excluded, but it yields information about the spatial variance. The run of the curves in detail was already discussed in section 4.2.1.

The comparison of the boundary layer height of the "Golden Days" with their respective HCRs (Fig. 4.19 (b)) shows a similar development for all cases, but the HCRs tend to reach slightly higher values of z_i ($50-100$ m higher), especially for the weak wind case B3005/BH3005. Since the vertical grid resolution of the simulations was 50 m and thus the differences of z_i are only in the range of $1-2$ numerical grid points, this outcome should not be overrated. Moreover, the eddies in the entrainment zone are smaller due to the stable stratification and thus the subgrid-scale part can make up a significant portion of the total fluxes. Fig. 4.20 shows horizontal cross-sections of $z_{i,loc}$ at 12 UTC. The cases B3005, B1306 and B1706 show absolute variations up to 10 % or even more, in contrast to case B0206 with variations up to 4 %. In case B3005, the surface heterogeneity clearly reflects in the modification of $z_{i,loc}$. Above areas with a high surface heat flux, updrafts rise above the nominal inversion and deeper in the free atmosphere, causing a folding and a higher $z_{i,loc}$. Areas of downdrafts are thus expected to have a lower $z_{i,loc}$. Particularly over the large forest patches in the western and northern part of the LFA the boundary layer is noticeably deeper, while underlying lakes can be linked to areas of low $z_{i,loc}$. The spatial distribution of up- and downdrafts might explain the tendency of a decreased mean boundary layer height in heterogeneous simulations, since mesoscale downdrafts are found to be weaker and of larger scale than updrafts. The distribution of the vertical velocity is thus left-skewed and more than the half of the horizontal area is characterized by downdrafts. In the other simulation cases, the updrafts are more influenced by wind shear, which yields a more smeared effect. As shown in section 4.2.3, the SCs are weaker in those cases. The folding of the local boundary layer height is shown in Fig. 4.21. Especially the weak wind case (Fig. 4.21, (a)) proves the statements above. Here, $z_{i,loc}$ can easily be linked to the underlying circulation. On the one hand, for instance at $y = 30.6$ km and $y = 33.5$ km, two strong updrafts (red) result in a double peak of $z_{i,loc}$. On the other hand, the larger area of a weak downdraft from $y = 12-30$ km displays an about 300 m lower boundary layer height. This correlation persists within most parts of the model domain. Anyhow, the pattern of Fig. 4.20 (a) differs from the SC structure (cf. Fig. 4.9), but one has to keep in mind two things. The first is, that the SC is varying in time and it is not sure, that the folding of the inversion interface happens at the same time scale ("memory effect", see also section 4.2.4). The second aspect is that the SC

was chiefly analyzed at $0.5 \cdot z_i$, but the variation of $z_{i,loc}$ is an effect taking place at the top of the boundary layer.

Fig. 4.21 (b) - (d)) also shows that updrafts exhibit horizontal velocity components in cases with background wind speed above $2\ \mathrm{m/s}$ due to increased wind shear and decreased circulation strength. Thus, the folding effect of $z_{i,loc}$ appears damped successively from case B3005 to B0206 in dependence of the background wind. The range of $z_{i,loc}$ is also smaller, especially in case B0206, with a height difference of only about $100\ \mathrm{m}$. Generally speaking, the variation of the local boundary layer height seems to be dependent on the SC strength, which itself is highly related to the background wind, as well as the boundary layer height. The normalized standard deviation $\sigma z_{i,loc}/\overline{z_{i,loc}}$ (Fig. 4.22) specifies this more quantitatively. In the morning hours until 10 UTC, $\sigma_{z_{i,loc}}/\overline{z_{i,loc}}$ is quite high, with values up to more than 30 %, because nocturnal inversions dissipate during this time. As already mentioned, residual layers persist atop the inversions, which are leading to a fast growth of the boundary layer as the inversions dissipate (see. Fig. 4.19 (b)). Strong updrafts tear down the inversion at some locations and can rise up to the top of the residual layer, while, at the same time, updrafts at other locations are still vertically limited by the inversion. The result is a high variance of the boundary layer height (not shown). After 10 UTC the variance is more or less constant and inversions have disappeared with one exception: case B1306 shows another peak at 14 UTC, owing to the dissipation of a secondary inversion. A corresponding jump in $z_{i,loc}$ is also shown in the time series (Fig. 4.22). At 12 UTC, the variances hold value between 4 % (case B3005) and 1 % (case B0206). It confirms the previous conclusions from Fig. 4.21 and is in agreement with Uhlenbrock (2006), who found the similar characteristics, but a higher standard deviation up to 10 % at 12 UTC. This enhancement might be due to variations caused by small-scale turbulent structures, which were filtered in the present study.

The HCRs display a significant lower variance in comparison with their respective cases B3005, B1306 and B1706, owing to the absence of mesoscale circulations. The small variance in the simulations B0206 and BH0206 is due to the enormous depth of the residual layer, which is leading to a significant higher boundary layer extent in the course of day. The mesoscale circulation scales with z_i and therefore heterogeneities of smaller scales do not affect the CBL, as was pointed out by Shen and Leclerc (1995) and Raasch and Schröter (2001). Thus, less and broader updrafts are expected to cause lifting $z_{i,loc}$ at a large horizontal size but only small vertical extent (Uhlenbrock, 2006).

Sullivan et al. (1998) found a $\sigma_{z_{i,loc}}/\overline{z_{i,loc}} \sim Ri^{-1}$ power law, with the Richardson number Ri, defined as

$$Ri = \frac{\Delta\theta}{\theta_*} \quad , \tag{4.14}$$

where θ_* is the temperature scale and $\Delta\theta$ is the temperature jump between the height where $\overline{w'\theta'}(z)$ is the minimum (z_1) and the height, where the flux vanishes (z_2). Thus, Ri can be considered as a measurement for the inversion strength atop the CBL. Ri was calculated for the LITFASS simulations to verify whether the power law is also valid for heterogeneous surfaces. Representative values of Ri and the standard deviations in the period from 10 UTC to 13 UTC were averaged over $30\ \mathrm{min}$. During this period, the standard deviations were relatively constant and no fast jumps of z_i occured (see Figs. 4.19 (b) and 4.22). In Fig. 4.23, $\sigma_{z_{i,loc}}/\overline{z_{i,loc}}$ is plotted against the Richardson number for the LITFASS simulations (a) and the HCRs (b). Results of Uhlenbrock (2006) and Sullivan et al. (1998) were added to the plot. For heterogeneous forcing, there is evidence that the power law is roughly valid and $\sigma_{z_{i,loc}}/\overline{z_{i,loc}}$ is dependent on the inversion-layer strength, expressed by Ri. All obtained values are in the same range as the values of Sullivan et al. (1998). The results of Uhlenbrock (2006) show higher variances for similar Ri, but this finding was already explained above. The standard deviations of case

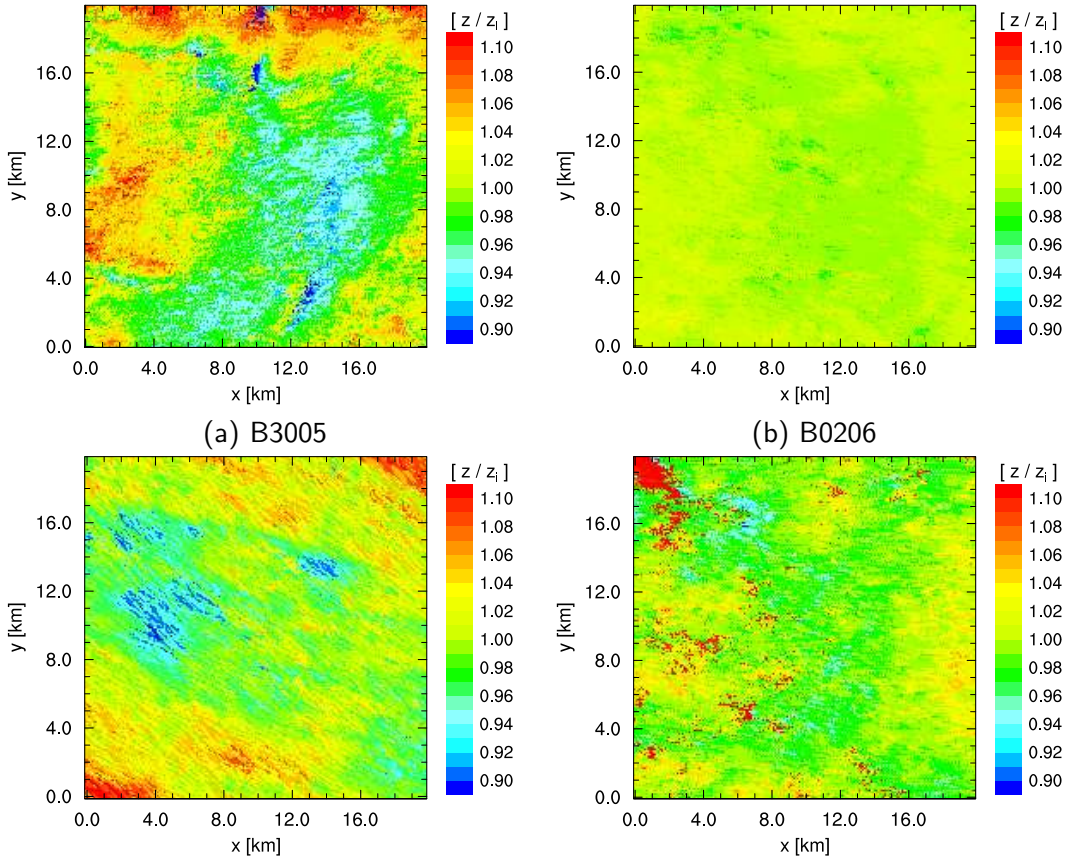

(a) B3005 (b) B0206

(c) B1306 (d) B1706

Figure 4.20: xy-cross-sections of the local boundary layer height at 12 UTC, averaged over 10 min and normalized by the horizontal mean $\overline{z_{i,loc}}$. Values < 0.9 were set to 0.9 and values > 1.1 were set to 1.1 for a more clearly outlook.

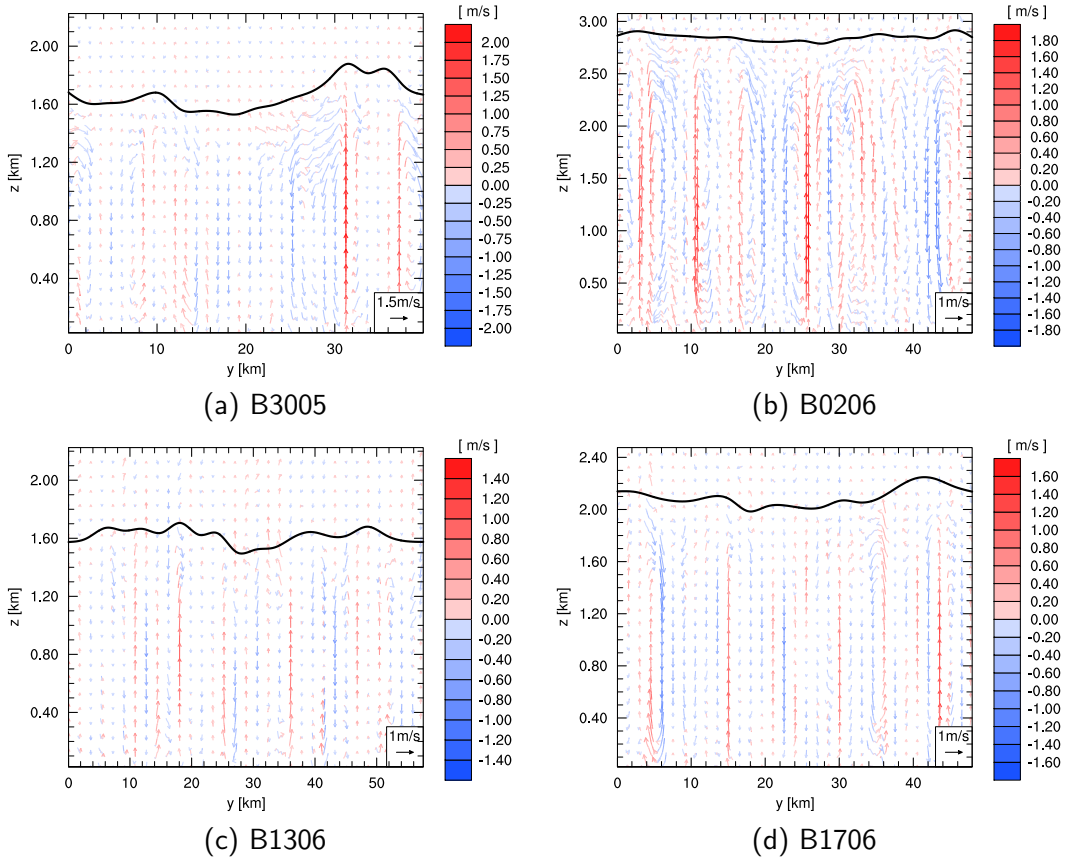

Figure 4.21: yz-cross-sections of the local boundary layer height (thick line, added smoothing filter) at the location $x = 24$ km along with the flow vector $(\widetilde{v}', \widetilde{w}')$ at 12 UTC, averaged over 900 s. The cross-sections are oriented relatively across the mean wind. The vectors are colored with the vertical velocity component.

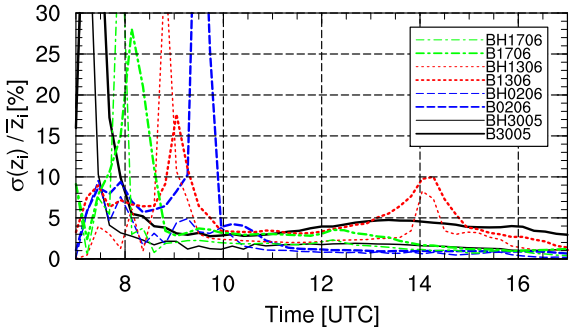

Figure 4.22: Time series of the standard deviation $\sigma_{z_{i,loc}}$, normalized by the mean $\overline{z_{i,loc}}$.

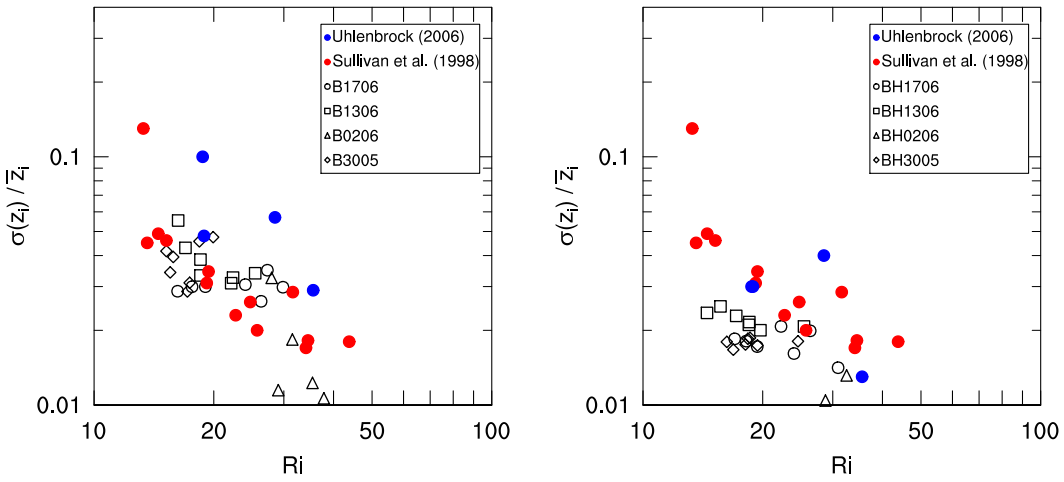

(a) "Golden Days" (b) HCR

Figure 4.23: Comparison of the normalized standard deviation of $z_{i,loc}$ against Ri for the LITFASS simulations in the period $10-13$ UTC and LES of Sullivan et al. (1998) and Uhlenbrock (2006). Values of the current LES are time-averaged (30 min).

B0206 (triangles) in general hold smaller values between 0.01 and 0.02, owing to the large depth of the residual layer, causing a very deep boundary layer. The respective plot for the HCRs shows smaller values than the heterogeneous case, but the standard deviation still follows the proposed power law. In any case, Sullivan et al. (1998) investigated free convective flows without shear in contrast to the present simulations with background winds between $2\ \mathrm{m/s}$ and $6\ \mathrm{m/s}$. Furthermore, the present study only investigated the mesoscale effect, as already mentioned, so a direct comparison is critical to perform.

The dependency of $\sigma_{z_{i,loc}}/\overline{z_{i,loc}}$ on the mean boundary layer depth leads to the speculation that residual layers, or rather the absolute boundary layer height, might have an effect beside the strength of the SC and the inversion-layer depth, because heterogeneities $< \overline{z_{i,loc}}$ do not affect the flow. Thus, the folding of the inversion interface and consequently the spatial variance decreases with the mean boundary layer depth.

Entrainment Entrainment processes have been investigated extensively over the last decades. Various LES studies have been carried out in the recent years that investigated the entrainment rate and its modeling in wind-shear driven (e.g. Pino et al., 2006a; Sun and Xu, 2009) and free convectively driven boundary layers (e.g. Fedorovich et al., 2004; van Heerwaarden and Vilà-Guerau de Arellano, 2008). The growth of the boundary layer from LES can be compared to predictions by so-called jump models, that are based on the assumption that the spatial-averaged profiles of potential temperature experience jumps in the inversion layer. The question remains how the entrainment rate behaves under realistic conditions and heterogeneous forcing and whether jump models show any sensitivity or not.

Since w_e was defined as the temporal derivative of z_i, Fig. 4.19 (b), provides a first overview (hereafter z_i will be used for notation instead of $\overline{z_{i,loc}}$). In the period from 10 UTC to 14 UTC, no significant deviations of the LITFASS simulations from their HCRs appear. Overall, the HCRs lead to slightly higher z_i, consequently the entrainment has to be higher as well. Especially for case B3005 this is apparent. This is unexpected, because the horizontal z_i variances are smaller, which should lead to a smaller entrainment rate (see Fig. 4.22). The profiles of $\overline{w'\theta'}$ at 12 UTC (Fig. 4.24) confirm a higher entrainment for homogeneous in comparison with the

heterogeneous heated surfaces. For the latter cases, on the one hand, the absolute minimum of the flux is up to 4 % (20 $\mathrm{W/m^2}$, B3005) smaller, but on the other hand, the top of the entrainment zone (height of the first zero crossing of the heat flux) is increased. Nevertheless, the sum of the entrainment flux is somewhat smaller than in the homogeneous case. The reasons remain unclear. Lilly (2002) pointed out that the process of horizontal averaging in LES can cause an underestimation of the vertical heat flux even for very small local fluctuations of z_i. van Heerwaarden and Vilà-Guerau de Arellano (2008) varied the amplitude of the surface heat flux for idealized two-dimensional heterogeneities and found a less total entrainment than in a homogeneous case for small amplitudes, but a larger entrainment for larger amplitudes. They brought forward the argument of Lilly (2002) and concluded that their different entrainment rates are a result of the model spinup. The present study cannot approve this theory, but assuming an artificial underestimation in the vertical heat flux would be inconsistent with the findings from Fig 4.19(b), which should not be affected by this effect, since they are calculated from local temperature profiles and spatial average was carried out afterwards.

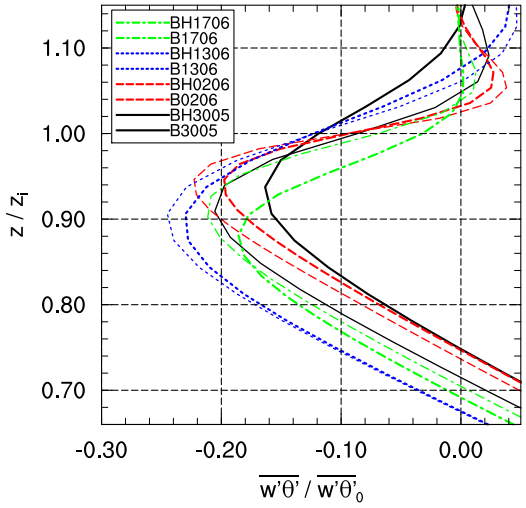

Figure 4.24: Vertical profiles of $\overline{w'\theta'}$ in the entrainment zone at 12 UTC, spatial-averaged.

Shen and Leclerc (1995) showed that w_e is larger over surface patches with a large surface heat flux in comparison to those with a small heat flux. This is in accordance to the finding that rising plumes over warmer areas in absence of a background wind penetrate deeper into the inversion layer, causing an enhanced entrainment and a higher spatial variance of the inversion interface. Following this concept, adapted for instance to case B3005, a higher entrainment could be expected over forest patches, while less entrainment should occur over, for example, the lakes. If the ratio between the surface forcing and the entrainment rate atop is of non-linear character, this could yield to a slightly different total entrainment in dependence of the heterogeneity distribution. Since z_i grows equally statistical horizontal in the HCRs, compensation effects due to horizontal gradients are not present and the total entrainment might be modified as well.

In thermally driven convective tank simulations, Deardorff and Stockton (1980) found the dimensionless entrainment rate to vary as

$$\frac{w_e}{w_*} = \frac{A}{Ri} \tag{4.15}$$

for typical atmospheric values of Ri. w_* is the convective velocity scale and A is a parameter in the range $0.1 < A < 0.2$. Betts (1974) showed a first-order jump model for an estimation of the

entrainment rate:

$$w_e \Delta\theta = -\overline{w'\theta'}_{min} + \Delta z \frac{\partial \theta^{12}}{\partial t} \quad . \tag{4.16}$$

Here, $\Delta\theta$ is the potential temperature jump between z_1 and z_2, as defined in Eq. 4.14, $\Delta z = z_2 - z_1$ is the inversion layer thickness and $\overline{w'\theta'}_{min}\left(=\overline{w'\theta'}(z_1)\right)$ is the minimum buoyancy flux. $\theta^{12} = [\theta(z_1) + \theta(z_2)]/2$ is the average temperature between z_1 and z_2. Eq. 4.16 can in terms of Ri (see Eq. 4.15) be written as

$$\frac{w_e}{w_*} = \frac{(A_{w\theta} + A_{\Delta z})}{Ri} \quad \text{, where the parameter A is now split up in} \tag{4.17}$$

$$A = A_{w\theta} + A_{\Delta z} \quad \text{with} \quad A_{w\theta} = -\frac{\overline{w'\theta'}_{min}}{\overline{w'\theta'}_0} \quad \text{and} \quad A_{\Delta z} = \frac{\Delta z}{\overline{w'\theta'}_0}\frac{\partial \theta^{12}}{\partial t}$$

For a comparison of the LES results with the predictions by the jump model, w_e/w_* was calculated from the time-averaged z_i (direct) in the period of $10-13$ UTC and from the horizontal averaged profiles of $\overline{w'\theta'}(z)$ and $\theta(z)$ (jump model). The predictions by the jump model for the HCRs are shown in Fig. 4.25 (b). Despite the tendency to underestimate the directly calculated entrainment rate, the scattering can be rated as small and the ratio of w_e/w_* to A/Ri is approximately constant. The entrainment rates resemble the order of magnitude of the values obtained by Sullivan et al. (1998) (cf. Sullivan et al., 1998, Fig. 22). Furthermore, case BH0206 displays a considerably smaller entrainment than the other cases. Summing up, the first-order jump-model reproduces the actual values very well, despite the diurnal cycle in the surface forcing and wind-shear. The application to the "Golden Days" simulations shows a larger scattering (Fig. 4.25 (a)) and points out, that the jump model might not generally be applicable to heterogeneous surfaces. The scattering distribution leads to assume that it tends to overestimate small values w_e/w_* (here up to 0.015), but underestimate larger entrainment rates. Pino et al. (2006a) and Sun and Xu (2009) used first-order models for a comparison with LES, too, and found their LES data generally to be overestimated by the model. The present study cannot confirm this result, but this must not be misconceived, simply because these studies used CBLs in steady-state conditions and with idealized initial stratification.

Conclusions The mesoscale circulations have a non-negligible effect on the local boundary layer height. Around noon, when local temperature inversions have vanished, it is leading to a standard deviation up to 5 % in dependence of circulation strength, average boundary layer depth and background wind. The power law $\sigma_{z_{i,loc}}/\overline{z_{i,loc}} \sim Ri^{-1}$ (after Sullivan et al., 1998) becomes apparent to be valid for the heterogeneous time-dependent surface forcing of the LITFASS simulations with certain synoptic conditions. Since the spatial variation of $z_{i,loc}$, point measurements are expected to be afflicted with an error of about 10 % due to mesoscale circulations. Above heterogeneous surfaces, inversions dissipate faster above strong heated patches, which is leading to a substantial spatial variance of the boundary layer depth. Against this background of extant inversions, z_i as scaling parameter from measurements is problematic. Generally speaking, with no or only weak background wind, the boundary layer above patches of a strong surface heat flux, such as forests, is significantly higher than above less heated surfaces, for instance lakes of a certain extent.

There is still no consensus in the scientific community whether there is an effect of surface heterogeneities on the mean boundary layer height or, more precisely, on the entrainment rate, and if it is a positive or rather negative effect. The present study reveals a slightly decreased entrainment velocity compared to homogeneous simulations with an equal heat input in the atmosphere. Reasons for this decrease might be ascribed to the left-skewness

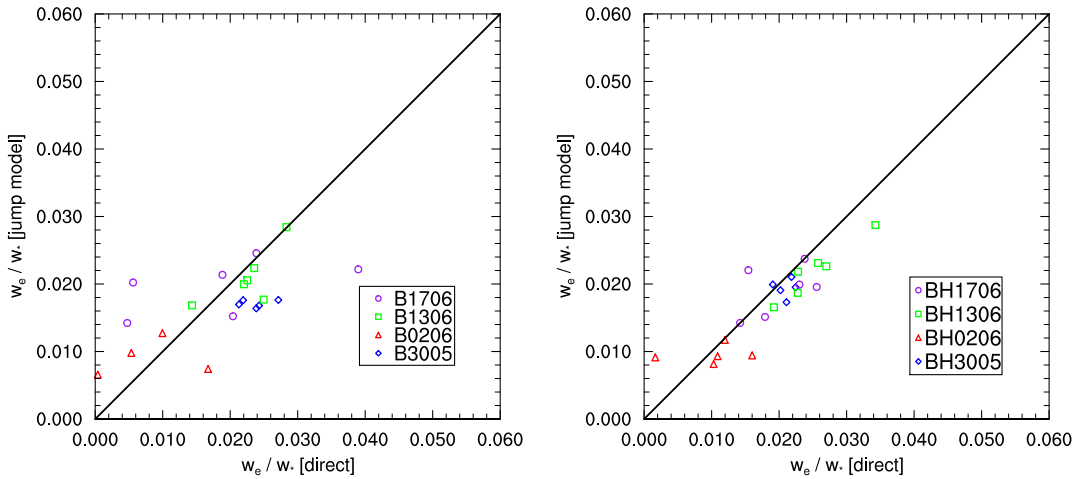

(a) "Golden Days" (b) HCRs

Figure 4.25: Comparison of the normalized entrainment rate w_e/w_*, calculated directly from LES data, to a first-order jump model (see Eq. 4.17). (a) shows results for the "Golden Days", (b) for the HCRs. All values are time-averaged over 30 min. The solid line represents w_e/w_* (direct) $= w_e/w_*$ (jump model).

of the horizontal vertical velocity distribution of the SCs. Since the grid resolution was of the order of the differences in z_i, conclusions have to be made very carefully and should not be overrated. However, the vertical profiles of $\overline{w'\theta'}$ showed that the heat flux minima in the entrainment zone is up to 20 $\mathrm{W/m^2}$ lesser than in the HCRs. Possible causes for the results might be artifical underestimation, generated by horizontal averaging (Lilly, 2002) or non-linear interactions between surface forcing and local boundary layer height, that is leading to different local entrainment rates. As will be shown in section 4.2.5, the vertical transport of heat is accomplished by mesoscale circulations to a significant portion (including the entrainment zone). The question, whether entrainment is modified by mesoscale structures, will be part of this study in section 4.2.5.

A simple first-order model after Betts (1974) provides good estimations of w_e/w_* for homogeneous and is still suitable for heterogeneous surface patterns under real synoptic conditions. Systematical overestimations of the entrainment rate, found in previous idealized studies, cannot be confirmed.

4.2.5 Mesoscale contribution to turbulent vertical fluxes

The mesoscale contribution at 13 UTC

This last section in the framework of the analysis of turbulence structures in the boundary layer is concerned with the contribution of heterogeneity induced quantities to vertical fluxes. The main question, if total vertical turbulent fluxes can be enhanced or decreased in the presence of surface heterogeneities under different synoptic conditions, is still not sufficiently investigated. The previous section 4.2.4 pointed out, that the influence, for instance on the entrainment flux, has been discussed in literature without a genereal consensus yet. Since secondary circulations were found in section 4.2.3 with length scales of the order of the grid spacings of NWP models, this section might enlighten the quantitative and qualitative contribution induced by surface heterogeneities in the diurnal cycle.

The mesoscale fraction can be calculated by decomposing the total flux into global-, meso- and small-scale parts according to Eq. 3.11 in section 3.3. The global-scale subsidence was applied by correcting the temperature profile after every time step, so the horizontally averaged vertical velocity equals zero due to continuity reasons for all simulations at all heights and $\overline{w}(z)\overline{\Phi}(z) = 0$. Contrary to the visual analysis of the SC, this analysis uses the entire model domain for averaging to benefit from the fact, that the global part is zero. Therefore Eq. 3.11 reduces to

$$\overline{w\Phi} = \overline{\widetilde{w'}\widetilde{\Phi'}}(z) + \overline{w''\Phi''}(z) \quad , \tag{4.18}$$

where $\overline{\widetilde{w'}\widetilde{\Phi'}}(z)$ is again the mesoscale and $\overline{w''\Phi''}(z)$ the small-scale turbulent fraction.

The profiles of the turbulent fluxes $\overline{w\theta}$, $\overline{wq}$ at 13 UTC (Fig. 4.26) show classical characteristics, as was already discussed in section 4.2.2 (please note that $\overline{w\Phi}$ here is a turbulent flux, commonly written as $\overline{w'\Phi'}$). Owing to the fact that the simulations B0206 and B1706 were found to generally show negligible differences in the flux characteristics, only profiles of B1706 are presented. Moreover, the mesoscale and small-scale fractions as well as the total flux from the HCRs for comparison are added to the plots. The mesoscale fraction $\overline{\widetilde{w'}\widetilde{\Phi'}}$ exhibits a value of 0 at the surface, because it only includes resolved-scale fluctuations. The subgrid-scale contribution in the lower boundary layer is dominant, so it can be concluded that the near-surface structures are not significantly influenced by the SC. SCs of smaller scales that might persist near the surface cannot be resolved.

The mesoscale vertical heat flux $\overline{\widetilde{w'}\widetilde{\theta'}}$ displays maximum values at $0.3z_i$ and minimum values at $0.9z_i$ (Fig. 4.26 (a) - (c)). The peak values are dependent on the strength of the SC and vary between $0.03 - 0.13 \cdot \overline{w'\theta'}_0$, since $\widetilde{w'}$ is dependent on the background wind. $\overline{\widetilde{w'}\widetilde{\theta'}}$ increases with height, due to an increase with height of $\widetilde{w'}$. The maximum is located below the maximum of the vertical velocity, because the variance of $\widetilde{\theta'}$ decreases with height (see Figs. 4.11 (c) and 4.14 (a)). The minimum in the entrainment region is in all cases located in the same height as that of the total flux. Here, $\widetilde{w'}$ is relatively small, but $\widetilde{\theta'}$ exhibits a high variance near the inversion interface. The peaks refer to percental values between 8 % (B1306) and 20 % (B3005) of the total flux. In general, it is shown that the small-scale contribution $\overline{w''\theta''}$ is decisive for the total flux. These results are in agreement with the LES studies of Patton et al. (2005) and van Heerwaarden and Vilà-Guerau de Arellano (2008) (the latter presented the virtual potential temperature instead of the potential temperature). In comparison to the study of Uhlenbrock (2006), the mesoscale contribution gained little higher values in the present study for case B3005 (the other cases were not investigated by Uhlenbrock (2006)). As was already stated, the entrainment zone shows slightly smaller entrainment fluxes in the presence of surface heterogeneities in comparison to the HCRs (cf. Fig. 4.24), but no differences occur within the lower part ($z \leq 0.7z_i$) of the boundary layer. Hence, it can be concluded that the vertical transport of heat is partly taken over by the SC but does not imply an enhancement of the total transport of heat in the boundary layer.

A quadrant analysis provides further information about $\overline{\widetilde{w'}\widetilde{\theta'}}$ and the transfer processes by separating the fluctuations $\widetilde{w'}$ and $\widetilde{\theta'}$ according to their sign. The resulting quadrants for a given flux $\overline{\widetilde{w'}\widetilde{\Phi'}}$ can be named and numbered after Shaw et al. (1983) and Katsouvas et al. (2007) as follows:

- Quadrant 1 (Q_1): $\widetilde{w'} > 0, \widetilde{\Phi'} > 0$: ($\overline{\widetilde{w'_{(+)}}\widetilde{\Phi'_{(+)}}}$, ejections)
- Quadrant 2 (Q_2): $\widetilde{w'} > 0, \widetilde{\Phi'} < 0$: ($\overline{\widetilde{w'_{(+)}}\widetilde{\Phi'_{(-)}}}$, outward interactions)

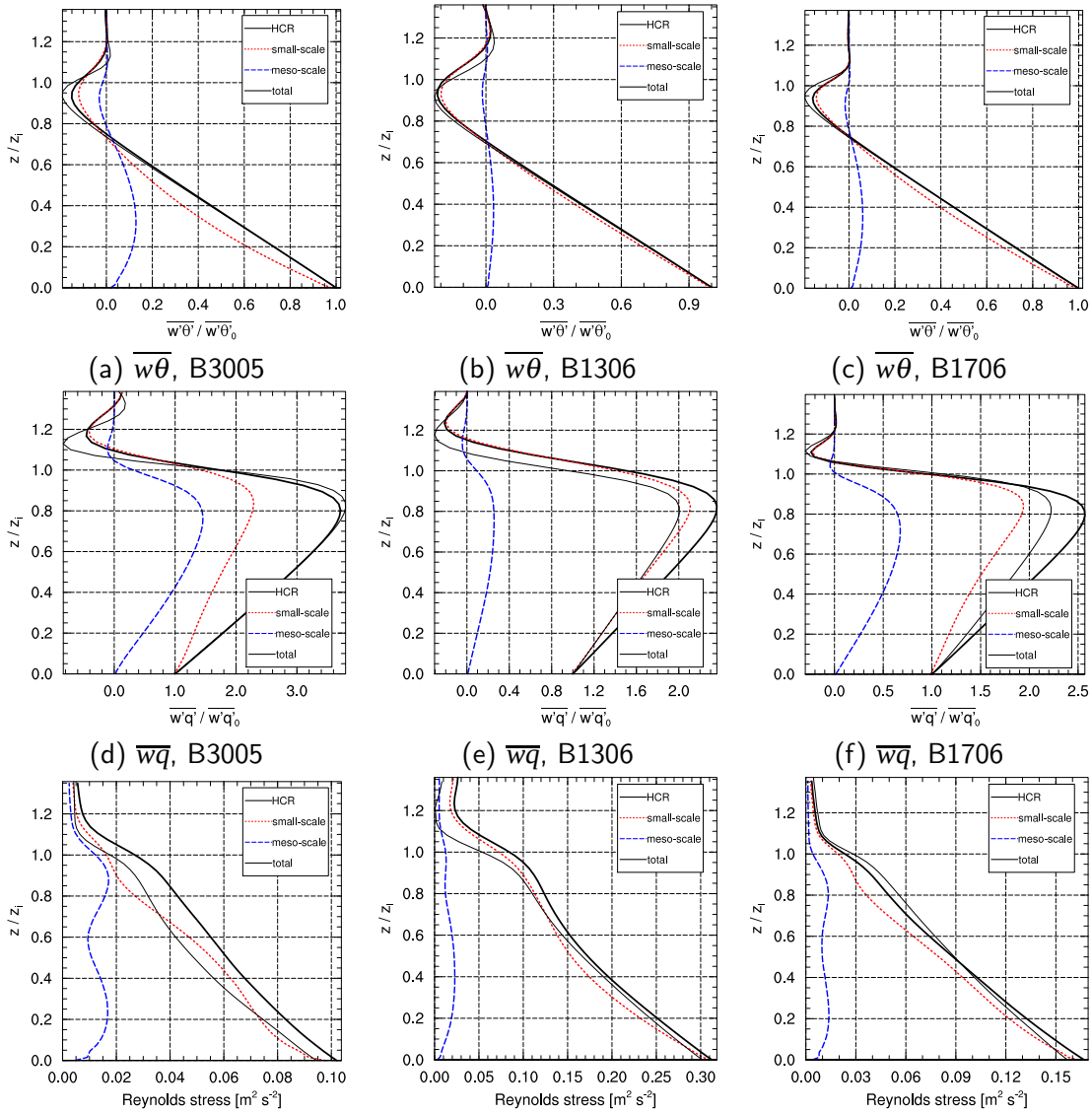

(a) $\overline{w\theta}$, B3005 (b) $\overline{w\theta}$, B1306 (c) $\overline{w\theta}$, B1706

(d) $\overline{wq}$, B3005 (e) $\overline{wq}$, B1306 (f) $\overline{wq}$, B1706

(g) R, B3005 (h) R, B1306 (i) R, B1706

Figure 4.26: Vertical profiles of sensible (a - c) and latent (d-f) heat fluxes and Reynolds stress (g - i) at 13 UTC, time-averaged over 1 h. The total fluxes (black, thick solid line) are decomposed into small-scale (red, short-dashed) and mesoscale (blue, dashed) parts. For comparison, the total fluxes of the respective HCRs are also plotted (black, thin solid line).

- Quadrant 3 (Q_3): $\widetilde{w'} < 0, \widetilde{\Phi'} < 0$: ($\overline{\widetilde{w'_{(-)}}\widetilde{\Phi'_{(-)}}}$, sweeps)
- Quadrant 4 (Q_4): $\widetilde{w'} < 0, \widetilde{\Phi'} > 0$: ($\overline{\widetilde{w'_{(+)}}\widetilde{\Phi'_{(+)}}}$, inward interactions)

The quadrants 1 and 2 correspond to positive, thus upward, transport of $\widetilde{\Phi'}$, and quadrants 3 and 4 to downward transport of $\widetilde{\Phi'}$. Mahrt and Paumier (1984) illustrated the interpretation for heat fluxes (see Fig. 4.27). Following this interpretation, Q_1 is related to rising thermals, whereas Q_4 is the entrainment flux. The other quadrants can be interpreted as penetrative convection (Q_2), and a flux due to compensational motions (Q_3).

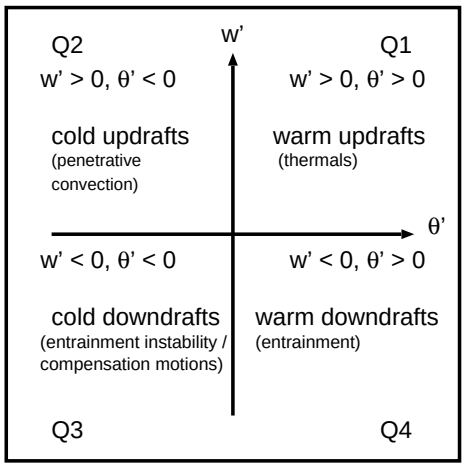

Figure 4.27: Exemplary schematic figure of the quadrant analysis for the vertical heat flux, modified after Mahrt and Paumier (1984) and Sullivan et al. (1998).

Since B3005 was mostly and B1306 was least modified by the mesoscale heat flux, the quadrant analysis is shown for these two case only (Fig. 4.28 (a),(c)). Case B3005 will be discussed in detail, while only significant differences of B1306 compared to case B3005 will be reported. Within the lower boundary layer, $\overline{\widetilde{w'_{(+)}}\widetilde{\theta'_{(+)}}}$ and $\overline{\widetilde{w'_{(-)}}\widetilde{\theta'_{(-)}}}$, that is to say rising thermals and compensational cold downdrafts, contribute most to the total flux. $\overline{\widetilde{w'_{(+)}}\widetilde{\theta'_{(+)}}}$ is found to be somewhat higher than $\overline{\widetilde{w'_{(-)}}\widetilde{\theta'_{(-)}}}$, since the latter also contains entrained warmer air, which is reducing the magnitude of $\theta'_{(-)}$. Near the top of the boundary, there are some interesting features that were already discussed by Sullivan et al. (1998), who decomposed the total heat flux with the aid of quadrant analysis in the entrainment zone. The upper peaks of the four flux components are located near z_i, while the resulting total flux minimum is shifted downwards to $0.93z_i$. This was also shown by Sullivan et al. (1998) who concluded that the fluxes must be self-canceling to a great extent. They found the peak magnitudes of all four flux components to be larger than the total flux peak. Fig. 4.28 (a) shows a noteworthy difference to this finding. Only $\overline{\widetilde{w'_{(+)}}\widetilde{\theta'_{(-)}}}$ exhibits a higher magnitude than the total flux. Near the top of the boundary layer, $\widetilde{\theta'_{(-)}}$ is linked to rising thermals, that are colder in comparison to the warm ambient air in the inversion layer, so the interpretation as penetrative convection fits quite well. Due to the high stability in the inversion layer, this flux might be re-directed downwards and thus make up a large fraction of flux $\overline{\widetilde{w'_{(-)}}\widetilde{\theta'_{(-)}}}$ (Sullivan et al., 1998). Even more interesting in consideration of the findings above is the absence of a peak of the entrainment flux $\overline{\widetilde{w'_{(-)}}\widetilde{\theta'_{(+)}}}$ at the top of the

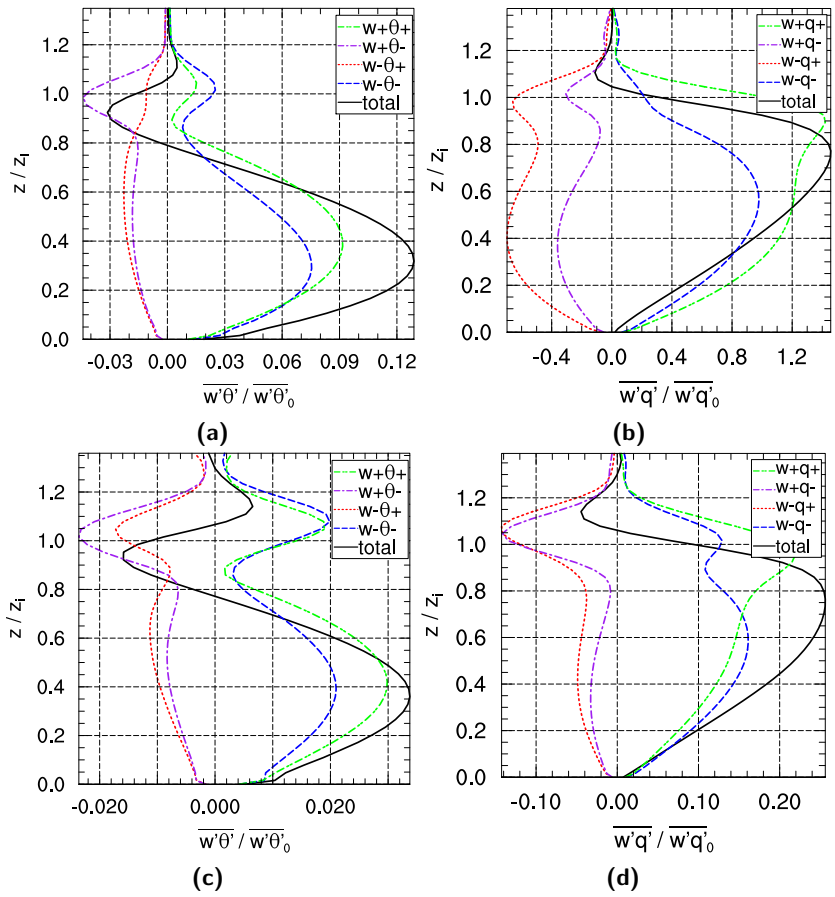

Figure 4.28: Quadrant analysis of the mesoscale vertical sensible (a,c) and latent (b,d) heat flux at 13 UTC for cases B3005 and B1306, time-averaged over 1 h. The solid black line represents the sum of the four quadrant contributions.

boundary layer, which fits in very well with the hypothesis that the entrainment is decreased due to SCs, which is also resulting in the modified minimum of the total flux. A comparison with the other cases shows that the development of a peak is clearly dependent on the SC strength (not shown). Case B1306 exhibits a distinct peak, which is higher in magnitude by a factor of 1.6 than the minimum in the lower boundary layer (Fig. 4.28 (c)). The other two cases B0206 and B1706 exhibit at least a small peak at z_i, which is smaller in magnitude than the secondary minimum as it is the case in B3005.

The vertical profiles of the decomposed latent heat flux contributions depict the enhanced relative fraction of the mesoscale flux and interesting impacts on the total flux $\overline{w'q'}$ (see Fig. 4.26 (d) - (f)). First of all, the contribution is again depending on the SC strength. The shape of the mesoscale fraction is similar to the shape of $\overline{w'q'}$, but maximum and entrainment minimum (of moist air) are slightly shifted downward. The maximum is found at $z = 0.7 - 0.8 z_i$ and varies between 11 % (B1306) and 39 % (B3006) of the according total flux. Uhlenbrock (2006) reported a smaller mesoscale contribution in case B3005. The findings of the present study suggest a smaller mesoscale fractions than the results of Patton et al. (2005), who found mesoscale fractions to contribute the bulk of the overall flux under certain conditions.

Contrary to $\overline{w'\theta'}$, $\overline{w'q'}$ is modified to a considerable extent. The peak value is increased up to 18 % in case B1306, while in case B3005, an insignificant decrease is found (≈ 2 %). This is surprising, since the total flux is rather expected to approach the HCR, if the SC weakens

and finally vanishes. On the other hand, the entrainment peak magnitude, where moist air is entrained into the boundary layer ($\overline{w'q'} < 0$), displays decreased magnitudes of $\overline{w'q'}$ in all cases. A first consequence of this finding is that a weak SC with developed roll-like structures seems to widely influence the transport of latent heat. Case B1306 has another remarkable feature which is associated with the small-scale flux contribution. In this case, $\overline{w''q''}$ is even larger than the HCR total flux (see Fig. 4.26 (e), $z = 0.8z_i$), leading to the implication that the surface heterogeneity must be responsible for an additional production of small-scale turbulence.

The plotted quadrant analysis results show latent heat flux distribution for the two cases B3005 and B1306, owing to their different total fluxes in comparison with their HCRs (Fig. 4.28 (b), (d)). The interpretation can be formulated analogously to the sensible heat flux (see Fig. 4.27), but here, the entrainment flux is $\overline{\widetilde{w'_{(-)}}\widetilde{q'_{(-)}}}$ owing to the fact, that the air in the inversion layer is very dry. $\overline{\widetilde{w'_{(+)}}\widetilde{q'_{(+)}}}$ is the dominant fraction in case B3005 and also the dominating part at least in the upper boundary layer in B1306. The entrainment flux $\overline{\widetilde{w'_{(-)}}\widetilde{q'_{(-)}}}$ is the second largest fraction in case B3005, but becomes even the largest in the lower part of the boundary layer in B1306. Furthermore an entrainment peak has developed at the top of the boundary layer. Taking into account cases B0206 and B1706, it is quite evident that this transition is continuous (not shown). Furthermore, it is visible that, on the one hand, the contribution of the downward fluxes up to $z = 0.8z_i$ is also depending on the SC strength and only of minor importance in case B1306. On the other hand, the respective contribution near $z = z_i$ is increased in case B1306. It is also noticeable, that $\overline{\widetilde{w'_{(+)}}\widetilde{q'_{(-)}}}$ approaches $\overline{\widetilde{w'_{(-)}}\widetilde{q'_{(+)}}}$. The latter finding points out that there is more vertical transport of negative humidity fluctuations which can be addressed to an enhanced entrainment of dry air into the boundary layer, as it is shown in Fig. 4.26 (e). In general, the findings are conform with all previous analysis results of the entrainment process at the top of the boundary layer.

For the additional flux contribution, the quadrant analysis is not able to provide explanations, since the total contribution of the mesoscale fraction is inversely proportional to the flux increase compared to the HCRs. It is also visible that the decreased entrainment of moist air, which must be originated from the boundary layer itself, cannot compensate for the additional flux in any way. The fact, that even the small-scale flux is higher than the HCR flux (case B1306) clarifies that there must be another process which is leading to this enhanced flux. It might be caused by the heterogeneous distribution of $\overline{w'q'}_0$. Kimmel et al. (2002) investigated the interaction of advected mesoscale conservative scalar fields (potential temperature and humidity) and the boundary layer turbulence. They figured out that this interaction produces smaller-scale scalar fluctuations. Despite the non-applicability of this result to the present study, it might be a starting point for further investigations to suggest the additional production of small-scale fluctuations due to heterogeneity induced mesoscale fluctuations $\widetilde{q'}$ by interaction with the small-scale turbulence in presence of a strong background wind or as a result of the roll-like structure of the SC. This would be also in agreement with the LES study of Kang (2009), who reported a break-up process of atmospheric fluctuation at the heterogeneity scale to smaller-scale fluctuations. Moreover, the transition of the total flux from a strong SC (e.g. B3005) to the HCR flux must be continuous as well. The findings above imply the existence of conditions which provide a maximum increase of $\overline{w'q'}$.

Beside the scalar flux $\overline{w'q'}$, the dynamical fluxes $\overline{w'u'}$, $\overline{w'v'}$ are affected by fractions of heterogeneity induced fluctuations as well. The decomposed dynamic fluxes are plotted in Fig. 4.26 (g) - (i), written as Reynolds stress R, which is defined as

$$R = \sqrt{\overline{w'u'}^2 + \overline{w'v'}^2} \quad . \tag{4.19}$$

The turbulent boundary layer flow is driven by the geostrophic wind, which is becoming less affected by surface friction with height. The total Reynolds stress is therefore roughly decreasing linear with height, but shows a konvex shape, which is interrupted by a konkav shape from $z = 0.7z_i$ to the top of the boundary layer. The near-surface values increase with wind speed (0.13 to 0.31 $\mathrm{m^2/s^2}$), because a higher geostrophic wind is leading to a higher throughput of kinetic energy from the top of the boundary layer to the surface and to a downward momentum flux (due to the definition of R, the flux appears positive). Needless to say, the dependency on the circulation strength is also the dispositive parameter of the mesoscale fraction. A double peak is found in all cases. The lower one at $0.2z_i$ and an upper one at $0.8-0.9z_i$, both with approximately equal magnitude. Thus, the peak locations coincide with the variance profiles of the fluctuations $\widetilde{\overline{u}}'$ and $\widetilde{\overline{v}}'$ (Fig. 4.11) in consideration of the variance of $\widetilde{\overline{w}}'$, which is close to 0 near the surface and the top of the boundary layer. The peaks reflect the horizontal compensational branches of the SC. The vertical up- and downdrafts are the dominant features in the middle of the boundary layer, causing a decrease of the Reynolds stress. Since the SC suffers from wind-shear, this decrease vanishes with increasing background wind (case B1306). The mesoscale fraction shows contributions of the total flux at the lower peak between 10 % and 18 % (B1306 - B3005) and 19 % and 43 % at the upper peak. Compared to the HCR, the total Reynolds stress benefits from the heterogeneity within the entire boundary layer in case B3005 (about 0.005 $\mathrm{m^2/s^2}$). The little enhanced flux in case B1306 should not be overrated. In B1706, the Reynolds stress is higher near the surface but smaller near the top of the boundary layer, but the sum of the differences appear to cancel each other out.

Mesoscale contribution in the course of the day

In order to study the temporal evolution of the mesoscale contribution, integral values of the flux profiles were carried out at different times in the course of day. A mesoscale flux $\mathcal{F}$ which is representative for the entire boundary layer can be calculated by the height-averaged value of the flux $\overline{\widetilde{w}'\widetilde{\Phi}'}(z)$ as follows:

$$\mathcal{F}_{\overline{w'\Phi'}} = \frac{1}{N}\sum_{z=0}^{1.4z_i} |\overline{\widetilde{w}'\widetilde{\Phi}'}(z)| \quad , \tag{4.20}$$

where N is the number of layers over that averaging is done. The percental contribution to the total flux $\mathcal{G}$ can be obtained by $\mathcal{F}_{\overline{w'\Phi'}}$, divided by the sum of the absolute value of all flux components:

$$\mathcal{G}_{\overline{w'\Phi'}} = \frac{\sum_{z=0}^{1.4z_i} |\overline{\widetilde{w}'\widetilde{\Phi}'}(z)|}{\sum_{z=0}^{1.4z_i} \left[|\overline{w}\overline{\Phi}(z)| + |\overline{\widetilde{w}'\widetilde{\Phi}'}(z)| + |\overline{w''\Phi''}(z)| \right]} \quad . \tag{4.21}$$

These definitions differ slightly from Uhlenbrock (2006) to account for negative fluxes. The global fraction $\overline{w}\overline{\Phi}$ is equal to 0. The results are shown as time series in Figs. 4.29 and 4.30. The values at 13 UTC relate to the shown profiles above (Fig. 4.29 (a)). The absolute contribution to $\overline{w'\theta'}$ is characterized by the diurnal cycle of the surface heat flux as well as a dependency on the SC strength. By comparing the peaks a lag of ~ 1 h to the respective surface forcing can be identified (see Fig. 4.4 (a)), giving evidence that the atmosphere needs this time to transfer the forcing signal to the SC. The maximum contribution is in the range of 4 % (B1306) and 18 $\mathrm{W/m^2}$ in case B3005. $\mathcal{F}_{\overline{w'q'}}$ shows different features (Figs. 4.29 (b)). A diurnal cycle is only marginally developed and a correlation to the strength of the SC is hardly detectable. The total contribution is much higher than $\mathcal{F}_{\overline{w'\theta'}}$ (maximum values: $50-175$ $\mathrm{W/m^2}$) and not directly coupled to the surface forcing by $\overline{w'q'}_0$ (see Fig. 4.4 (b)). In

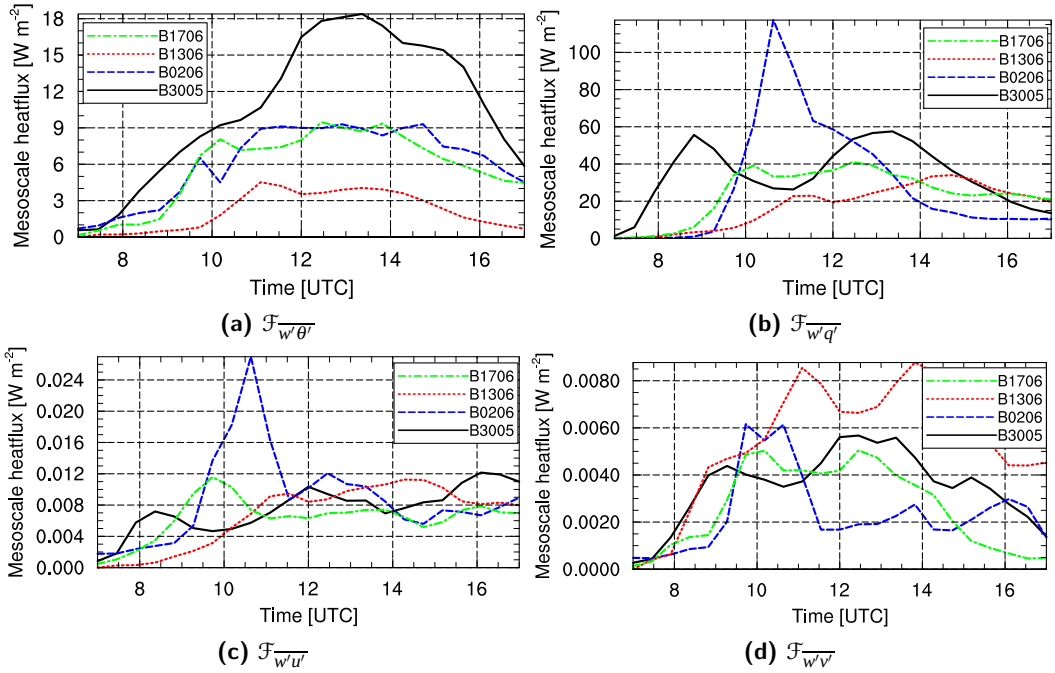

Figure 4.29: Timeseries of the absolute contribution of mesoscale vertical fluxes from $6-17$ UTC, calculated every 30 min after Eq. 4.20 as moving average (1 h).

contrast to Uhlenbrock (2006), case B3005 was not found to exhibit the smallest values of $\mathcal{F}_{\overline{w'q'}}$, which might be related to the additional border area. Furthermore a distinct peak is observed at $10:40$ UTC (B0206). Uhlenbrock (2006) showed the same peak and suggested that it would be caused by evaporated water-vapor which was released over the forest patches, where strong SCs occured. Since both, $\mathcal{F}_{\overline{w'u'}}$ and $\mathcal{F}_{\overline{w'v'}}$ exhibit this peak as well, it is assumed, that it is related to the fast growth of the boundary layer which occured between 9 UTC and 10 UTC from a depth of 600 m to 2400 m owing to dissipation of higher inversions (see Fig. 4.29 (c) - (d) and Fig. 4.6 (a)). Due to the persistent inversion in the morning and a redisual layer above, vertical fluxes are suppressed (cf. section 4.2.4). As soon as the inversion vanishes, humidity as well as momentum can be transported vertically. The process benefits from the quasi-neutral stratification of the residual layer above the inversion to a great extent, leading to the high flux peak. It will also be shown that this peak is not a feature of the mesoscale contribution, but of the total vertical flux and thus not of major interest in the scope of this study. The momentum flux contributions shall not be analyzed further but it should be mentioned, that the maximum contribution $\mathcal{F}_{\overline{w'u'}}$ is in general about twice as high (typical values $\sim 0.008\ \mathrm{m^2/s^2}$) as $\mathcal{F}_{\overline{w'v'}}$ (typical values $\sim 0.004\ \mathrm{m^2/s^2}$).

The normalized series in Fig. 4.30 give percental contribution and are more meaningful, because they relate the mesoscale to the total flux and are able to filter effects of the diurnal cycle. $\mathcal{G}_{\overline{w'\theta'}}$ clearly shows, that the percentage of the contribution is depending on the SC strength as it was expected. The contribution is slighty increasing in time in case B3005 and approximately constant otherwise. Typical values at about 13 UTC between 4 % and 18 % can be obtained. In the later afternoon (after 16 UTC), the mesoscale fraction rises significantly (in case B1306 the SC seem to be too weak to show this increase). It can be traced back to the fact that the surface forcing has vanished to a great extent. The small-scale turbulence is sensitive to changes of the surface forcing and thus dissipates rapidly when the forcing dimishes. In contrast to small-scale turbulence, the SC takes about 1 h to transfer the surface forcing into turbulent transport and therefore is able to persist longer, resulting in a shift of the contribution

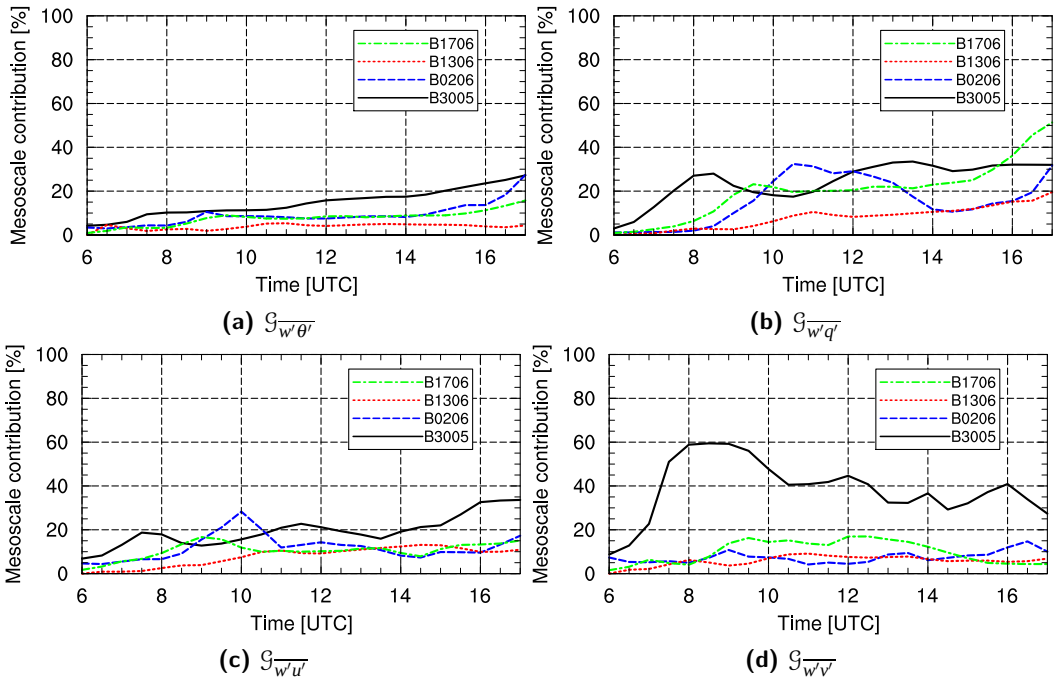

Figure 4.30: Timeseries of the percental contribution of mesoscale vertical fluxes from $6-17$ UTC, calculated every 30 min after Eq. 4.21 as moving average (1 h).

to the total flux.

$\mathcal{G}_{\overline{w'q'}}$ displays a similar behavior as $\mathcal{G}_{\overline{w'\theta'}}$, but holds more fluctuations due to water-vapor release events in the course of day which leads to the result that the SC strength cannot be linked clearly to the mesoscale contribution. Anyway, B3005 tends to reach higher values than the other cases and B1306 cleary displays the smallest contribution. This result is contrary to Uhlenbrock (2006), who suggested no dependency of $\mathcal{G}_{\overline{w'q'}}$ on the SC strength. The results of the present study contrariwise suggest the latent heat flux contribution to be a combination of the SC strength and the available water-vapor at the surface. The values at 13 UTC vary between 10 % (B1306) and 32 % (B3005). It is also noteworthy that the discussed peak at $10:40$ UTC has disappeared in all time series due to the normalization of the total flux.

The momentum fluxes shall be discussed only briefly here, since the two components are dependent on the mean wind direction which was varying for the four simulations and therefore a comparison is not reasonable. In general, the contributions $\mathcal{G}_{\overline{w'u'}}$ and $\mathcal{G}_{\overline{w'v'}}$ exhibit values up to 20 %, a typical contribution of 10 % and are relatively constant in the course of day. Case B3005 appears to yield higher contributions, especially with a view to $\mathcal{G}_{\overline{w'v'}}$, where the contribution is more than twice as high (~ 40 %) as for the other cases. The reason for this might be originated from the weak background wind, which allows the SC to develop freely in both lateral directions, while the small-scale turbulence is more affected by the background wind and the development of turbulent structures in directions perpendicular to the mean wind (here 90 ° east) is suppressed.

Conclusions

From the results above which are in agreement with the findings from section 4.2.4, there is evidence to suggest that entrainment at the top of the boundary layer due to small-scale turbulence is more effective than due to mesoscale turbulent structures. On the one hand, the

vertical heat flux is found not to be influenced by the SC in the boundary layer. Therefore the vertical transport of heat is partially taken over by the SC. On the other hand, the latent heat flux is enhanced under certain conditions in the presence of the SC. The reasons for this enhancement remain unclear. The Reynolds stress benefits from the presence of the SC, depending on the strength of the circulation. For this reason it can be concluded, that the vertical transport of momentum by the SC is more efficient than by small-scale turbulence.

The percentage of the mesoscale contributions $\mathcal{G}_{\overline{w'\theta'}}$ and $\mathcal{G}_{\overline{w'q'}}$ are found to be higher than respective calculations of Uhlenbrock (2006). The mesoscale contribution $\mathcal{G}_{\overline{w'q'}}$ shows a dependency on the SC strength. It leads to the suggestion that the heterogeneity induced humidity $\widetilde{q'}$ is transported to a great extent by the SC. Both findings were disputed by the study of Uhlenbrock (2006). However, the general finding, that the mesoscale fraction contains a significant amount of the total flux, which is smaller than the values of $50-80$ % from idealized studies (e.g. Chen and Avissar, 1994a; Lynn et al., 1995; Patton et al., 2005), still holds for the results of this study. The suggestion of Kang and Davis (2008), that the mesoscale fluxes are negligible in comparison to the turbulent portion can thus not be approved.

By the knowledge of the author, the quantitative effect of heterogeneity induced vertical momentum fluxes has not been investigated so far. The present study shows that the total momentum flux, represented by the Reynolds stress, is enhanced commensurably to the SC strength.

4.3 Correlations between secondary circulations and surface heterogeneities

This section forms a main part of the present study and attempts to identify relations between the structure of SCs and surface heterogeneities. The study is based on the fundamental hypothesis that the position and strength of the circulation, represented by the vertical velocity component, is correlated with the underlying and the upstream sensible surface heat flux. Updrafts are expected to develop over locations that provide a higher surface heat flux than the environment. In sections 4.1 and 4.2, the development of roll convection was a significant feature of simulation cases with a geostrophic wind velocity $\geq 4\ \mathrm{m/s}$, while for a wind of 2 m/s, the SC structure was primarily characterized by local structures. It is assumed that in the former cases, the flow is affected by a "smeared" surface heat flux (advection effect) and rolls are forming oriented to the mean wind. The latter case suggests that the effect of advection is weak for low wind speeds of the same magnitude as turbulent velocities and the position of the circulation therefore is mainly dependent on the local underlying surface heat flux. This hypothesis would be in agreement with the LES study of Gryschka et al. (2008), where sea-ice inhomogeneities led to the development of rolls during an cold-air outbreak. They found that SCs originate at sea-ice leads, represented by surface heat flux distributions in the marginal ice zone, which force roll convection over the open sea in the presence of a strong background wind.

For proving this hypothesis, a correlation analysis is used, suggesting that the bulk of the SC might be explainable by a linear correlation between sensible surface heat flux and vertical velocity for mean winds $\geq 4\ \mathrm{m/s}$. Of course, the effects of local surface heterogeneities are still relevant and might decrease the correlation coefficient.

In the first part of this study, the simulations from the previous sensitivity study were used for calculating correlations, because of the constant forcing by surface heat fluxes. Therefore, a streamwise averaging of the heat fluxes was feasable for huge distances up to $130\ \mathrm{km}$ (see section 4.3.1). Furthermore, correlations between the heterogeneity and the mesoscale humidity

and the local boundary layer were investigated.

In the second part (section 4.3.2), based on the results of section 4.3.1, the correlation analysis will be applied to a selected simulation case for the "Golden Days" of section 4.2, including a discussion about the applicability to real synoptic conditions.

Correlation analysis method

Owing to the complexity of the analysis, resulting terms of comprehension as well as the quality of the analysis results, the basic method applied to the simulation data, shall be explained briefly in advance.

The correlation can be measured as cross-correlation coefficient ρ, defined as

$$\rho_{\Phi,\Psi} = \frac{1}{N-1} \cdot \frac{\sum_{i=1}^{N} \left(\Phi_i - \overline{\Phi}\right)\left(\Psi_i - \overline{\Psi}\right)}{\sigma_\Phi \cdot \sigma_\Psi} \tag{4.22}$$

for given sequences of N elements $(\Phi_1, \Phi_2, \ldots \Phi_N)$, $(\Psi_1, \Psi_2, \ldots \Psi_N)$ for two quantities Φ, Ψ with their respective standard deviations σ_Φ and σ_Ψ. The values of ρ are in the range of $[-1, 1]$, where 1 is a perfect positive linear correlation and -1 stands for perfect negative linear correlation (also called anti-correlation). A value of 0 corresponds to independence (linear). The interpretation of the correlation coefficient is arbitrary, depending on the context and does not exclude higher order correlations. For this study, Tab. 4.5 is used for interpretation. ρ is used to calculate the cross-correlation between the sensible surface heat flux $\overline{w'\theta_0'}$ and the ensemble-averaged vertical velocity $\widetilde{w'}$ at height level $z = 0.4\ z_i$, where the secondary circulation was strongest. Both, $\widetilde{w'}$ and $\overline{w'\theta_0'}$ were averaged along the rolls, i.e. streamwise-averaged. Due to the fact that the mean wind at $0.4\ z_i$ was not parallel to any numerical grid axis, the averaging process required a coordinate transformation, i.e. a rotation, of the fields to achieve an orientation parallel to the grid axes. This was realized by a rotation and a following two-dimensional interpolation using an inverse distance weighting method after Shepard (1968). The mean wind was calculated as the spatial average of the horizontal velocity components u and v at $0.4\ z_i$.

Correlation	Negative	Positive
Small	-0.39 to -0.1	0.1 to 0.39
Medium	-0.59 to -0.4	0.4 to 0.59
Large	-1.0 to -0.6	0.6 to 1.0

Table 4.5: Interpretation of the correlation coefficient

It was necessary to extend the area in the upstream direction to include the full path an air parcel covers during the simulation time, because the rotated fields do not exhibit cyclic boundaries. Nevertheless, the fields used for streamwise averaging contain artifacts of the cyclic boundaries of the original fields. Depending on the geostrophic wind and the chosen border area, structures are repeating themselves several times within the rotated extended fields. The surface heat flux displays distinct discontinuities because the land use classes are not continuous. These discontinuities are expected to act as (non-realistic) surface heterogeneities as already mentioned in section 4.1. The vertical velocity component does of course not show any discontinuity due to continuity reasons. Though these artifacts could be avoided by extending the border area to

the values mentioned above, this would imply an enormous rise of computational costs, which is not applicable.

However, the border area sensitivity study clearly showed, that the effect of these artifacts is only small for the analysis in the LFA with a sufficient border area ≤ 22 km, depending on the wind speed, thus a further extension is not worthwhile.

4.3.1 Correlation study for a case with constant surface fluxes

The correlation analysis method was applied to the border area study cases with geostrophic wind velocities of $v_g = 4$ m/s and, particularly, 6 m/s with different border areas from 6 km up to 22 km. For the cases with $v_g = 2$ m/s, this analysis was not carried out, because rolls did not occur and therefore a streamwise averaging would not make any sense. Different border areas were chosen, in spite of the results of section 4.1, to show some features that can influence the correlation decisively. The averaging distance was chosen according to the geostrophic wind. For cases with $v_g = 6$ m/s and a simulation time of 6 h, a parcel of air passes and thus can be affected by ~ 130 km of surface area (~ 80 km for 4 m/s and ~ 45 km for 2 m/s, respectively). Below, the detailed analysis is presented for cases $v_g = 6$ m/s (with distinct roll convection), while for $v_g = 4$ m/s only the resulting correlations shall be discussed briefly.

All fields used in this section are averaged over 1 h after 6 h of simulation time.

Streamwise-averaged correlations

With $v_g = 6$ m/s and a simulation time of 6 h, a parcel of air covers a distance of 129.6 km. The calculation of the correlation was done for different angles in relation to the mean wind direction. The angle varied in this study between -90 ° and 90 ° with a step-size of 5 °. This was done for the reason that a single correlation value might be at random, and is, especially for values in the range of $0.3 - 0.59$, difficult to assess. The variation of the rotation angle might be able to clarify the randomness and the relevance of those values.

Fig. 4.31 shows xy-cross-sections of the rotated and extended sensible surface heat flux field of this area ((a), (c) and (e)) and the appropriate vertical velocity at $z = 0.4\, z_i$ ((b), (d) and (f)) for the simulations A066, A146 and A226 with a rotation angle of 0 °. The fields are orientied to the mean wind which is blowing from the right side. The xy-cross-sections of the surface heat flux with a range of $0 - 500$ Wm^{-2} show repeating structures like Lake Scharmützel, where the lowest values (blue) can be found, or larger forest patches, represented by higher values (red). The discontinuities of the cyclic boundaries are more or less of good visibility for all cases and are dependent on the corresponding border area. Certainly, there are less discontinuity boundaries and thus comparatively less repeating structures in case A226 owing to the large border area.

A first look at the correlations (Fig. 4.32, plotted against rotation angle) displays a well-defined peak at 0 ° for all cases, except A064, with at least medium correlations ≥ 0.4. It ensures that the correlation is not random, though there are other peaks of the same magnitude for border areas < 14 km. This already confirms the results of the border area sensitivity study, which was displaying the shortcomings of small border areas, but can be more specified in connection with the vertical velocity. On the one hand, a border area of 6 km allows the development of rolls of limited length with reference to the model domain size, which was 28 km $\times$ 32 km in this case, thus a maximum roll length < 40 km (Fig. 4.31 (b)) in the rotated field is obtained. This can result in a reduced range of the vertical velocity (averaged over 129.6 km, which is about three times as long as the maximum roll length). The range for case A066 is ~ 0.3 m/s, while cases A146 and A226 gain higher ranges of 0.5 m/s and 0.8 m/s,

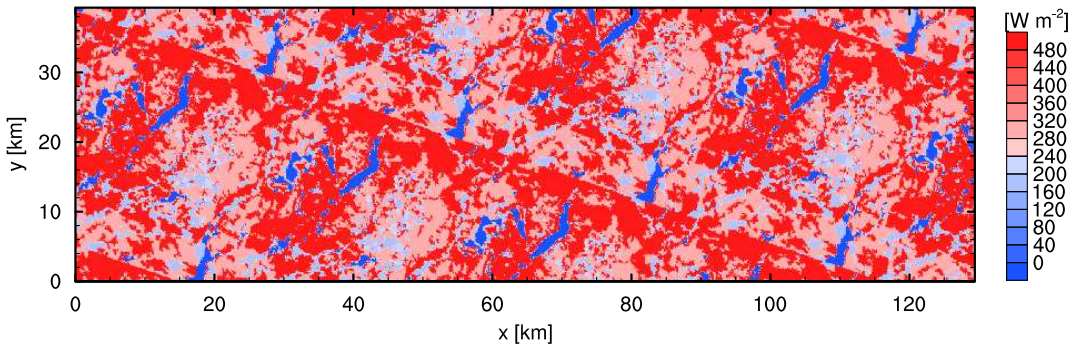

(a) A066, $\overline{w'\theta'_0}$

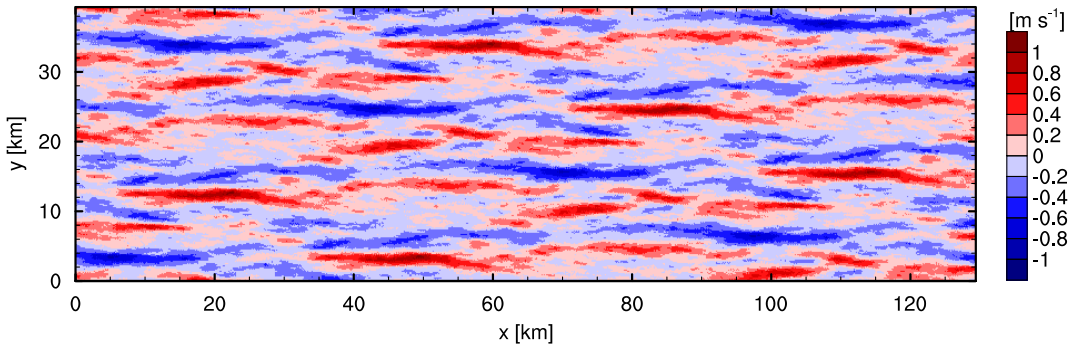

(b) A066, $\widetilde{w}$

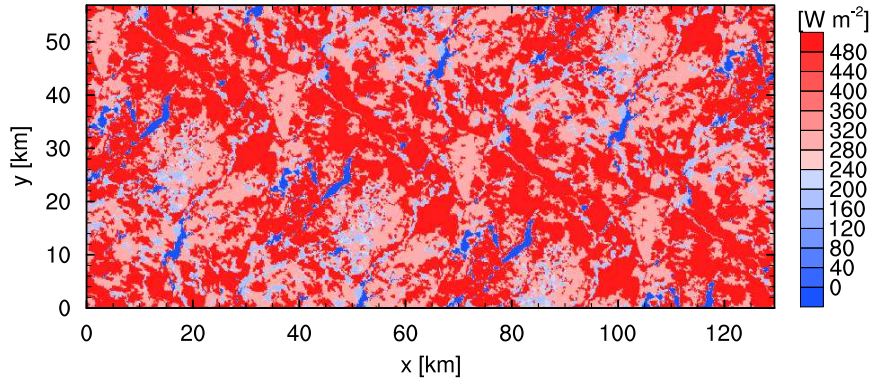

(c) A146, $\overline{w'\theta'_0}$

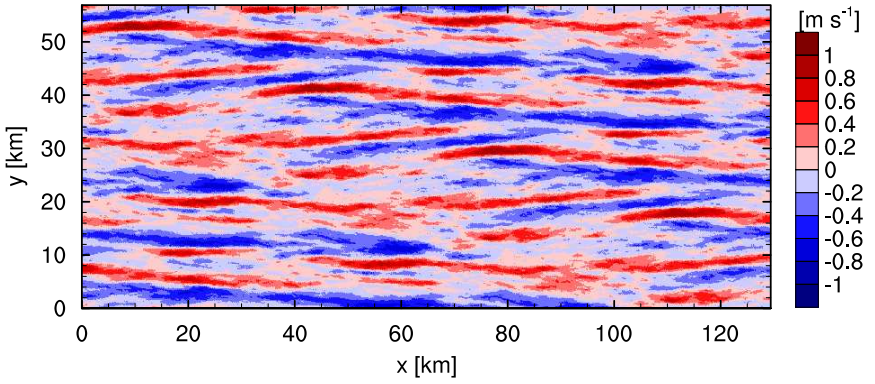

(d) A146, $\widetilde{w}$

Figure 4.31: xy-cross-sections of the rotated and extended fields of the sensible surface heat flux (a, c) and the ensemble-averaged vertical velocity at $z = 0.4\ z_i$ (b, d) after 6h of simulation time, averaged over 1h (part I).

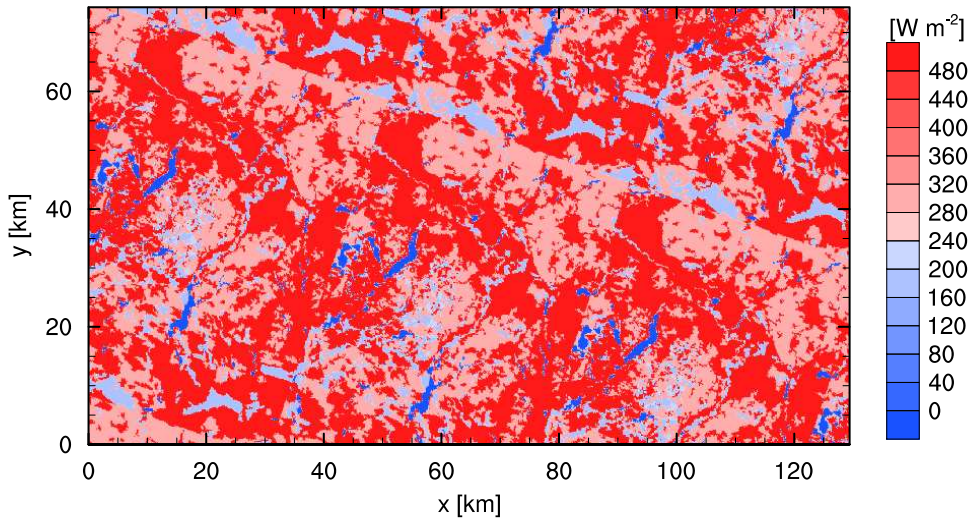

(e) A226, $\overline{w'\theta_0'}$

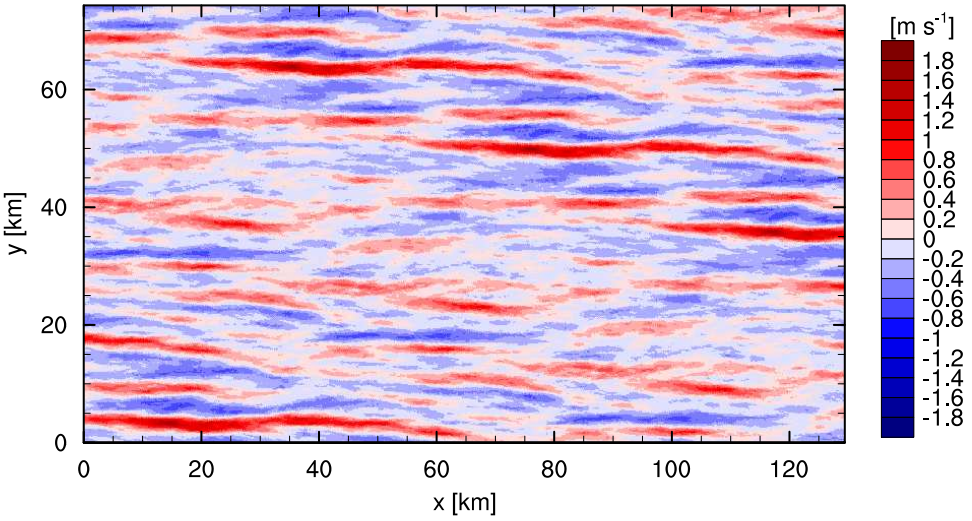

(f) A226, $\widetilde{w}$

Figure 4.31: xy-cross-sections of the rotated and extended fields of the sensible surface heat flux (e) and the ensemble-averaged vertical velocity at $z = 0.4\ z_i$ (f) after 6h of simulation time, averaged over 1h (part II).

respectively (Fig. 4.33). A smaller range is the equivalent of a weaker SC signal. On the other hand, the according range of the streamwise-averaged sensible surface heat flux is increasing with an increasing border area as well. An enhanced range, following the hypothesis, should lead to a strengthened SC. But as can be seen in Fig. 4.33, though the range changes slightly from ~ 50 Wm^{-2} (case A066, Fig. 4.33 (a)) to ~ 55 Wm^{-2} (case A226, Fig. 4.33 (b)), it is leading to a significant change in the correlation (Fig. 4.32 (b)). Therefore the secondary peaks mentioned above are assumened to be at random, while the primary peak at $0\,^{\circ}$ can be treated as the desired correlation. However, the correlations for small border areas have to be interpreted carefully and finally support the choice of a large border area.

In general, the correlation coefficient at $0\,^{\circ}$ displays the feature to become higher with increasing area size (Fig. 4.32). For all cases with a border area ≥ 14 km, the correlation is large and achieves values of 0.6 or even higher. This might be owing to the extended surface area, which is leading to a change in the circulation pattern and strength as well as the elongated rolls, which are able to enhance the averaging conditions. It should be considered that roll structures might be eliminated during the averaging process anyhow and have a negative impact on the correlation.

As can be seen in Fig. 4.31 (b), (d) and (f), the circulation pattern does not necessarely have to be aligned perfectly to the mean wind. This can reduce the correlation as well and is arisen from a local effect of the heterogeneity on the boundary layer turbulence and the fact that the mean wind is only a horizontally averaged value.

The location of the discontinuities in the circulation structure is distinguishable e.g. in Fig. 4.31 (d) and shows some interesting characteristics. Strong circulation rolls are visible and repeating themselves along the virtual line from $(x,y) = (11\ \mathrm{km}, 57\ \mathrm{km})$ to $(129.6\ \mathrm{km}, 14\ \mathrm{km})$ and whose axes are more or less oriented to the mean wind (blowing from the right side). South-westbound of this patch, the circulation weakens considerably. This feature is present in all simulation cases and finds its cause in the underlying surface heterogeneity. The virtual line is equivalent to the borderline of model domain (cf. Fig. 4.31 (c)). The north-eastbound region of the borderline is characterized by striking heterogeneities, contrary to the south-westbound region, which shows a much more homogeneous surface distribution. The former is supposed to cause the strong circulation pattern, located further downstream due to advection, while the latter is responsible for the weakening of this pattern due to relatively homogeneous heating. It nicely shows the effect of advection on the circulation and again constitutes the importance of a sufficient border area. Furthermore, it indicates that the fetch of advection should be taken into account to obtain even higher correlations. It also shows that the (statistical) SCs in this study do not propagate over large homogeneously (strong) heated surface regions.

The only exceptional case is A064, where no well-defined peak appeared at $0\,^{\circ}$. The causes for this behavior were not studied any further, but the shortcomings were already discussed and shall be recapitulated here. On the one hand, a border area of 6 km was already stated as inadequate for the analysis. On the other hand, the main objective was to identify correlation for cases with a remarkable development of roll-like structures, which was particularly the case in the simulations with $v_g = 6$ m/s. However, correlations for simulation cases with $v_g = 4$ m/s were presented for the sake of completeness in this section and display large correlations for sufficient border areas as well (Fig. 4.32 (a)).

Fetch study

The previous section used streamwise-averaged data for the calculation of correlations. The fields were extended to the distance a parcel of air covers during the simulation time of 6 h in

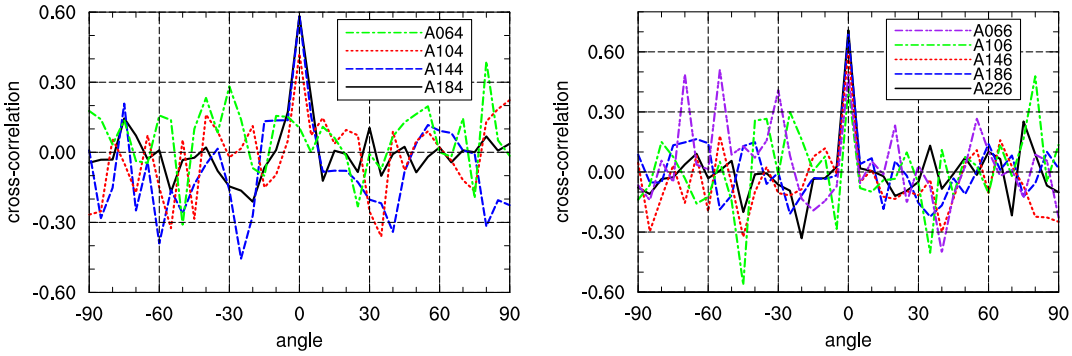

(a) $v_g = 4$ m/s (b) $v_g = 6$ m/s

Figure 4.32: Cross-correlation against rotation angle regarding the orientation to the mean wind for different simulation cases.

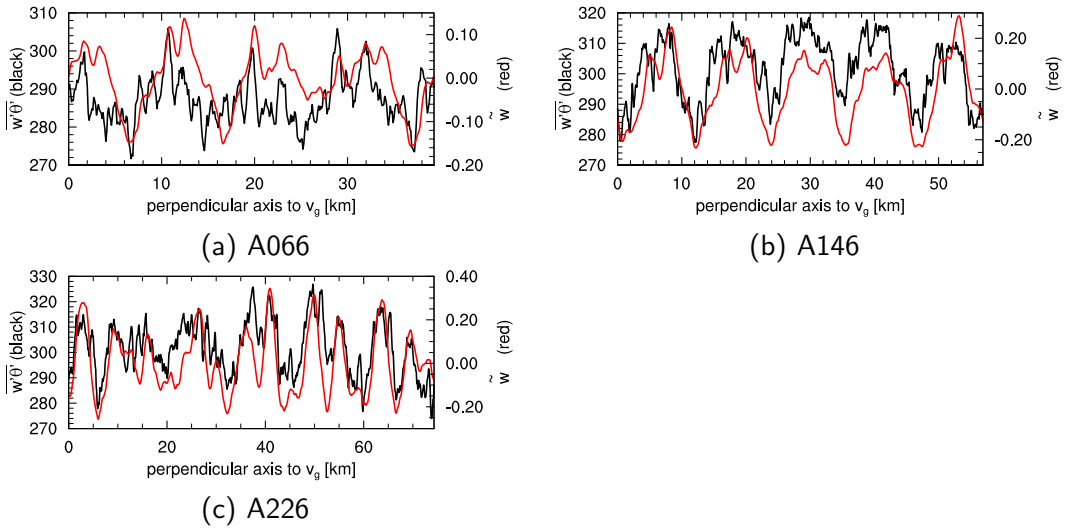

(a) A066 (b) A146

(c) A226

Figure 4.33: Streamwise-averaged sensible surface heat flux (black) and vertical velocity (red) for different simulation cases.

the presence of a background wind, since this is exactly the distance, a parcel is affected by the underlying surface properties. Despite the good results in the previous sections, an implicit assumption was made, that is actually questionable. The correlation analysis could not take into account that the effect of advection on the circulation is usually dependent on the upstream fetch length and thus is assuming an equal contribution by the entire upstream region.

The hypothesis can be expanded, presuming a distinct fetch length of the sensible surface heat flux depending on the wind speed that is affecting the circulation. This would be able to explain, that rolls develop for high wind speeds of $v_g = 6$ m/s, because the flow "sees" a smeared (moving average) surface heat flux of a larger fetch, while for low wind speed, this fetch is short and therefore providing short heat flux patches. The averaging over shorter distances would lead to higher deviations and cause stronger circulations that do not show roll-like structures. For this reason, this section tries to specify a fetch length depending on the wind speed.

The calculation of correlations was modified to achieve this objective and is based on the rotated fields of $\widetilde{w}$ at height level $z = 0.4\ z_i$ and $\overline{w'\theta_0'}$. However, the former was not extended, while the latter was extended according to the calculation method. The correlation coefficient $\rho(x_i, \Delta_f x)$ was calculated for the slices at $x = x_i$ of the vertical velocity in y-direction and the, over distance $\Delta_f x$ averaged, sensible surface heat flux fetch of the upstream region $[x_i, x_i + \Delta_f x]$ starting at x_i. ρ was calculated for different fetches $\Delta_f x$ and averaged over all slices x_i. In a few words, this method is calculating the correlation of a slice of $\widetilde{w}$ perdendicular to the mean wind and the upstream fetch of $\overline{w'\theta_0'}$. This was done for slices in the entire (not extended) model domain for fetches of $\Delta_f x = 1$ km to x_{max} and can also be written as:

$$\overline{\rho}(\Delta_f x) = \frac{1}{N/2} \sum_{i=0}^{N/2} \rho(x_{2i+1}, \Delta_f x) \quad \forall \quad \Delta_f x = 1, 2, \ldots, x_{max} \quad , \tag{4.23}$$

where the correlation was calculated for every second slice (every second slice was chosen to save computational resources). x_{max} is the maximum possible fetch length, depending on the wind speed ($x_{max} = 100$ km for $v_g = 6$ m/s was found to be sufficient) of the previous study and N is the number of grid points in x-direction. $\overline{\rho}(\Delta_f x)$ is the resulting mean correlation dependent on the fetch $\Delta_f x$.

With this method it was possible to estimate the upstream fetch for different simulation cases, even for the weak wind case. Fig. 4.34 shows the averaged cross-correlation $\overline{\rho}$ against the fetch $\Delta_f x$. For a border area of 18 km, the maximum correlation varies between 0.23 and 0.31. Though the correlation is small in all cases, a global maximum exists at $\Delta_f x = 5$ km for $v_g = 2$ m/s, $\Delta_f x = 19$ km for $v_g = 4$ m/s and $\Delta_f x = 35$ km for $v_g = 6$ m/s and the figures show right-skewed shapes. The correlation is at first increasing rapidly with increasing $\Delta_f x$, then converging to the maximum, followed by a monoton decrease. It clearly points out that the influence of the upstream surface heat flux is decreasing with distance to the reference slice, owing to the effect of advection. As expected, the maxima are shifted to larger fetches for higher geostrophic winds. The relatively small correlations might be owing to the fact that the vertical velocity at one point is depending on the nearby circulation structure and above all, the calculation used a smoothed and averaged surface heat flux which affects the correlation on a markable level when comparing to a single slice of the vertical velocity. Furthermore, it is possible that the direct underlying (and somewhat upstream) surface properties are not effecting the local circulation due to advection. This would reduce the correlation as well. For the present fetch study, the absolute value of the correlation is of minor interest compared to the location of the maximum.

It should be mentioned that the fetch is also dependent on the heterogeneity itself. The gap between the simulations with the border area 10 km and 14 km, as discussed sufficiently in

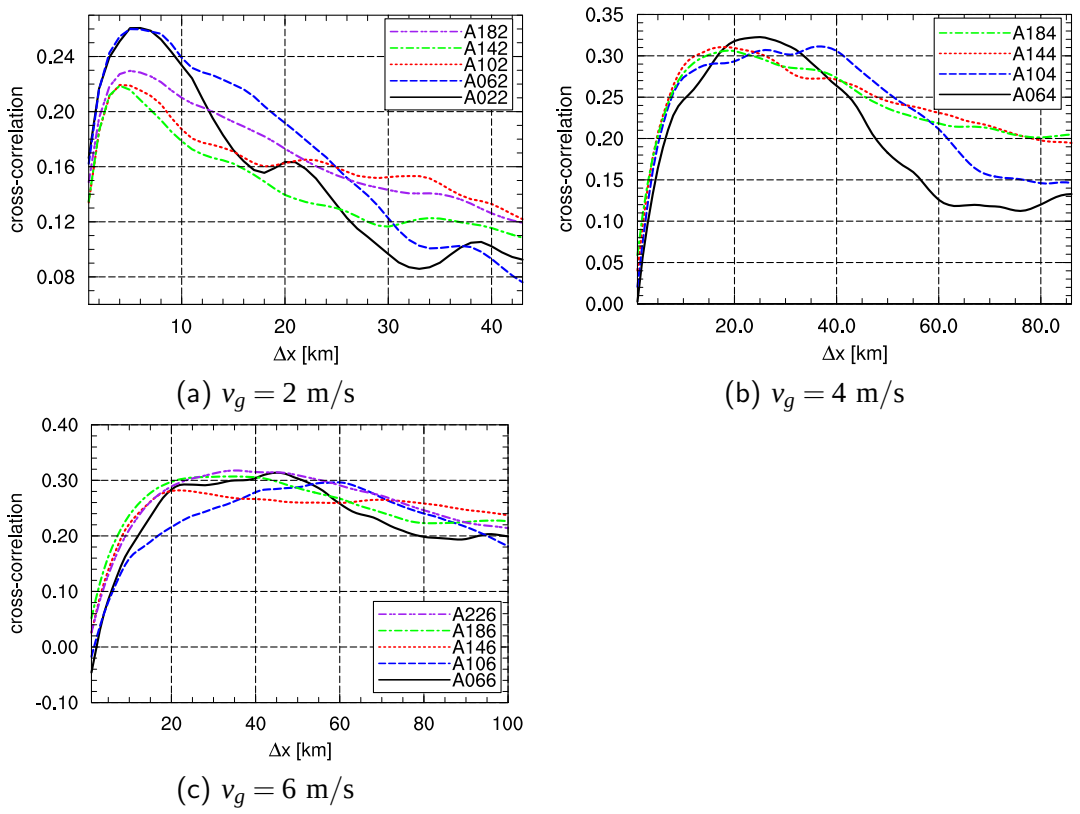

(a) $v_g = 2$ m/s (b) $v_g = 4$ m/s

(c) $v_g = 6$ m/s

Figure 4.34: Averaged cross-correlations against fetch $\Delta_f x$, calculated according to Eq. 4.23.

section 4.1, is leading to modified locations of the maxima for simulations with $v_g = 4-6$ m/s. The more or less fixed length of the fetch in case of $v_g = 2$ m/s ($\Delta_f x \approx 5$ km) reveals that the gap is not affecting the flow, because the fetch is smaller than the border area.

In regard to the purpose to performing simulations with best possible realistic results, the fetch analysis suggests to add at least the length of the fetch as upstream border area. With this fact in mind, the border area of 22 km for $v_g = 6$ m/s in comparison with the fetch length $\Delta_f x = 35$ km might be called into question. With reference to the border area study, the chosen border area of 22 km can still be seen as adequate for geostrophic wind velocities of 6 m/s, since most of the relevant fetch is covered (Fig. 4.34 (c)). For lower wind speeds, the chosen border area has roughly the same size as the fetch.

As a conclusion for the correlation analysis, larger correlations could be obtained by shortening the averaging distance of the surface heat flux to the analysis domain plus fetch area. This was also proved by calculating correlations and varying the averaging distance (not shown).

With knowledge of the fetch length, an "effective surface heat flux" could be calculated and compared to the circulation pattern. This was realized by averaging $\overline{w'\theta'_0}$ over the fetch length:

$$\overline{w'\theta'_0}_{eff}(i,j) = \frac{1}{\Delta_f x} \sum_{k=0}^{\Delta_f x - 1} \overline{w'\theta'_0}(i+k,j) \tag{4.24}$$

for all horizontal grid points i, j of the model domain. The result is a modified surface heat flux field (Fig. 4.35 (a), (c), (e)) that should be able to predict the development of circulation structures to a high degree.

When comparing $\overline{w'\theta'_0}_{eff}$ to the circulation pattern (Fig. 4.35 (b), (d), (f)) for the different

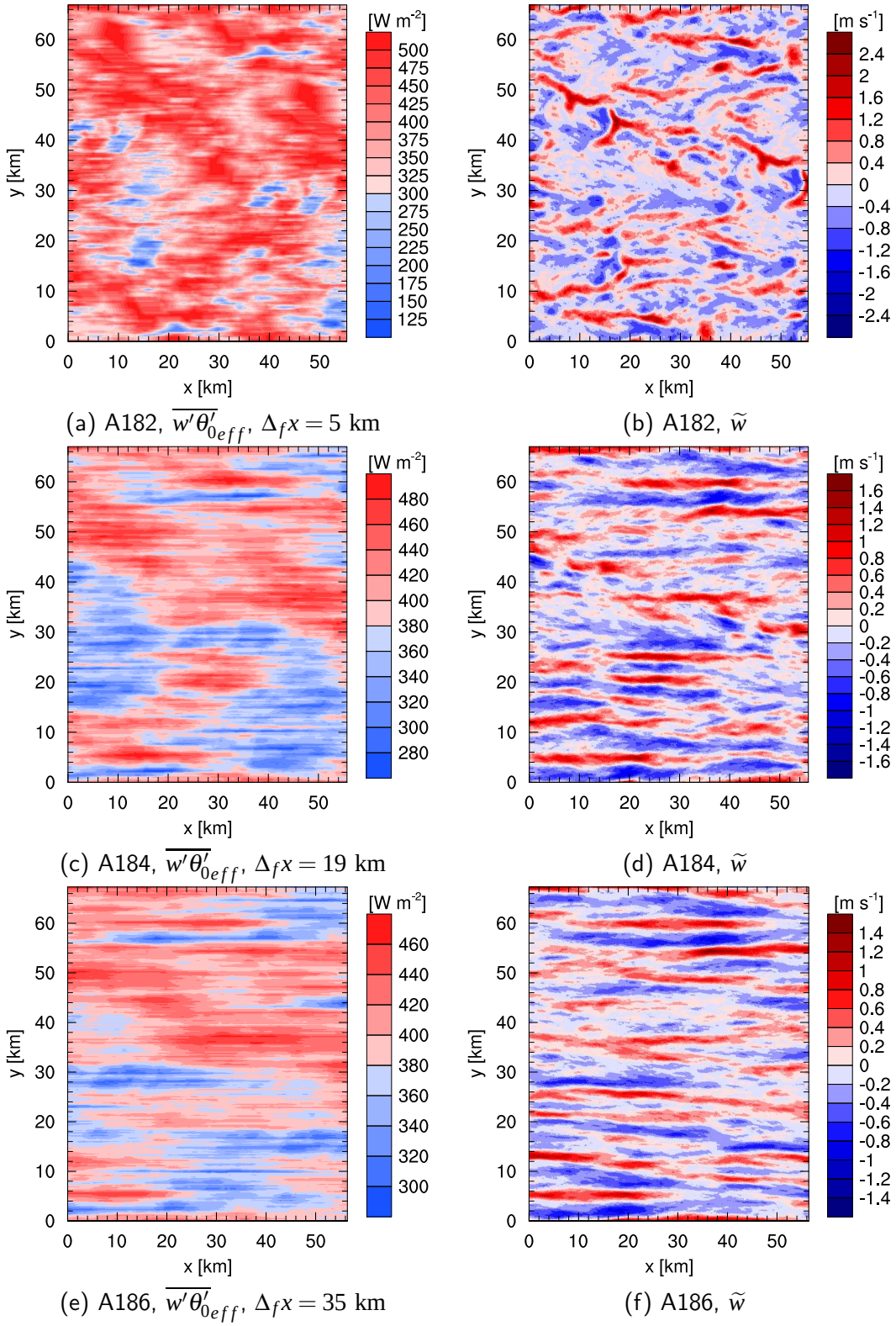

(a) A182, $\overline{w'\theta'_{0_{eff}}}$, $\Delta_f x = 5$ km

(b) A182, $\widetilde{w}$

(c) A184, $\overline{w'\theta'_{0_{eff}}}$, $\Delta_f x = 19$ km

(d) A184, $\widetilde{w}$

(e) A186, $\overline{w'\theta'_{0_{eff}}}$, $\Delta_f x = 35$ km

(f) A186, $\widetilde{w}$

Figure 4.35: xy-cross-section of the effective sensible surface heat flux (left) and the ensemble-averaged vertical velocity at $z = 0.4\ z_i$ (right) for simulation cases with a border area of 18 km.

geostrophic wind speeds, one has to consider that not absolute high or low heat fluxes lead to circulation structures, but rather the spatial gradient. For high wind speeds ≥ 4 m/s this is equivalent to the spatial variation in y-direction. Fig. 4.35 nicely shows, that with knowledge of the fetch length, it is possible to estimate the circulation structure with the aid of $\overline{w'\theta'_{0}}_{eff}$. This shall be explained using the example of simulation A186. Strong roll pairs appear from $y = 52$ km to 62 km (Fig. 4.35 (f)). Corresponding pairs of high and low surface heat fluxes, thus high spatial variations, are of good visibility (Fig. 4.35 (e)). This does also apply to the rolls from $y = 0$ km to 12 km. On closer examination of the rest of the circulation pattern, the assumption fits very well. While for case A184, this assumption is also easy to show, the circulation pattern of simulation A182 offers more complex structures that are difficult to link to $\overline{w'\theta'_{0}}_{eff}$. This is due to the weak wind, which is reducing the effect of advection. This also explains the small correlation of the fetch maximum (Fig. 4.34 (a)).

Further correlations

High correlation coefficient values $\rho_{\overline{w'\theta'_0},\widetilde{w}}$ were already shown. By reason of the characteristics of humidity and the local boundary layer height were studied in section 4.2.4, the question rises, whether further possible correlations (or inexistent correlations) between the heterogeneity and mesoscale induced quantities might be detectable by the analysis method. Thus, the correlation coefficients $\rho_{\overline{w'q'_0},\widetilde{q'}}$,$\rho_{\overline{w'\theta'_0},\widetilde{\theta'}}$ and $\rho_{\overline{w'\theta'_0},\widetilde{z_i}}$ shall be part of this section, too. In the following, the presented analysis method will be applied to the simulation B1306. A comparison is carried out using results from the idealized case A186, because both simulations have equal border areas (18 km) and background winds (6 m/s). Due to the fact that issues like randomness and applicability were discussed at full length for $\rho_{\overline{w'\theta'_0},\widetilde{w}}$, it appears to be sufficient to discuss obtained correlation values for a single simulation case at rotation angle 0 ° only.

Correlation	Height			
		$0.1 \cdot z_i$	$0.4 \cdot z_i$	$1.0 \cdot z_i$
$\rho_{\overline{w'q'_0},\widetilde{q'}}$	-	0.10	-0.12	-0.52
$\rho_{\overline{w'\theta'_0},\widetilde{\theta'}}$	-	0.70	0.41	-0.50
$\rho_{\overline{w'\theta'_0},\widetilde{w}}$	-	-	0.69	-
$\rho_{\overline{w'\theta'_0},\widetilde{z_i}}$	0.5	-	-	-
$\rho_{\overline{w'\theta'_0},\overline{w'q'_0}}$	-0.92	-	-	-

Table 4.6: Correlation coefficient between surface fluxes and different quantities for case A186

Tab. 4.6 shows values of ρ, partially in different height levels, because high variances were found to occur near the surface and near the inversion layer atop the boundary layer, while the SC strength was maximum at 0.5 z_i (see Figs. 4.11 and 4.14). $\rho_{\overline{w'\theta'_0},\widetilde{z_i}}$ and $\rho_{\overline{w'\theta'_0},\overline{w'q'_0}}$ are independent from a height level. $\rho_{\overline{w'\theta'_0},\widetilde{z_i}}$ shows a medium correlation as it was expected from the findings of section 4.2.4. More interesting is $\rho_{\overline{w'q'_0},\widetilde{q'}}$ which displays very small correlations. It proves, that the latent heat flux distribution is in fact not significantly responsible for the humidity structures within the boundary layer. Unexpected is the negative correlation coefficient of -0.52 at the top of the boundary layer. It can be explained in consideration of $\rho_{\overline{w'\theta'_0},\overline{w'q'_0}}$ which shows a nearly perfect negative correlation (-0.92). This is no general finding, but it explains that the updrafts in this simulation case are occuring above areas with a high sensible heat flux but a very low latent heat flux. As was pointed out, the folding of the inversion interface yields

to a high spatial variance of $\widetilde{q'}$ and, more precisely, to a relatively high value of $\widetilde{q'}$ by comparison with the dry ambient air of the inversion layer itself. Hence, a correlation between $\overline{w'\theta'_0}$ and $\widetilde{q'}$ at the top of the boundary persists (not shown), which is by accident leading to the high value of $\rho_{\overline{w'q'_0},\widetilde{q'}}$. $\rho_{\overline{w'\theta'_0},\widetilde{\theta'}}$ exhibits the same characteristics (lower temperature than the ambient air at the top of the boundary layer), but an increasing correlation downwards. These results are in very good agreement with the analysis of the mesoscale structures in section 4.2.4.

4.3.2 Correlation study for the "Golden Days"

For the application of the streamwise-averaged correlation method, the case B1306 was chosen according to the demand of developed roll convection, which additionally needs to be more or less constant in time to allow representative results. The analysis method had to be modified by the restrictions given by the simulation setup. The total averaging area was not extended because of the diurnal cycle of the surface forcing, which allowed an averaging over a maximum time period of 1 h. An air parcel covers a distance of 21.6 km in this period, but the surface forcing is changing significantly. Therefore the decision was taken to use the pure model domain for averaging. The results show that this is a valid cutback. The fields were averaged as in the idealized study over 1 h, from $12-13$ UTC. The SC was strongest at $0.5\ z_i$, thus this height level was investigated instead of $0.4\ z_i$.

The obtained correlation coefficients of B1306 are generally in very good accordance to case A186, though the magnitude of the values is smaller (Tab. 4.7, cf. Tab. 4.6). Correlations of the sensible surface heat flux and $\widetilde{w}$, $\widetilde{z_i}$ and $\widetilde{\theta}$ are clearly detectable under realistic conditions. Due to the shortcomings by time-averaging in the background of a diurnal cycle, the results still show medium correlations equal or above $|0.47|$. $\rho_{\overline{w'q'_0},\widetilde{q'}}$ shows again, that there is most likely no correlation between the latent surface heat flux and the mesoscale humidity structures. In contrast to A186, it yields a small positive value at the top of the boundary layer, showing that the larger negative value in the idealized study was caused by the provided correlation of the two surface heat fluxes. For case B1306, this correlation is significantly smaller (0.31). It indicates, how sensible some calculated correlations might be to the simulation setup and the synoptic conditions.

Correlation	Height			
		$0.1 \cdot z_i$	$0.5 \cdot z_i$	$1.0 \cdot z_i$
$\rho_{\overline{w'q'_0},\widetilde{q'}}$	-	-0.2	-0.2	0.2
$\rho_{\overline{w'\theta'_0},\widetilde{\theta'}}$	-	0.62	0.51	-0.47
$\rho_{\overline{w'\theta'_0},\widetilde{w}}$	-	-	0.48	-
$\rho_{\overline{w'\theta'_0},\widetilde{z_i}}$	0.47	-	-	-
$\rho_{\overline{w'\theta'_0},\overline{w'q'_0}}$	0.31	-	-	-

Table 4.7: Correlation coefficient between surface fluxes and different quantities for case B1306

Conclusion

There is evidence to suggest that the main hypothesis of a linear correlation between the circulation structure (expressed by $\widetilde{w'}$) and the underlying averaged sensible surface heat flux is valid, but strongly dependent on the simulation setup or, more precisely, on the distribution

of heterogeneities and discontinuities due to different border area sizes as well as wind speed. However, large correlations up to 0.7 were achieved in the present study. The fetch study pointed out that the averaging distance can be optimized in dependence on the wind speed and above all, that the relevant upstream fetch is increasing with wind speed and could be taken into account for an estimation of a sufficient border area as well. Furthermore, it indicates the continuous transition from local to roll structures with increasing background wind.

With a comparison of the cases B1306 and A186, the applicability of the correlation analysis to more realistic simulation setups was proved for cases where the flow shows distinct roll convection (high background wind), which is necessary for the spanwise average. The fact that a diurnal cycle decreases the correlation was also shown. Nevertheless, the reduction of the correlation was found to be small. Furthermore, the independence of mesoscale humidity structures from the latent surface heat flux was pointed out. Previous statements on the role of evapotranspiration are confirmed.

5 Summary and Conclusions

The main objective of the present study was the numerical simulation of the turbulent flow over realistic heterogeneous terrain as a follow-up study to Uhlenbrock (2006). With the aid of the LES model PALM it was possible to simulate the flow over a $20\ \mathrm{km} \times 20\ \mathrm{km}$ area in the southeast of Berlin (Germany) for four different days in the diurnal cycle. The simulations were driven by measurement data from the LITFASS-2003 experiment. Particular attention was paid on the development and structure of thermal induced mesoscale circulations, also called secondary circulations (SC), that appeared over thermal discontinuities in the presence of background wind velocities between $2\ \mathrm{m/s}$ and $6\ \mathrm{m/s}$. The former results of Uhlenbrock (2006) were partly reviewed and among other things enhanced by a correlation study. The SCs were extracted from the simulation data by application of the ensemble-averaging method.

A sensitivity study on the effect of border areas with idealized time-independent forcing was necessary because cyclic horizontal boundaries were used in the model. It showed that even for a light background wind of $2\ \mathrm{m/s}$ an additional border of $10\ \mathrm{km}$ attached to each side of the model domain is required. For a background wind of $6\ \mathrm{m/s}$ a yet larger border area of $18\ \mathrm{km}$ was essential owing to the effect of advection.

The structure of SCs for the four simulations was found to be similar to the results of Uhlenbrock (2006) and superimposed on the flow field of small-scale turbulence. Observed differences are ascribed to the improved (larger) border areas used in the present study and the revised model code. The weak wind case showed strong SCs that span the entire boundary layer vertically (with maximum strength at $0.5\ z_i$) and that can be linked to the surface characteristics in the model domain. Over most patches that exhibited high surface heat fluxes (e.g. forest area), updrafts were obtained, while over areas with small heat fluxes (e.g. water patches), corresponding downdrafts could be observed. In transition to higher background winds, the structures are more and more affected by advection and distinct roll-like structures appeared in the case with a wind speed of $6\ \mathrm{m/s}$. The strength of the SC is significantly weakened by the background wind, but was not found to vanish. In the course of the day, the length scale of the circulations broadened since it grows proportionally to the boundary layer height, as was stated by Shen and Leclerc (1995) and Raasch and Harbusch (2001).

A Spectral analysis of the heterogeneity induced (mesoscale) atmospheric quantities pointed out, that the characteristic length scales of potential temperature and humidity are considerably larger than those of the velocity components, as proposed by Jonker et al. (1999) for a homogeneous CBL. The local ensemble-averaged boundary layer height was calculated by a modified gradient method of Uhlenbrock (2006) at each horizontal grid point and it was found that the boundary layer height is correlated to the SC and thus to the surface heat flux: SC updrafts are able to penetrate deeper into the inversion layer, causing enhanced local entrainment. Overall, the heterogeneity induced standard deviation of the boundary layer height was typically about $5\ \%$. In comparison to homogeneous control runs (HCR), the analysis revealed slightly decreased values of average boundary layer height. In the scientific community, there still is no consensus whether or not the existence of SCs has an effect on entrainment and thus the boundary layer height. The present study, however, supposes the entrainment by SCs to be less effective than by small-scale turbulence. In general an orientation of the mesoscale

structures to the mean wind was observed, particularly for high background winds.

The mesoscale contribution to vertical turbulent fluxes revealed no enhancement of the sensible heat flux but a significant contribution by the SCs. Thus ist can be assumed, that the vertical transport is partly taken over by SCs. The Reynolds stress on the contrary exhibited increased values, the vertical transport of momentum can be regarded as slightly enhanced in the presence of mesoscale circulations. The contribution to the vertical latent heat flux was found to increase with SC strength, since humidity structures are transported vertically by the SC to a great extent. In one case (highest background wind), the small-scale contribution yielded higher values than the respective total flux of the HCR, which implies that there must be some production of small-scale turbulence by heterogeneities.

A main part of the present study was a correlation study to prove the hypothesis that the flow over heterogeneous terrain is affected by a "smeared" surface heat flux in case of high background winds ($\geq 4\ \mathrm{m/s}$) and roll-like structures develop according to this heat flux. High linear correlation coefficients up to 0.7 were obtained between the streamwise-averaged fields of heterogeneity induced vertical velocity and surface heat flux for idealized cases with a time-independent forcing. For the LITFASS simulation case B1306 with time-dependent forcing, a correlation coefficient up to 0.48 was obtained at noon, which can still be assessed as good, in consideration of the restrictions by the more realistic setup. Therefore there is evidence, that the hypothesis of a linear correlation between streamwise-averaged surface heat flux and vertical velocity is valid. Furthermore it was possible to define a length, that yields information about the upstream fetch length in dependence of the background wind. Based on this fetch, it was possible to calculate a two-dimensional "effective surface heat flux" field, which is the surface heat flux, streamwise-averaged over the upstream fetch. It represents the surface heat flux that is seen by the flow and thus can be used to estimate the SC pattern.

Further research For further research, it is suggested to investigate entrainment processes in presence of SCs, since causes for the decrease or increase in this and other studies still remain unclear. A higher grid resolution is necessary to perform a real LES in the entrainment zone, since the typical size of the eddies here is small. To enhance the analyses and methods of the present study, it is furthermore proposed to extent the model domain for the analysis of the mesoscale scalar quantities $\widetilde{\theta}'$ and $\widetilde{q}'$ because the spectral analysis showed, that they scale approximately with the model domain. The behavior in larger model domains could enlighten the underlying processes. The correlation study could be optimized by taking into account the calculated fetch length in the streamwise-averaging procedure to obtain higher correlations and based on the effective surface heat flux, an estimation of the location and strength of SC might be developable.

During the calculation of the local boundary layer height after the method of Uhlenbrock (2006), near-surface inversions were observed in the ensemble-averaged temperature fields. They were found to occur directly above the strong discontinuity borders. These inversions might be linked to SC downdrafts. Following this idea, ring-shaped circulations for example around Lake Scharmützel might exist as weak sea breeze systems (cf. Fig. 1.2). Since the grid resolution was too low ($100\ \mathrm{m}$ in the horizontal and $50\ \mathrm{m}$ in the vertical direction), to investigate such circulations, the present study concentrated on SCs of the mesoscale. Nevertheless, this finding might be an indication of near-surface circulations on smaller scale at the heterogeneity borderlines. This would support the hypothesis of Mauder et al. (2008) and Foken et al. (2009) as well as the findings of the LES study of Inagaki et al. (2006), who proposed, that the non-closure of the energy balance in micrometeorological measurements (up to $25\ \%$ in LITFASS-2003) is originated from such SCs.

Bibliography

Albertson, J. D., Kustas, W. P., Scanlon, T. M. (**2001**): Large eddy simulation over heterogeneous terrain with remotely sensed land surface conditions. Water Resourc. Res.. 37(7), p. 1939–1953.

Albertson, J. D., Parlange, M. B. (**1999a**): Natural Integration of scalar fluxes from complex terrain. Adv. Water Res.. 23, p. 239–252.

Albertson, J. D., Parlange, M. B. (**1999b**): Surface Length Scales and Shear Stress: Implications for Land-Atmosphere Interaction over Complex Terrain. Water Resour. Res.. 35, p. 2121–2132.

Arakawa, A., Lamb, V. R. (**1977**): Computational design of the basic dynamical processes of the UCLA general circulation model. In: J. Chang (Ed.), 1977: General circulation models of the atmopshere. Methods in Computational Physics, Berlin, 17, p. 173-265.

Asselin, R. (**1972**): Frequency filter for the time integrations. Mon. Wea. Rev.. 100, p. 487–490.

Avissar, R., Schmidt, T. (**1998**): An Evaluation of the Scale at which Ground-Surface Heat Flux Patchiness Affects the Convective Boundary Layer Using Large-Eddy Simulations. J. Atmos. Sci.. 55, p. 2666–2689.

Bange, J., Spieß, T., et. al. (**2006**): Turbulent fluxes from Helipod flights above quasi-homogeneous patches within the LITFASS area. Boundary-Layer Meteorol.. 121, p. 127–151.

Bertoldi, G., Kustas, W. P., Albertson, J. D. (**2008**): Estimating Spatial Variability in Atmospheric Properties over Remotely Sensed Land Surface Conditions. J. Appl. Meteorol.. 47, p. 2147–2165.

Betts, A. K. (**1974**): Non-precipitating cumulus convection and its parameterization. Quart. J. R. Met. Soc.. 99, p. 178–196.

Beyrich, F., Adams, E. K., et. al. (**2004**): Verdunstung über einer heterogenen Landoberfläche - Das LITFASS-2003 Experiment - Ein Bericht. Report 79. Deutscher Wetterdienst. Offenbach, Germany. ISSN 1430-0281.

Beyrich, F., Herzog, H.-J., Neisser, J. (**2002a**): The LITFASS project of the DWD and the LITFASS-98 experiment: The project strategy and the experimental setup. Theor. Appl. Climatol.. 73, p. 3–18.

Beyrich, F., Leps, J.-P., et. al. (**2006a**): Area-averaged surface fluxes over the LITFASS region based on eddy-covariance measurements. Boundary-Layer Meteorol.. 121, p. 33–65.

Beyrich, F., Mengelkamp, H.-T. (**2006**): Evaporation over a Heterogeneous Land Surface: EVA_GRIPS and the LITFASS-2003 Experiment: An Overview. Boundary-Layer Meteorol.. 121, p. 5–32.

Beyrich, F., Richter, S. H., et al. (**2002b**): Experimental determination of turbulent fluxes over heterogeneous LITFASS area: selected results from the LITFASS-98 experiment. Theor. Appl. Climatol.. 73, p. 19–34.

Blackadar, A. K. (**1997**): Turbulence and Diffusion in the Atmosphere. Springer, Berlin, Heidelberg, New York.

Bou-Zeid, E., Meneveau, M., Parlange, M. P. (**2004**): Large-eddy simulation of neutral atmospheric boundary layer flow over heterogeneous surfaces: Blending height and effective surface roughness. Water Resour. Res.. 40, p. 1–18.

Boussinesq, J. V. (**1903**): Théorie analytique de la chaleur. Vol. 2. p. 154–176. Gauthier-Villars, Paris.

Chen, F., Avissar, R. (**1994a**): The Impact of Land-Surface Wetness Heterogeneity on Mesoscale Heat Fluxes. J. Appl. Meteorol.. 33, p. 1323–1340.

Chen, F., Avissar, R. (**1994b**): Impact of land-surface moisture variability on local shallow convective cumulus and precipitation in large-scale models. J. Appl. Meteor.. 33, p. 1382–1401.

Chlond, A. (**1994**): Locally modified version of Bott's advection scheme. Mon. Wea. Rev.. 122, p. 111–125.

Chorin, A. J. (**1968**): Numerical solution of the Navier-Stokes equations. Math. Comp.. 22, p. 745–762.

Chorin, A. J. (**1969**): On the convergence of discrete approximations to the Navier-Stokes equations. Math. Comp.. 23, p. 341–353.

Courant, R., Friedrichs, K., Lewy, H. (**1928**): Über die partiellen Differentialgleichungen der mathematischen Physik. Math. Ann.. 100, p. 32–74.

Courault, D., Drobinski, P., Brunet, Y., Lacarrere, P., Talbot, C. (**2007**): Impact of surface heterogeneity on a buoyancy-driven convective boundary layer in light winds. Boundary-Layer Meteorol.. 124, p. 383–403.

Couvreaux, F., Guichard, F., Redelsperger, J.-L., Kiemle, C., Masson, V., Lafore, J.-P., Flamant, C. (**2005**): Water-vapor variability within a convective boundary-layer assessed by large-eddy simulations and IHOP_2002 observations. Quart. J. R. Met. Soc.. 131, p. 2665–2693.

De Roode, S. R., Duynkerke, P. G., Jonker, H. J. J. (**2004**): Large-Eddy Simulation: How Large is Large Enough?. J. Atmos. Sci.. 61, p. 403–421.

Deardorff, J. W. (**1972**): Numerical investigation of neutral and unstable planetary boundary layers. J. Atmos. Sci.. 29, p. 91–115.

Deardorff, J. W. (**1974**): Three-dimensional numerical study of the height and mean structure of a heated planetary boundary layer. Boundary-Layer Meteorol.. 7, p. 81–106.

Deardorff, J. W. (**1980**): Stratocumulus-capped mixed layers derived from a three-dimensional model. Boundary-Layer Meteorol.. 18, p. 495–527.

Deardorff, J. W., Stockton, B. H. (**1980**): Laboratory Studies of the entrainment zone of a convectively mixed layer. J. Fluid. Mech.. 100, p. 41–64.

Doran, J. C., Zhong, S. (**2000**): A study of the effects of subgrid-scale land use differences on atmospheric stability in prestorm environments. J. Geophys. Res.. 105, p. 9381–9392.

Durran, D. R. (**1999**): Numerical methods for wave equations in geophysical fluid dynamics. Springer, New York.

Etling, D. (**2002**): Theoretische Meteorologie. Eine Einführung. Springer, Berlin, Heidelberg, New York.

Etling, D., Brown, R. A. (**1993**): Roll vortices in the planetary boundary layer: A review. Boundary-Layer Meteorol.. 65, p. 215–248.

Fedorovich, E., Conzemius, R., Mironov, D. (**2004**): Convective Entrainment into a Shear-Free, Linearly Stratisfied Atmosphere: Bulk Models Reevaluated through Large Eddy Simulations. J. Atmos. Sci.. 61, p. 281–295.

Ferziger, J. H., Perić, M. (**2002**): Computational Methods for Fluid Dynamics. 3rd Ed.. Springer.

Fesquet, C., Dupont, S., et. al. (**2009**): Impact of Terrain Heterogeneity on Coherent Structure Properties: Numerical Approach. Boundary-Layer Meteorol.. 133, p. 71–92.

Foken, T. (**2003**): Angewandte Meteorologie. 1st Ed.. Springer.

Foken, T., Mauder, M., et. al. (**2009**): Energy balance closure for the LITFASS-2003 experiment. Theor. Appl. Climatol.. doi: 10.1007/s00704-009-0216-8.

Foken, T., Wichura, B. (**1996**): Tools for quality assessment of surface-based flux measurements. Agric. For. Meteorol.. 78, p. 83–105.

Franke, T. (**2008**): Numerische Simulation von Staubteufeln in der atmosphärischen Grenzschicht. Diploma thesis. Leibniz University of Hannover. Hannover.

Fröhlich, J. (**2006**): Large Eddy Simulationen turbulenter Strömungen. Teubner, Wiesbaden.

Garratt, J. R. (**1992**): The atmospheric boundary layer. Cambridge University Press, Cambridge.

Gopalakrishnan, S. G., Avissar, R. (**2000**): An LES study of the impacts of land surface heterogeneity on dispersion in the convective boundary layer. J. Atmos. Sci.. 57, p. 352–371.

Gropp, W., Lusk, E., Skjellum, A. (**1999**): Using MPI. Portable parallel programming with the Message-Passing Interface. 2nd Ed.. MIT Press, Cambridge, Mass.

Gryschka, M., Drüe, C., Etling, D., Raasch, S. (**2008**): On the influence of sea-ice inhomogeneities onto roll convection in cold-air outbreaks. Geophys. Res. Lett.. 35. l23804, doi:10.1029/2008GL035845.

Hadfield, M. G., Cotton, W. R., Pielke, R. A. (**1991**): Large-eddy simulations of thermally forced circulations in the convective boundary layer. Part I: a small-scale circulation with zero wind. Boundary-Layer Meteorol.. 57, p. 79–114.

Hadfield, M. G., Cotton, W. R., Pielke, R. A. (**1992**): Large-eddy simulations of thermally forced circulations in the convective boundary layer. Part II: the effect of change in wavelength and wind speed. Boundary-Layer Meteorol.. 58, p. 307–327.

Hechtel, L. M., Moeng, C.-H., Stull, R. B. (**1990**): The effects of Nonhomogeneous Surface Fluxes on the Convective Boundary Layer: A Case Study using Large-Eddy Simulation. J. Atmos. Sci.. 47, p. 1721–1741.

Heinemann, G., Kerschgens, M. (**2006**): Simulation of surface energy fluxes using high-resolution non-hydrostatic simulations and comparisons with measurements for the LITFASS-2003 experiment. Boundary-Layer Meteorol.. 121, p. 195–220.

Holton, J. R. (**2004**): An Introduction to Dynamic Meteorology. International Geophysics Series. 4th Ed.. Elsevier Academic Press.

Huang, H.-Y., Stevens, B., Margulis, S. A. (**2008**): Application of Dynamic Subgrid-scale Models for Large-eddy Simulation of the Daytime Convective Boundary Layer over Heterogeneous Surfaces. Boundary-Layer Meteorol.. 126, p. 327–348.

Huang, J., Lee, X., Patton, E. G. (**2009**): Dissimilarity of Scalar Transport in the Convective Boundary Layer in Inhomogeneous Landscapes. Boundary-Layer Meteorol.. 130, p. 327–345.

Inagaki, A., Letzel, M. O., Raasch, S., Kanda, M. (**2006**): Impact of Surface Heterogeneity on Energy Imbalance: A Study Using LES. J. Meteor. Soc. Japan. 84(1), p. 187–198.

Jonker, H. J. J., Duynkerke, P. G., Cuijpers, J. W. M. (**1999**): Mesoscale Fluctuations in Scalars Generated by Boundary Layer Convection. J. Atmos. Sci.. 56, p. 801–808.

Kaimal, J. C., Wyngaard, J. C., Haugen, D. A., Coté, O. R., Izumi, Y. (**1976**): Turbulence Structure in the Convective Boundary Layer. J. Atmos. Sci.. 33, p. 2152–2169.

Kang, S.-L. (**2009**): Temporal Oscillations in the Convective Boundary Layer Forced by Mesoscale Surface Heat-Flux Variations. Boundary-Layer Meteorol.. 132, p. 59–81.

Kang, S.-L., Davis, K. J. (**2007**): Observations of the ABL Structures over a Heterogeneous Land Surface during IHOP_2002. J. Hydrometeor.. 8, p. 221–244.

Kang, S.-L., Davis, K. J. (**2008**): The Effects of Mesoscale Surface Heterogeneity on the Fair-Weather Convective Atmospheric Boundary Layer. J. Atmos. Sci.. 65, p. 3197–3213.

Katsouvas, G. D., Helmis, C. G., Wang, Q. (**2007**): Quadrant analysis of the scalar and momentum fluxes in the stable marine atmospheric surface layer. Boundary-Layer Meteorol.. 124, p. 335–360.

Kimmel, S. J., Wyngaard, J. C., Otte, M. J. (**2002**): "Log-Chipper" Turbulence in the Convective Boundary Layer. J. Atmos. Sci.. 59, p. 1124–1134.

Kohsiek, W., Meijninger, W. M. L., Beyrich, F., De Bruin, H. A. R. (**2006**): Saturation of the large aperture Scintillometer. Boundary-Layer Meteorol.. 121, p. 111–126.

Kolmogorov, A. N. (**1941**): Die lokale Struktur der Turbulenz in einer inkompressiblen zähen Flüssigkeit bei sehr hohen Reynoldsschen Zahlen. Dokl. Akad. Nauk. SSSR. 32, p. 299–303. Reprinted in: H. Goering (Ed.), 1958: Statistische Theorie der Turbulenz. Akademie-Verlag, Berlin, p. 77–81.

Kustas, W. P., Albertson, J. D. (**2003**): Effects of surface temperature contrast on land-atmosphere exchange: A case study from Monsoon 90. Water Resourc. Res.. 39(6), p. 1159–1174.

Kustas, W. P., Goodrich, D. C. (**1994**): Preface to special section on Monsoon'90. Water Resour. Res.. 30, p. 1211–1225.

Lenschow, D. H., Sun, J. (**2007**): The spectral composition of fluxes and variances over land and sea out to the mesoscale. Boundary-Layer Meteorol.. 125, p. 63–84.

Letzel, M. O. (**2007**): High resolution Large-Eddy Simulation of the flow around buildings. PhD Thesis, Leibniz University of Hannover. Hannover.

Letzel, M. O., Raasch, S. (**2003**): Large Eddy Simulation of Thermally Induced Oscillations in the Convective Boundary Layer. J. Atmos. Sci.. 60, p. 2328–2341.

Lilly, D. K. (**2002**): Entrainment into Mixed Layers. Part I: Sharp-Edged and Smoothed Tops. J. Appl. Meteorol.. 59, p. 3340–3352.

Lynn, B. H., Rind, D., Avissar, R. (**1995**): The Importance of Mesoscale Circulations Generated by Subgrid-Scale Landscape Heterogeneities in General Circulation Models. J. Climate. 8, p. 191–205.

Mahrer, Y., Pielke, R. A. (**1978**): A test of an upstream spline interpolation technique for the advective terms in a numerical mesoscale model. Mon. Wea. Rev.. 106, p. 818–830.

Mahrt, L., Paumier, J. (**1984**): Heat Transport in the Atmospheric Boundary Layer. J. Atmos. Sci.. 41, p. 3061–3075.

Mauder, M., Desjardins, R. L., Pattey, E., Gao, Z., van Haarlem, R. (**2008**): Measurement of the Sensible Eddy Heat Flux Based on Spatial Averaging of Continuous Ground-Based Observations. Boundary-Layer Meteorol.. 128, p. 151–172.

Mauder, M., Liebethal, C., et. al. (**2006**): Processing and quality control of flux data during LITFASS-2003. Boundary-Layer Meteorol.. 121, p. 67–88.

Meijninger, W. M. L., Beyrich, F., Lüdi, A., Kohsiek, W., De Bruin, H. A. R. (**2006**): Scintillometer-based turbulent fluxes of sensible and latent heat over a heterogeneous land surface - A contribution to LITFASS-2003. Boundary-Layer Meteorol.. 121, p. 89–110.

Neisser, J., Adam, W., Beyrich, F., Leiterer, U., Steinhagen, H. (**2002**): Atmospheric boundary layer monitoring at the Meteorological Observatory Lindenberg as part of the Lindenberg Column: facilities and selected results. Meteorol. Z.. 11, p. 241–253.

Oncley, S. P., Friehe, C. A., Larue, J. C., Businger, J. A., Itsweire, E. C., Chang, S. S. (**1996**): Surface-Layer Fluxes, Profiles and Turbulence Measurements over Uniform Terrain under Near-Neutral Conditions. J. Atmos. Sci.. 53, p. 1029–1044.

Patrinos, A. N. A., Kistler, A. L. (**1977**): A Numerical Study of the Chicago Lake Breeze. Boundary-Layer Meteorol.. 12, p. 93–123.

Patton, E. G., Sullivan, P. P., Moeng, C.-H. (**2005**): The Influence of Idealized Heterogeneity on Wet and Dry Planetary Boundary Layers Coupled to the Land Surface. J. Atmos. Sci.. 62, p. 2078–2097.

Piacsek, S. A., Williams, G. P. (**1970**): Conservation properties of convection difference schemes. J. Comput. Phys.. 6, p. 392–405.

Pielke, R. A. (**2001**): Influence of the spatial distribution of vegetation and soils on the prediction of cumulus convective rainfall. Rev. Geophys.. 39(2), p. 151–177.

Pino, D., Jonker, H. J. J., Vilà-Guerau de Arellano, J., Dosio, A. (**2006b**): Role of shear and the inversion strength during sunset turbulence over land: characteristic length scales. Boundary-Layer Meteorol.. 121, p. 537–556.

Pino, D., Vilà-Guerau de Arellano, J., Kim, S.-W. (**2006a**): Representing Sheared Convective Boundary Layer by Zeroth- and First-Order-Jump Mixed-Layer Models: Large-Eddy Simulation Verification. J. Appl. Meteorol.. 45, p. 1224–1243.

Prabha, T. V., Karipot, A., Binford, M. W. (**2007**): Characteristics of secondary circulations over an inhomogeneous surface simulated with large-eddy simulation. Boundary-Layer Meteorol.. 123, p. 239–261.

Raasch, S., Etling, D. (**1991**): Numerical simulation of rotating turbulent thermal convection. Beitr. Phys. Atmos.. 64, p. 185–199.

Raasch, S., Etling, D. (**1998**): Modeling deep ocean convection: Large eddy simulation in comparison with laboratory experiments. J. Phys. Oceano.. 28, p. 1786–1802.

Raasch, S., Harbusch, G. (**2001**): An Analysis of Secondary Circulations and their Effects caused by small-scale Surface Inhomogeneities using Large-Eddy Simulation. Boundary-Layer Meteorol.. 101, p. 31–59.

Raasch, S., Schröter, M. (**2001**): PALM - A large-eddy simulation model performing on massively parallel computers. Meteorol. Z.. 10, p. 363–372.

Ramos da Silva, R. (**2006**): The Hydrometeorology of a Deforested Region of the Amazon Basin. J. Hydrometeor.. 7, p. 1028–1044.

Reen, B. P., Stauffer, D. R., Davis, K. J., Desai, A. R. (**2006**): A case study on the effects of heterogeneous soil moisture on mesoscale boundary-layer structure in the southern Great Plains, U.S.A. part II: Mesoscale modelling. Boundary-Layer Meteorol.. 120, p. 275–314.

Reynolds, O. (**1895**): On the dynamical theory of incompressible viscous fluids and the determination of the criterion. Phil. Trans. Roy. Soc.. A186, p. 123–164.

Roache, P. J. (**1985**): Computational Fluid Dynamics. Hermosa Publishers, Albuquerque, New Mexiko.

Roy, B. S., Avissar, R. (**2000**): Scales of response of the convective boundary layer to land-surface heterogeneity. Geophys. Res. Lett.. 27, p. 533–536.

Satoh, M. (**2004**): Atmospheric Circulation Dynamics and General Circulation Models. Springer, Berlin, Heidelberg, New York.

Schröter, M. (**2003**): Untersuchung der Evolution von Konvektionsstrukturen bei Kaltluftausbrüchen mit Hilfe eines parallelisierten Grobstrukturmodells. PhD Thesis, Leibniz University of Hannover. Hannover.

Schumann, U. (**1973**): Ein Verfahren zur direkten numerischen Simulation von Strömungen in Platten- und Ringspaltkanälen und über seine Anwendung zur Untersuchung von Turbulenzmodellen. PhD Thesis, Universität Karlsruhe. Karlsruhe.

Schumann, U. (**1975**): Subgrid Scale Model for Finite Difference Simulations of Turbulent Flows in Plane Channels and Annuli. J. Comput. Phys.. 18, p. 376–404.

Sellers, P., Hall, F. G., et. al. (**1995**): The Boreal Ecosystem-Atmosphere Study (BOREAS) - An Overview and Early Results from the 1994 Field Year. Bull. Am. Meteorol. Soc.. 76, p. 1549–1577.

Shaw, R. H., Tavangar, J., Ward, D. P. (**1983**): Structure of the Reynolds Stress in a Canopy Layer. J. Clim. Appl. Meteorol.. 22, p. 1922–1931.

Shen, S., Leclerc, M. Y. (**1995**): How large must surface inhomogeneities be before they influence the convective boundary layer structure? A case study. Q.J.R. Meteorol. Soc.. 121, p. 1209–1228.

Shepard, D. (**1968**): A two-dimensional interpolation function for irregularly-spaced data. Proceedings of the 1968 23rd ACM national conference. p. 517–524. ACM, New York, NY, USA.

Shuttleworth, W., Yang, Z.-L., Arain, M. A. (**1997**): Aggregation rules for surface parameters in global models. Hydrol. Earth Syst. Sci.. 1, p. 217–226.

Steinfeld, G. (**2009**): Die Analyse von Turbulenzmess- und Analyseverfahren der Mikrometeorologie durch virtuelle Messungen innerhalb von Großstruktursimulationen. PhD Thesis, Leibniz University of Hannover. Hannover.

Stoll, R., Porté-Agel, F. (**2009**): Surface Heterogeneity Effects on Regional-Scale Fluxes in Stable Boundary Layers: Surface Temperature Transitions. J. Atmos. Sci.. 66, p. 412–431.

Stull, R. B. (**1988**): An Introduction to Boundary Layer Meteorology. Kluwer Academic Publishers, Dordrecht.

Sullivan, P. P., Moeng, C.-H., Stevens, B., Lenschow, D. H., Mayor, S. D. (**1998**): Structure of the Entrainment Zone Capping the Convective Atmospheric Boundary Layer. J. Atmos. Sci.. 55, p. 3042–3064.

Sun, J., Xu, Q. (**2009**): Parameterization of Sheared Convective Entrainment in the First-Order Jump Model: Evaluation Through Large-Eddy Simulation. Boundary-Layer Meteorol.. 132, p. 279–288.

Tennekes, H., Lumley, J. L. (**1973**): A first course in turbulence. The MIT Press, Cambridge.

Uhlenbrock, J. (**2006**): Numerische Untersuchung der konvektiven Grenzschicht über realen heterogenen Landoberflächen mit einem Grobstruktursimulationsmodell. PhD Thesis, Leibniz University of Hannover. Hannover.

van Dop, H., van As, D., van Herwijnen, A., Hibbert, M. F., Jonker, H. J. J. (**2005**): Length Scales of Scalar Diffusion in the Convective Boundary Layer: Laboratory Observations. Boundary-Layer Meteorol.. 116, p. 1–35.

van Heerwaarden, C. C., Vilà-Guerau de Arellano, J. (**2008**): Relative Humidity as an Indicator for Cloud Formation over Heterogeneous Land Surfaces. J. Atmos. Sci.. 65, p. 3263–3277.

Weaver, C. P. (**2004**): Coupling between large-scale atmospheric processes and mesoscale land–atmosphere interactions in the U.S. southern Great Plains during summer. Part II: Mean impacts of the mesoscale. J. Hydrometeor.. 5, p. 1247–1258.

Weaver, C. P., Avissar, R. (**2001**): Atmospheric Disturbances Caused by Human Modification of the Landscape. Bull. Am. Meteorol. Soc.. 82, p. 269–281.

Weckwerth, T. M., Parsons, D. B., et. al. (**2004**): An Overview of the International H2O Project (IHOP_2002) and Some Preliminary Highlights. Bull. Am. Meteorol. Soc.. 85, p. 253–277.

Wyngaard, J. C., Coté, O. R. (**1974a**): The evolution of a convective planetary boundary layer - a higher-order-closure model study. Boundary-Layer Meteorol.. 7, p. 289–308.

Wyngaard, J. C., Coté, O. R., Kao, K. S. (**1974b**): Modeling the atmospheric boundary layer. Adv. Geophys.. 18A, p. 193–212.

Zhong, S., Doran, J. C. (**1997**): A study of the effects of spatially varying fluxes on cloud formation and boundary layer properties using data from the southern Great Plains cloud and radiation testbed. J. Climate. 10, p. 327–341.

Zhong, S., Doran, J. C. (**1998**): An evaluation of the importance of surface flux variability on GCM-scale boundary layer characteristics using realistic meteorological and surface forcing. J. Climate. 11, p. 2774–2788.

Eidesstattliche Erklärung

Hiermit erkläre ich, dass ich die vorliegende Diplomarbeit selbstständig und nur unter Verwendung der angegebenen Quellen und Hilfsmittel angefertigt habe.

Hannover, 26. Mai 2010